Helsinki University of Technology Laboratory of Computational Engineering Publications
Teknillisen korkeakoulun Laskennallisen tekniikan laboratorion julkaisuja
Espoo 2004 REPORT B40

COMPUTATIONAL STUDIES OF PATTERN FORMATION IN TURING SYSTEMS

Teemu Leppänen

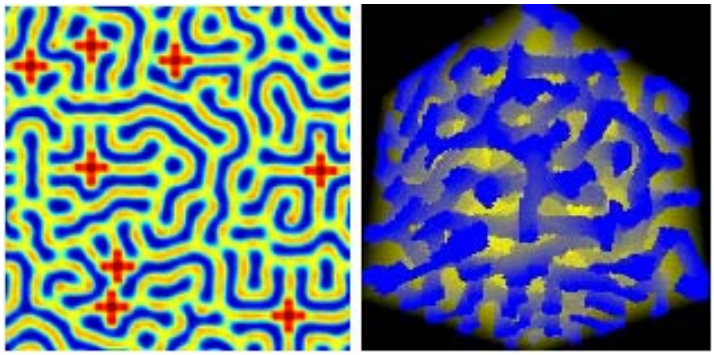

TEKNILLINEN KORKEAKOULU
TEKNISKA HÖGSKOLAN
HELSINKI UNIVERSITY OF TECHNOLOGY
TECHNISCHE UNIVERSITÄT HELSINKI
UNIVERSITE DE TECHNOLOGIE D'HELSINKI

Helsinki University of Technology Laboratory of Computational Engineering Publications
Teknillisen korkeakoulun Laskennallisen tekniikan laboratorion julkaisuja
Espoo 2004 REPORT B40

COMPUTATIONAL STUDIES OF PATTERN FORMATION IN TURING SYSTEMS

Teemu Leppänen

Dissertation for the degree of Doctor of Science in Technology to be presented with due permission of the Department of Electrical and Communications Engineering, Helsinki University of Technology, for public examination and debate in Auditorium S4 at Helsinki University of Technology (Espoo, Finland) on the 27th of November, 2004, at 12 noon.

Helsinki University of Technology
Department of Electrical and Communications Engineering
Laboratory of Computational Engineering

Teknillinen korkeakoulu
Sähkö- ja tietoliikennetekniikan osasto
Laskennallisen tekniikan laboratorio

Distribution:
Helsinki University of Technology
Laboratory of Computational Engineering
P. O. Box 9203
FIN-02015 HUT
FINLAND
Tel. +358-9-451 4826
Fax. +358-9-451 4830
http://www.lce.hut.fi

Online in PDF format: http://lib.hut.fi/Diss/2004/isbn9512273969

E-mail: Teemu.Leppanen@hut.fi

ISBN 951-22-7395-0 (printed)
ISBN 951-22-7396-9 (PDF)
ISSN 1455-0474
PicaSet Oy
Espoo 2004

Abstract

This thesis is an analytical and computational treatment of Turing models, which are coupled partial differential equations describing the reaction and diffusion behavior of chemicals. Under particular conditions, such systems are capable of generating stationary chemical patterns of finite characteristic wave lengths even if the system starts from an arbitrary initial configuration. The characteristics of the resulting dissipative patterns are determined intrinsically by the reaction and diffusion rates of the chemicals, not by external constraints. Turing patterns have been shown to have counterparts in natural systems and thus Turing systems could provide a plausible way to model the mechanisms of biological growth. Turing patterns grow due to diffusion-driven instability as a result of infinitesimal perturbations around the stationary state of the model and exist only under non-equilibrium conditions. Turing systems have been studied using chemical experiments, mathematical tools and numerical simulations.

In this thesis a Turing model called the Barrio-Varea-Aragon-Maini (BVAM) model is studied by employing both analytical and numerical methods. In addition to the pattern formation in two-dimensional domains, also the formation of three-dimensional structures is studied extensively. The scaled form of the BVAM model is derived from first principles. The model is then studied using the standard linear stability analysis, which reveals the parameter sets corresponding to a Turing instability and the resulting unstable wave modes. Then nonlinear bifurcation analysis is carried out to find out the stability of morphologies induced by two-dimensional hexagonal symmetry and various three-dimensional symmetries (SC, BCC, FCC). This is realized by employing the center manifold reduction technique to obtain the amplitude equations describing the reduced chemical dynamics on the center manifold. The main numerical results presented in this thesis include the study of the Turing pattern selection in the presence of bistability, and the study of the structure selection in three-dimensional Turing systems depending on the initial configuration. Also, the work on the effect of numerous constraints, such as random noise, changes in the system parameters, thickening domain and multistability on Turing pattern formation brings new insight concerning the state selection problem of non-equilibrium physics.

Preface

The research presented in this dissertation has been carried out at the Laboratory of Computational Engineering (LCE), Helsinki University of Technology (HUT), mostly during the years 2002-2004, while working in the Biophysics and Statistical Mechanics, and the Complex Systems groups. The work was initiated during my apprenticeship at LCE as a second-year student in the summer of 2000. My postgraduate studies were funded by the Graduate School in Computational Methods of Information Technology (ComMIT) and the Academy of Finland under the Finnish Centre of Excellence Programme. I also gratefully acknowledge the financial support from the Finnish Academy of Science and Letters (Väisälä fund), and the Jenny and Antti Wihuri foundation.

First and foremost, I wish to express my gratitude to Prof. Kimmo Kaski for directing me to the amazingly interesting field of Turing systems, giving me the opportunity to combine the research flexibly with my interdisciplinary studies, and encouraging me all the way through. My sincere thanks go to Prof. Rafael Barrio for his support and inspiring guidance. I also wish to thank Dr. Mikko Karttunen, who has instructed me numerous times during this project. In addition, I am grateful to Dr. Murat Ünalan for sharing his biological expertise, and Prof. Philip Maini for his hospitality during my one-month visit to the Centre for Mathematical Biology at the University of Oxford.

Thanks are also due to LCE personnel for making the laboratory an enjoyable environment to work. I would especially like to thank my office mate Sebastian von Alfthan for advice and making the work days fruitful, and Jukka-Pekka Onnela for the intensive and motivating discussions. I would also like to thank my colleagues Ville Mäkinen, Markus Miettinen, Petri Nikunen, Toni Tamminen and Ilkka Kalliomäki for keeping up the cheerful and encouraging atmosphere.

I would not have been able to complete my studies at HUT as fast as I did without the unfailing support from my family. I am obliged to my parents Anita and Olli for teaching me the meaning of hard work through their own example. I also wish to thank my delightful sisters Helmi and Marjaana for tolerating me.

Lastly, thank you Satu for your unconditional love and optimism.

Teemu I. Leppänen

List of publications

Although this thesis has been written as a monograph, it is based on the results that have been published in the following scientific articles:

1. T. Leppänen, M. Karttunen, K. Kaski, R. A. Barrio, and L. Zhang, A new dimension to Turing patterns, *Physica D* **168-169C**, 35-44 (2002).

2. T. Leppänen, M. Karttunen, K. Kaski, and R. A. Barrio, The effect of noise on Turing patterns, *Prog. Theor. Phys. (Suppl.)* **150**, 367-370 (2003).

3. T. Leppänen, M. Karttunen, K. Kaski, and R. Barrio, Dimensionality effects in Turing pattern formation, *Int. J. Mod. Phys. B* **17**, 5541-5553 (2003).

4. T. Leppänen, M. Karttunen, K. Kaski, and R. A. Barrio, Turing systems as models of complex pattern formation, *Braz. J. Phys.* **34**, 368-372 (2004).

5. T. Leppänen, M. Karttunen, R. A. Barrio, and K. Kaski, Morphological transitions and bistability in Turing systems, *Phys. Rev. E* **70**, (2004).

6. T. Leppänen, The theory of Turing pattern formation, in *Current Topics in Physics* (Imperial College Press), a book chapter in press (2004).

7. T. Leppänen, M. Karttunen, R. A. Barrio, and K. Kaski, Spatio-temporal dynamics in a Turing model, *InterJournal*, submitted (2004).

The work has also been presented in the following popular science articles:

- T. Leppänen and K. Kaski, Matemaatikko selätti seepran raidat (in Finnish), *Tiede* **1**, 48-49 (2004).

- T. Leppänen and K. Kaski, Matemaatikko luonnonilmiöiden jäljillä (in Finnish), *Arkhimedes* **2**, 13-16 (2004).

Contents

Chapter 1

Introduction

Natural systems exhibit an amazing diversity of structures in both living and non-living systems. Trees and plants growing from a single seed can show extremely complex organization not to mention mammals, whose development begins from a single fertilized egg cell. Mathematical biologists devise and study models that at least qualitatively capture some essential characteristics of the natural mechanisms of growth. In these models the primary interest is not in genes, but in the processes that follow the activation of a gene. The information stored in DNA corresponds to a blueprint, which is put into action by spontaneous physico-chemical processes. DNA is known to have three billion (3×10^9) base pairs, whereas an adult human being consists of tens of trillions of cells (10^{13}). Thus it cannot contain enough information for determining everything in detail, but it is responsible for the major guidelines for the development of an organism. What could the spontaneous processes generating the structure by following these guidelines be?

More than half a century ago a British mathematician Alan M. Turing addressed the problem. He assumed that genes (or proteins and enzymes) act only as catalysts for spontaneous chemical reactions, which regulate the production of other catalysts or morphogens. Finally, cells differentiate according to the morphogen concentration in their surroundings. There was not any new physics involved in Turing's idea, but he merely suggested that the fundamental physical laws can account for complex physico-chemical behavior. In 1952 Turing published his seminal article titled *The Chemical Basis of Morphogenesis*, where he showed that a simple mathematical model describing spontaneously spreading and reacting chemicals could give rise to stationary spatial concentration patterns of fixed characteristic length from a random initial configuration and proposed that *reaction-diffusion models* might have relevance in describing *morphogenesis*, the growth of biological form.

Turing begun his reasoning by considering the problem of a spherically symmetrical fertilized egg cell becoming a complex and highly structured organism. A

spherically symmetrical egg should remain spherically symmetrical forever notwithstanding plain chemical diffusion and reactions. As Turing (1952) put it: *"From spherical initial state chemical reactions and diffusion certainly cannot result in an organism such as a horse, which is not spherically symmetrical."* However, Turing showed that there is a fallacy in this argument and reasoned that something must make the stable spherical state unstable and thus cause spontaneous symmetry-breaking. The egg in the blastula stage is never exactly spherically symmetrical and the random deviations from the spherical symmetry are different in two eggs of the same species. Thus one could argue that those deviations are not of importance since all the organisms of a certain species will end up having the same anatomical structure irrespective of the initial random deviations. However, Turing emphasized and showed that *"it is important that there are some deviations, for the system may reach a state of instability in which these irregularities tend to grow"* (Turing, 1952). In other words, if there are no random deviations, the egg will stay in the spherical state forever. In biological systems the random deviations arise spontaneously due to natural noise and distortions.

Turing proved rigorously that a chemical state, which is stable against perturbations in the absence of diffusion may become unstable to perturbations in the presence of diffusion. *Turing* or *diffusion-driven instability* is initiated by arbitrary random deviations of the stationary state and results in stationary spatially periodic variations in the chemical concentration, i.e., chemical patterns. The idea that diffusion could make a stable and uniform chemical state unstable was innovative since usually diffusion is thought to be stabilizing (e.g. a droplet of ink dispersing to water). Intuitively Turing instability can be understood by considering the long-range effects of the chemicals, which are not equal due to the difference in the pace of diffusion and thus an instability arises. The random initial conditions naturally have an effect on the resulting pattern, but only with respect to the phase of the pattern. The intrinsic parameters determine that the system will evolve e.g. towards stripes of a fixed width instead of spots, but the random initial conditions together with the effects of the boundaries and the domain geometry determine the exact positions and the alignment of the stripes (the phase). This idea becomes evident by considering the fact that all tigers have stripes, but the stripe pattern is not exactly similar in all individual tigers.

Some exhilarating common sense explanations of the mechanism of the Turing instability can be found from the literature: Murray has discussed sweating grasshoppers on a dry grass field that is set alight (Murray, 1989). I have often tried to illustrate the mechanism by using Turing's own metaphor of missionaries (M) and cannibals (C) on an island, which we will next revive. Imagine an island inhabited by efficiently reproducing cannibals. It happens so that some missionaries decide to come to the island by boat to evangelize the cannibals. What happens then? The rules are: If two or more missionaries meet one cannibal they can convert him into a missionary ($C + 2M \rightarrow 3M$). If the relative strength

is the other way around, the missionaries get killed and eaten by the cannibals ($2C + M \rightarrow 2C$). As the missionaries die, more missionaries are brought to the island. The competition between forces, constraints or tendencies is characteristic to all pattern forming systems. In this example the missionaries want to convert their opponents, whereas cannibals prefer eating them. The essential prerequisite for the Turing instability is diffusion, which here corresponds to the movement of cannibals and missionaries. The missionaries are assumed to have bicycles and thus they move faster, i.e., they represent the inhibitor of the reaction and slow down the reproduction of cannibals, which in turn are the activator. Should the missionaries not have bicycles, they would always get killed as they meet cannibals, but by having bicycles they have a chance to escape and return where there are more missionaries around. With these definitions the auto-catalytic nature of the Turing mechanism becomes evident: In areas with many cannibals their number will increase due to reproduction, and as a result the cannibals will be even more effective in killing missionaries. On the other hand, the predominance of the cannibals means that more missionaries need to be brought to the island to convert them. If the rate of the cannibal reproduction and missionary boat transport combined with cannibals' running and missionaries' bicycling speed are appropriate, the cannibals and missionaries might finally find a stationary pattern. This pattern would correspond to a map of the island where the areas with cannibal dominance can be marked by one color and the areas with missionary dominance by another color.

Turing patterns were first observed in chemical experiments as late as 1990. In addition to experiments, previous studies of Turing systems have employed analytical mathematical tools and numerical computer simulations in studies of different models exhibiting Turing instability. Apart from physicists also mathematical biologists have been interested in the Turing systems, which have been shown to be able to at least qualitatively imitate many biological patterns such as the stripes of a zebra or spots of a cheetah (see Fig. 1.1) and even more irregular patterns such as those on leopards and giraffes, not to talk about the patterns on exotic fish, butterflies or beetles. Also the segmentation of the fruit fly embryo has been modeled using Turing systems (see e.g. Koch and Meinhardt (1994)). Conclusive evidence connecting Turing systems to formation of animal coat patterns and biology in general is, however, still missing.

Despite the fact that the biological relevance of Turing's work is controversial even today, it had a significant impact on the development of nonlinear dynamics and non-equilibrium physics. Turing gave the first detailed description of a mechanism that can generate order in a non-equilibrium system. In the case of Turing systems the most important prerequisite for the pattern formation process is the difference in the characteristics of the random movement of the chemical molecules due to thermal fluctuations, i.e., diffusion. The special feature of Turing patterns is that their characteristics are determined *intrinsically* by the properties

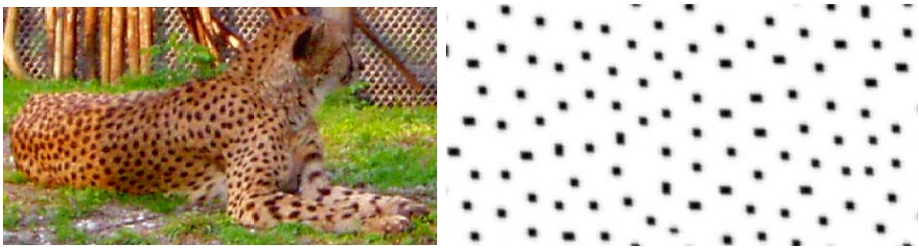

Figure 1.1: For example, the spots of a cheetah can be imitated by using a Turing model. The pattern on the right hand side has been generated by a computer simulation starting from a random state. (Photo: Helmi Leppänen.)

of the chemicals involved and not by external factors. The reaction-diffusion system is kept out of equilibrium by fresh reagents, which are continuously fed into the system. Under certain well-defined conditions this causes a chemical instability, resulting in the formation of a Turing pattern with respect to the chemical concentrations. If the feeding of fresh chemicals is stopped, the pattern will vanish, i.e., the system will return to equilibrium.

Since Turing's goal was to find a generic mechanism, he was aware of the fact that the models he proposed were a severe simplification of any real biological system. In order to construct a manageable model he neglected the mechanical and electrical properties of biological tissue, and instead considered the chemical properties as the crucial factors in biological growth. However, Turing committed suicide only two years after the publication of his only article on morphogenesis, leaving behind a lot of unfinished work. Later it has been found that the relevance of Turing instability is not confined to chemical systems, but also many other physical systems exhibiting dissipative structures can be understood in terms of diffusion-driven instability (Epstein et al., 1992). Turing instability has been connected to gas discharge systems (Astrov et al., 1996; Ammelt et al., 1998), catalytic surface reactions (Falta et al., 1990), semiconductor nanostructures (Temmyo et al., 1997), nonlinear optics (Tlidi et al., 1997), irradiated materials (Walgraef and Ghoniem, 2003) and surface waves on liquids (Barrio et al., 1997).

In general, according to the second law of thermodynamics, a *closed* system always maximizes its entropy. This means that if a system is not in an equilibrium state, it will move towards it. In nature, a seed can remain in an equilibrium state for a long time before it germinates. If it finds its way into nutritious soil the seed develops branches that become the stem and roots of the plant. As a structure arises the entropy decreases locally, which seems to contradict the second law of thermodynamics. Thus, it was long thought (and some people still do) that science cannot explain the origins of life. To overcome this reasoning, the most important

point to notice is that natural systems are not closed systems, but are in constant interaction with their environment. It was not until 1950s when the scientific community began to understand that there are many analogous open systems, ranging from chemistry to hydrodynamics. The constant external feeding of energy into a system keeps the system away from equilibrium, and hence the dynamics of the system are not anymore governed by the rules of equilibrium thermodynamics, thus enabling self-organization of dissipative structures and many other interesting phenomena. For example, a human being is an open dissipative non-equilibrium system that has to keep up a constant influx of energy by eating. The energy is consumed in resisting the universal increase of entropy to maintain the structure of the body. If a human being stops eating, the entropy will win the competition causing the body to break down.

The pattern formation behavior in Turing systems is very complex. In this thesis a Turing model called the Barrio-Varea-Aragon-Maini (BVAM) model is studied employing computational methods. We have focused on the dynamics of the BVAM model under different conditions in both two- and three-dimensional domains by employing large-scale computer simulations. The results of the numerical simulations were justified and validated by analytical treatment of the BVAM model using both *linear stability analysis* and *nonlinear bifurcation theory*. In our work, the emphasis is on extending the present knowledge concerning the characteristics of Turing structure formation in three dimensions as compared to two-dimensional Turing pattern formation.

The purpose of Chapter 2 is to introduce the reader to the field of pattern formation on a general level and to position the subject matter of this thesis to a larger context. Some basic concepts related to pattern formation are reviewed and two extensively studied classes of systems showing pattern formation, namely hydrodynamical systems and chemical reaction-diffusion systems are discussed. This chapter is concluded by a brief introduction to pattern formation in natural systems and to the biological relevance of Turing's ideas.

The focus of Chapter 3 is specifically on the chemical reaction-diffusion systems that exhibit Turing instability. First, the idea of Turing instability is discussed at an abstract level followed by a sketch of the formal methods available for treating Turing systems. Then three well-known Turing models are introduced to get some insight to Turing models in general. Finally, we discuss an experimental CIMA reaction showing Turing patterns and review some other recent experimental work.

Chapter 4 presents the results of our original work in the context of the BVAM model. First, the model is derived and scaled followed by the linear stability analysis in order to determine the unstable wave vectors and the parameter sets resulting in the Turing instability. Then, pattern selection in the BVAM model is studied by using nonlinear bifurcation analysis in both two- and three-dimensional systems. The methods are presented in a detailed manner starting from the deriv-

ation of the amplitude equations for different symmetries, followed by the center manifold reduction and stability analysis of the resulting amplitude equation systems. The nonlinear analysis yields the parameter regimes corresponding to morphologically different patterns and bistability.

The main results of this thesis are presented in Chapter 5. First, the numerical procedure for solving the BVAM model is introduced and analyzed. Then, some general result of Turing pattern formation in both two- and three-dimensional domains are presented, and the difference between Turing pattern formation in two and three dimensions is discussed. Next, the robustness of the Turing mechanism is studied by introducing Gaussian noise in the system, which is followed by a broad study of morphological transitions and the effects of bistability. Then, the effect of the domain growing from a two-dimensional plane to a three-dimensional slab is studied. The results are concluded by a study of spatio-temporal dynamics in the BVAM model due to competing bifurcations and multistability.

Finally, in Chapter 6 the most important ideas presented in this thesis are reviewed and the biological relevance of our results and Turing pattern formation is discussed in general.

Chapter 2

Some general aspects on pattern formation

The appearance of dissipative structures due to a spontaneous symmetry-breaking is a phenomenon occurring in a variety of non-equilibrium systems. Dissipative structures exist far from equilibrium and differ from typical equilibrium structures (e.g. crystals) in that they are kept in a steady-state by ongoing dynamical processes feeding energy into the system. The structures persist by dissipating the input energy, which makes non-equilibrium processes irreversible. Dissipative structures are typically macroscopic and the characteristic length scale of the structure is independent of the size of the individual constituents (e.g. molecules) of the system.

The formal theory of pattern formation is based on non-equilibrium thermodynamics (see e.g. De Groot and Mazur (1962)) and was pioneered by the Russian chemist Ilya Prigogine. The research was carried out in Brussels from the 1940s to 1960s by Prigogine and coworkers. They extended the treatment of thermodynamical systems to the nonlinear regime far from equilibrium and applied bifurcation theory to analyze state selection (Prigogine and Lefever, 1968; Nicolis and Prigogine, 1977). In 1945 Prigogine had suggested that a system in non-equilibrium tries to minimize its rate of entropy production and chooses the state accordingly. This condition was proved to be inadequate by Landauer (1975), who argued that minimum entropy production is not in general a necessary condition for the steady-state and that the most favorable state of the system cannot be determined based on the behavior in the vicinity of the steady state, but one must consider the global non-equilibrium dynamics. Nevertheless, in 1977 Prigogine was awarded the Nobel price in chemistry for his contribution to the theory of dissipative structures. Later studies have developed new techniques for analyzing pattern selection (Pismen, 1980; Newell et al., 1993; Gunaratne, 1994; Ipsen et al., 2000) and spontaneous symmetry-breaking in dissipative systems (Walgraef et al.,

1980, 1981; Pismen, 1994; Callahan and Knobloch, 2001). It should be noted, however, that the theory of non-equilibrium thermodynamics is still incomplete.

The exact definition of pattern formation is somewhat ambiguous since there are numerous systems showing some sort of organized behavior. In this thesis we will not discuss self-organized criticality, where the emphasis is on the description of the universal characteristics of the resulting configurations instead of the mechanism resulting in self-organization behavior (Bak et al., 1987). On one hand, pattern formation can be considered to refer to any process that gives rise to some kind of observable patterns or in a more general sense increase of order in the system. On the other hand, the definition may require that the mechanism behind the patterns has particular characteristics. Haken (1977) has tried to capture the general phenomena under the name synergetics, referring to the cooperation of different effects, whereas Nicolis and Prigogine (1977) have called similar phenomena self-organization of dissipative structures.

The point of view to pattern formation that is adopted here is little different. Here the pattern formation is seen as a *dissipative non-equilibrium process, where local rules (interaction or reaction) or external constraints (time or length scales) govern the global organization*. There are numerous physical systems exhibiting dynamical behavior that satisfy the above definition (see e.g. Gollub and Langer (1999) and (Rabinovich et al., 2000)). Certain hydrodynamical systems and chemical reaction-diffusion systems are good examples of pattern formation and will be discussed in more detail in Secs. 2.2 and 2.3. Other problems related to the pattern formation according to the above definition include periodically vibrated systems (e.g. granular media (Melo et al., 1995) or Faraday experiment (Barrio et al., 1997)), interface dynamics (e.g. solidification, viscous fingering, dendritic growth) (Cross and Hohenberg, 1993; van Saarloos, 1998) and nonlinear optics (Tlidi et al., 1997). It should be noted, however, that, for example, self-organization in amphiphilic systems (Chaikin and Lubensky, 1995) or in block co-polymer melts (Matsen and Bates, 1996; Groot and Madden, 1998; Groot et al., 1999) are excluded by the definition, since they are dynamical equilibrium processes driven by minimization of the free energy, i.e., there is not a constant external driving maintaining the non-equilibrium conditions, but rather the system is evolving towards the equilibrium.

One of the challenges in studying pattern forming systems is the analysis of the patterns themselves. How can one define what is a real pattern as opposed to something random, characterize the properties of a pattern and differentiate between patterns? In essence, many pattern forming systems may result in striped or spotty patterns. Thus if you see a picture of a two-dimensional hexagonal lattice of spots, by looking at it you cannot determine, whether the structure was generated by chemicals in a gel, laser light in a cavity or charges on the surface of a semiconductor. This should be duly noted, since the great variety of patterns that can be observed in nature has inspired researchers to propose descriptive models

for biological pattern formation. Patterns in natural systems and their mathematical modeling will be discussed in Sec. 2.4.

2.1 Basic concepts

There are some basic concepts that should be introduced before discussing problems related to nonlinear dynamics and pattern formation. *Bifurcation* refers to a qualitative change in the dynamics of a system. At the bifurcation point, the *stability* of stationary states typically changes. We write a differential equation for an n-component reaction system as

$$\frac{d\mathbf{W}}{dt} = f(\mathbf{W}, \theta), \tag{2.1}$$

where $\mathbf{W} = (w_1, \ldots, w_n)^T$ stands for the n species w_i, θ holds the parameter values and f is a typically nonlinear function of the species and parameters. Eq. (2.1) describes a spatially homogeneous system since spatial dependence of $\mathbf{W}$ in the form of diffusion operator (∇^2) is missing. The behavior of the system can be adjusted by the control parameter included in θ that defines the distance to the thermal equilibrium state or to the onset of the pattern forming instability. Around some critical value θ_c the system undergoes a bifurcation, which leads to the *spontaneous symmetry-breaking* and ordering at the macroscopic level.

2.1.1 Symmetry-breaking

Spontaneous symmetry-breaking is one of the key concepts while discussing bifurcations in non-equilibrium systems (corresponding to phase transitions in equilibrium systems). The phenomena can be understood by considering equilibrium phase transitions such as the liquid-solid phase transition, where homogeneous liquid becomes a fixed crystal. Another example is the Ising model, which shows a disordered structure at high temperatures with magnetization $\langle m \rangle = 0$ and as the temperature is lowered the system undergoes a second-order phase transition into the *symmetry-broken phase* with spins pointing coherently either up or down (see Fig. 2.1).

As a non-equilibrium example let us consider a thin metal strip mounted to a piece of wood. The strip has a weight attached to it and the height of the weight can be adjusted. As the weight is low enough ($h < h_c$) the strip will stand straight and oscillate around the vertical state if perturbed. As the weight is moved higher ($h > h_c$), the strip becomes unstable to perturbations. The strip will bend either to the left or right due to gravity and the flexibility of the strip. Upon bending the mirror symmetry is broken with respect to the vertical axis. If the system is then perturbed again, it will oscillate around the bent state. The situation is

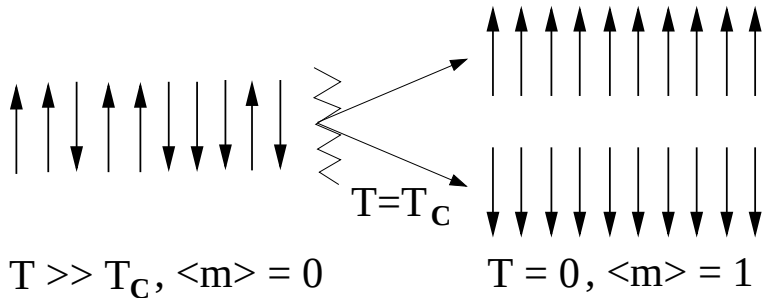

Figure 2.1: The symmetry-breaking phase transition in the Ising model occurs at $T = T_c$. At high enough temperatures $T >> T_c$ the system is disordered. As the temperature decreases the system enters the broken symmetry phase with the spins pointing either up or down.

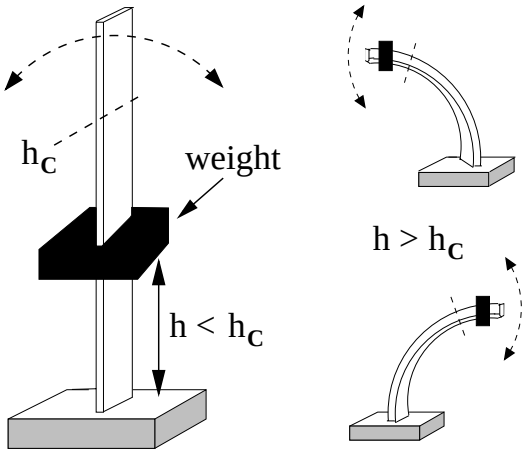

Figure 2.2: A metal strip with a weight illustrating a system undergoing a spontaneous symmetry-breaking via a subcritical pitchfork bifurcation as the height of the weight is altered. The dashed arrows describe the oscillations around the steady-states due to perturbations.

illustrated in Fig. 2.2. It should be noticed that the system is driven by gravity. In the absence of gravity the value of the bifurcation parameter, i.e., the height of the weight (h), does not affect the behavior of the system. Then the bent states do not exist for any value of h and the spontaneous symmetry-breaking does not occur. The behavior of the system describes very well the pitchfork bifurcation, which will be discussed later.

Chemical reaction-diffusion systems exhibiting pattern formation, such as the

Turing systems studied in this thesis, are analogous to the non-equilibrium case. In chemical systems the spontaneous symmetry-breaking occurs due to an instability as the feed rate of a chemical exceeds certain threshold value. The initial state is typically just a homogeneous state with random fluctuations, whereas the final state is a highly organized pattern with respect to the chemical concentration. The exact form of the resulting pattern is determined by the initial fluctuations (corresponding to the metal strip bending either to the left or to the right), whereas the general features of the morphology are governed intrinsically by the reaction and diffusion rates of the chemicals (corresponding to deviation of the metal strip from the vertical line, which is the same whether the strip bends to the left or right).

2.1.2 Stability

Stability refers to a system's ability to resist small perturbations. A system is in a stationary state, when it satisfies the condition $\partial \mathbf{W}/\partial t = 0$ in Eq. (2.1). Let us denote this solution by $\mathbf{W}_s$ such that $f(\mathbf{W}_s, \theta) = 0$. Next we introduce a time-dependent perturbation denoted by $\mathbf{w}(t)$. Now the state $\mathbf{W}(t)$ of the system can be written as

$$\mathbf{W}(t) = \mathbf{W}_s + \mathbf{w}(t). \tag{2.2}$$

There are two different definitions of stability. The state $\mathbf{W}_s$ is *stable in the sense of Lyapunov* if the perturbed system never deviates "very far" from $\mathbf{W}_s$. On the other hand, the state is said to be *asymptotically stable* if it satisfies the previous condition and, in addition, the perturbed system tends to return to the original state $\mathbf{W}_s$ as time goes on. An asymptotically stable system is also stable in the sense of Lyapunov, but the opposite is not always true. If a state is not stable, it is said to be *unstable*.

The idea of stability is intuitive: If we disturb a system by a small amount, an asymptotically stable system returns back to its original state. Figure 2.3 shows schematically the idea of stable and unstable states with the help of three balls. When the ball is on the top of a barrier, as a result of any little perturbation the ball will fall to one of the stable states, A or B. On the contrary, when the ball is in one of the lower stable states, it will stay there even if it is pushed to the side. It is very important to notice that in the system of Figure 2.3 the direction of the arbitrarily small perturbation fully determines the final state of the system (stable state A or B). This is typical also to non-equilibrium systems.

The above discussion can be formulated mathematically as follows: if a norm $\| \cdot \|$ is defined in the phase space then the system is stable in the sense of Lyapunov if for $\forall\, \epsilon > 0$ there $\exists\, \delta(\epsilon) > 0$ such that $\forall\, \mathbf{W}_0,\ \| \mathbf{W}_0 - \mathbf{W}_s \| < \delta \ \Rightarrow \| \mathbf{W}(t) - \mathbf{W}_s \| < \epsilon$, for $\forall\, t \geq 0$. The system is asymptotically stable if, in addition, $\| \mathbf{W}(t) - \mathbf{W}_s \| \to 0$ as $t \to \infty$.

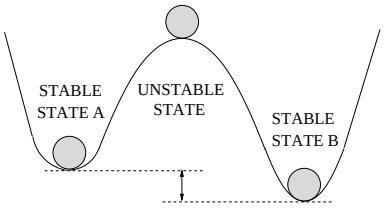

Figure 2.3: A schematic illustration showing three balls in stable and unstable states. The stability of a state is determined by the effects of a small perturbation to that state. If the ball is perturbed in the unstable state, the direction of the infinitesimal perturbation determines the resulting state (A or B).

If the dynamics of a system can be captured in the form of an equation such as Eq. (2.1), the stability of a stationary state $\mathbf{W}_s$ can be studied mathematically by using linear analysis (see Sec. 3.1.1 for application to Turing models). The Jacobian $\mathbf{J}$ of the system (Eq. (2.1)) is a matrix with elements defined as $J_{ij} = \frac{\partial f_i}{\partial w_j}$. Now the linear approximation for the system is given by

$$\frac{d\mathbf{W}}{dt} = \mathbf{A}(\mathbf{W} - \mathbf{W}_s), \tag{2.3}$$

where $\mathbf{A}$ stands for the Jacobian $\mathbf{J}$ evaluated at the stationary state $\mathbf{W}_s$. The eigenvalues λ_i of $\mathbf{A}$ determine the stability of the state and the corresponding eigenvectors span the stable and unstable subspaces. If one or more of the real parts of the eigenvalues λ_i are positive, the state is unstable.

The stationary states can be classified further according to the imaginary parts and signs of the corresponding eigenvalues. For example, in a two-dimensional phase space there are five types of fixed points: stable and unstable foci (imaginary eigenvalues with non-zero real part), stable and unstable nodes (real eigenvalues) and saddle-nodes (real eigenvalues with different sign). In addition, there is a further possibility for the state of the system, namely the limit cycle, which corresponds to temporal oscillations with a fixed frequency. For a more detailed discussion of the stability of fixed points, see e.g. Stich (2003).

As an example, let us consider the Fisher-Kolmogorov kinetics in the absence of diffusion given by

$$\frac{dw}{dt} = \theta w - w^3, \tag{2.4}$$

where w describes a real field (e.g. concentration) and θ is the bifurcation parameter of the model. The stationary states of Eq. (2.4) are given by $w_s^1 = 0$ for all θ and $w_s^{2,3} = \pm\sqrt{\theta}$, for $\theta > 0$. Since we are dealing with only one equation rather than a system, the Jacobian reduces to a single derivative of the kinetics given by $\theta - 3w^2$. The evaluation of this derivative at the stationary state w_s^1 yields θ and

$w_s^{2,3}$ yields -2θ, which follows that for $\theta < 0$ there exists only one stable state w_s^1. For $\theta > 0$, w_s^1 becomes unstable and two additional stable stationary states $w_s^{2,3}$ arise. The above stability scenario corresponds to the supercritical pitchfork bifurcation at $\theta_c = 0$, which will be introduced next.

2.1.3 Bifurcations

A bifurcation can be defined as a qualitative change in the topology of the phase space of a system. It occurs due to a change in the value of the *bifurcation parameter* θ resulting in a spontaneous symmetry-breaking. In practise this can be observed as the appearance of a new stationary state or as changes in the stability of the stationary states. The are many types of bifurcations, for example, the saddle-node bifurcation, pitchfork bifurcation and Hopf bifurcation. Their names refer to different kinds of changes in the topology of the phase space. Bifurcations may also be classified as subcritical and supercritical depending on the direction of the bifurcation. A further classification is based on the *co-dimension* of the bifurcation, which more or less tells the number of parameters that have to be adjusted in order to find the bifurcation point.

In the case of a saddle-node bifurcation, a stable node and an unstable saddle point appear above the bifurcation point θ_c. An example of a saddle-node bifurcation is given by the equation $w_t = \theta - w^2$. For $\theta < 0$ this equation has no (real) stationary states, but for $\theta > 0$ it has a stable and an unstable stationary state with opposite signs. The bifurcation takes place at $\theta_c = 0$ and is schematically illustrated in Fig. 2.4A. A supercritical pitchfork bifurcation takes place as the only stationary state loses stability and two new stable stationary states appear. This situation corresponds to the case of the metal strip with a weight (see Sec. 2.1.1) and it was also illustrated earlier using the Fisher-Kolmogorov kinetics. The corresponding bifurcation diagram is presented in Fig. 2.4B. The bifurcation parameter θ corresponds to quantity $h - h_c$ in the metal strip system and the w corresponds to the deviation from the vertical state. A Hopf bifurcation illustrated by Fig. 2.4C corresponds to a pair of imaginary eigenvalues crossing the real axis and it results in a limit cycle with oscillations. The bifurcation diagrams presented in Fig. 2.4 correspond to a co-dimension-one bifurcation, since the bifurcation point is adjusted by only one parameter θ. For a more detailed discussion of bifurcation types and their characteristics the reader is referred to Strogatz (1994).

The bifurcation diagrams in Fig. 2.4 may be easier to understand, if one considers the bifurcation as a continuous deformation of a phase space landscape such as is shown in Figure 2.3. For example, the saddle-node bifurcation corresponds to a monotonous landscape rising from one point (creating an unstable state) and lowering from another point (creating a stable state). The supercritical pitchfork bifurcation, on the other hand, corresponds to a convex curve (with the peak at

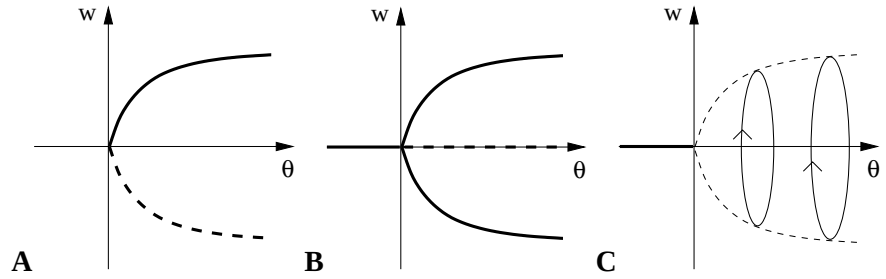

Figure 2.4: The schematic bifurcation diagrams corresponding to A) a saddle-node bifurcation, B) supercritical pitchfork bifurcation and C) Hopf bifurcation (limit cycle). Solid lines correspond to stable states, whereas dashed lines correspond to unstable states. Here the critical value of the bifurcation parameter is assumed to be $\theta_c = 0$.

W_s) deforming to the form of the landscape in Figure 2.3, where W_s would be the unstable state.

Bifurcations can also be analyzed based on the eigenvalues and the corresponding eigenvectors determined by the linear stability analysis around a particular stationary state (see Sec. 2.1.2). The eigenvectors span the stable ($\lambda_i < 0$) and unstable ($\lambda_i > 0$) subspaces, E^s and E^u of a stationary state. The center subspace E^c is spanned by the eigenvectors of the bifurcating eigenvalues. These subspaces are (linear) approximations of the full nonlinear dynamics described by the corresponding unstable, center and stable manifolds W^u, W^c and W^s (see Crawford (1991)). The *center manifold* is the surface separating the unstable and stable manifolds in the space spanned by the nonlinear generalizations of subspaces E^s, E^u and E^c.

The *center manifold theorem* states that the full dynamics of a nonlinear model can be reduced to the center manifold near a bifurcation point. The dynamics on the center manifold is described by normal forms or amplitude equations, which are universal, i.e., all systems showing certain bifurcation have the same dynamics on the center manifold (Crawford, 1991). The amplitude equations can be expressed in terms of the parameters of the original system by devising a mapping from the concentration space to the center manifold of the wave vector space. This reduces the dimensionality of the problem from the dimension of the phase space (described by PDEs) to that of the center manifold (described by ODEs). For a rigorous mathematical justification of the method we refer the reader elsewhere (Crawford, 1991; Callahan and Knobloch, 1997; Dionne et al., 1997). In relation to Turing systems the center manifold reduction can be used to study pattern selection and will be applied on the BVAM model later in this thesis (see sections 3.1.2 and 4.3). *Turing bifurcation* is different from the other bifurcations discussed above in that the number of stationary states does not change, but merely

a stationary state becomes Turing unstable resulting in a Turing instability (see Sec. 3.1).

2.2 Hydrodynamical systems

The behavior of hydrodynamical systems is related to motion of fluids. In this section we introduce the reader to two phenomena related to a hydrodynamical instabilities, namely Rayleigh-Bénard convection and Taylor-Couette flow. In the former, patterns arise due to a thermal gradient and in the latter due to the centrifugal force. A dimensionless control parameter determining the onset of the instability can be derived for both of these systems.

2.2.1 Rayleigh-Bénard convection

The Rayleigh-Bénard experiment concerns the problem of thermal convection and was first performed by Bénard in 1900. It was not until sixteen years later, when Lord Rayleigh explained the phenomenon theoretically. Although the experimental setup is simple, the system displays very rich behavior (see e.g. Elder et al. (1992) or Ball (2001)). For example, the motion of continental plates resulting in earthquakes is caused by convective motion of magma in the mantle of the earth. Also many weather phenomena are related to convection.

The idea of Rayleigh-Bénard convection is illustrated in Figure 2.5. Consider a fluid placed between two infinite parallel horizontal plates, which are assumed to be perfect heat conductors. If the temperature of the lower plate is denoted by T_1 and the upper plate by T_2, and the temperature difference between the lower and upper plates is given by $\Delta T = T_1 - T_2$. If $\Delta T < 0$, both conducting and convective states of the fluid are stable. If ΔT is positive, but small, the thermal conduction from lower to upper plate occurs and the temperature profile between T_1 and T_2 becomes linear. The fluid will remain at rest since the viscosity and thermal conduction are able to stabilize the system against small perturbations: viscosity generates internal friction opposing movement and dissipative effects of thermal conduction tend to restore the displacements.

As ΔT exceeds a certain threshold ΔT_c, thermal expansion makes the fluid near the lower plate substantially less dense than the colder fluid above. This is an unstable situation in the gravitational field. The warmer fluid near the lower plate rises due to buoyant force, but there is no space for it above. Thus some of the colder molecules must be brought down by gravity to make space for warmer molecules. The ongoing process forms so-called Bénard cells, where fluid moves in rolls (see Fig. 2.5). The up and down movement is distributed spatially with a periodicity proportional to the distance between the plates.

It should be noted that in the case of Rayleigh-Bénard convection the characteristic length scale (width of Bénard cells) is determined by an external length

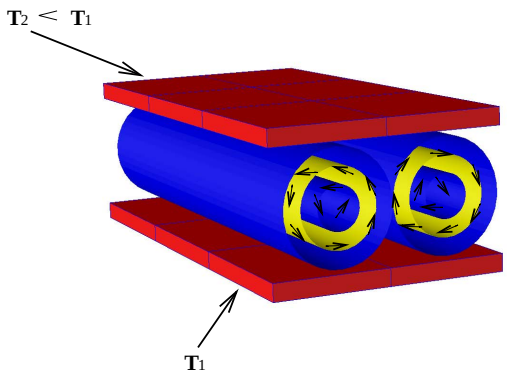

Figure 2.5: The idea of Rayleigh-Bénard convection. As the temperature difference between the bottom and top plates exceeds the threshold value ΔT_c, Bénard cells are formed and the fluid starts to move in rolls to opposite directions in the neighborhood cells. The situation shown in the figure is ideal and in reality the cells are not always parallel and defectless. (Image: Ville Mustonen.)

scale (separation of plates), whereas for example in the context of chemical instabilities the characteristic length of the resulting patterns is often determined by the properties of the chemicals that are intrinsic to the system. It should also be noticed that from the macroscopic point of view the system is stationary, since the velocity, temperature and density at a given point are time-independent and only the fluid molecules are moving.

The Rayleigh-Bénard convection can be analyzed by employing dimensional analysis (Barenblatt, 1987). Dimensional analysis is based on isolating the factors that are relevant to the phenomena and deriving a dimensionless control parameter that captures the essentials of the problem without knowledge of the exact mechanism.[1] The relevant dimensions of the Rayleigh-Bénard convection problem are given in Table 2.1.

As $\Delta T > \Delta T_c$ the warmer and lighter fluid on the bottom is moved upwards by a buoyant force per unit volume given by $\alpha\rho g\Delta T$. On the other hand, the motion of the fluid molecules is resisted by a friction force, which is a combination

[1] Incidentally, it could be mentioned that in 1950 G. I. Taylor used dimensional analysis to determine the energy of American nuclear bombs based on a governmental PR-video of a nuclear explosion and published his "top secret" findings in the Proceedings of the Royal Society of London (see Barenblatt (1987) for details).

Dimension	Notation	Unit
temperature difference between plates	ΔT	K
mass density of the fluid	ρ	kg/m^2
acceleration of gravity	g	m/s^2
thermal expansion coefficient of the fluid	α	$1/K$
kinematic viscosity of the fluid	ν	$1/K$
thermal diffusivity	κ	m^2/s
separation between plates	d	m

Table 2.1: The dimensions of Rayleigh-Bénard convection problem

of the effects of fluid viscosity and stabilizing thermal conduction. This dissipative force per unit volume can be written as $\nu\kappa\rho/d^3$. Consequently, the Rayleigh number R, i.e., the control parameter of the Rayleigh-Bénard system is defined as the ratio of the two forces

$$R = \frac{\alpha g \Delta T d^3}{\kappa \nu} \tag{2.5}$$

One should note that the Rayleigh number is indeed a dimensionless or unitless combination of system parameters and it is independent on the mass density of the fluid. It is widely known that instability occurs at $R_c \approx 1708$ (Cross and Hohenberg, 1993). At this dimensionless number the state of the fluid changes from conductive to convective and the critical point is dependent only on the value of this specific combination of parameters and independent of the fluid.

More rigorous analysis of the Rayleigh-Bénard instability requires a microscopic description for the velocity field in the fluid with help of the Navier-Stokes equation. Swift and Hohenberg (1977) have studied the dynamics of the system with help of reduced dynamics at the onset of the instability. By writing an amplitude equation for the critical mode that grows due to deviations from the linear temperature profile they obtained a model, which describes the spatio-temporal changes in the system. The scaled model with spatial dependence is of the form

$$\frac{\partial \phi}{\partial t} = \epsilon\phi - (\nabla^2 + 1)^2\phi - \phi^3, \tag{2.6}$$

where ϕ is an order parameter describing the vertical velocity of fluid molecules.

The Swift-Hohenberg model is asymptotically exact in the limit $R \to R_c$ and it produces patterns that are similar to the ones observed in the experimental systems. The model succeeds very well in capturing the essential features of the system and enables detailed studies of the pattern formation mechanism (see e.g. Elder et al. (1992)). For example, Cross and Hohenberg (1993), who offer a detailed explanation of the analytical treatment of the system, list some drawbacks of the Swift-Hohenberg equation. Figure 2.6 shows a pattern obtained from a

Figure 2.6: Computer simulation of Rayleigh-Bénard convection using the Swift-Hohenberg model. The view is from above. Notice that the convective cells are not ordered as in the ideal situation of Figure 2.5. The dark and light colors denote the domains with upward movement (warmer sparse liquid) and downward movement (cooler dense liquid), respectively. (Image: Mikko Karttunen, Helsinki University of Technology.)

computer simulation of the Swift-Hohenberg model (Eq. (2.6)). In addition to the labyrinthine striped pattern the model exhibits also hexagonal spotty patterns.

2.2.2 Taylor-Couette flow

Taylor-Couette flow is analogous to Rayleigh-Bénard convection in that it also involves fluid moving in rolls. A Taylor-Couette instability may take place in a fluid layer confined between two concentric cylinders rotating at rates Ω_i and Ω_o. The difference in the angular frequencies between the inner and outer cylinders $\Omega = \Omega_i - \Omega_o$ is the control parameter of the system (with critical value Ω_c). If only the outer cylinder is rotating, i.e., $\Omega_i = 0$ a stable laminar shear flow can be observed. If, on the other hand, the inner cylinder is rotating at a high enough rate as compared to the outer cylinder, i.e., $\Omega > \Omega_c$, a turbulent flow is observed in the form of a Taylor-vortex state (see Cross and Hohenberg (1993) or Walgraef (1997)). The experimental setup is illustrated in Fig. 2.7.

In the Taylor-vortex state the fluid moves towards the wall of the outer cylinder and back to the inner cylinder in similar cells as those observed in the context of Rayleigh-Bénard convection. If one separates between fluid moving axially away from the center and towards the center, stripes are observed as a function of height. The Taylor-Couette reactor is essentially a one-dimensional pattern generator. In

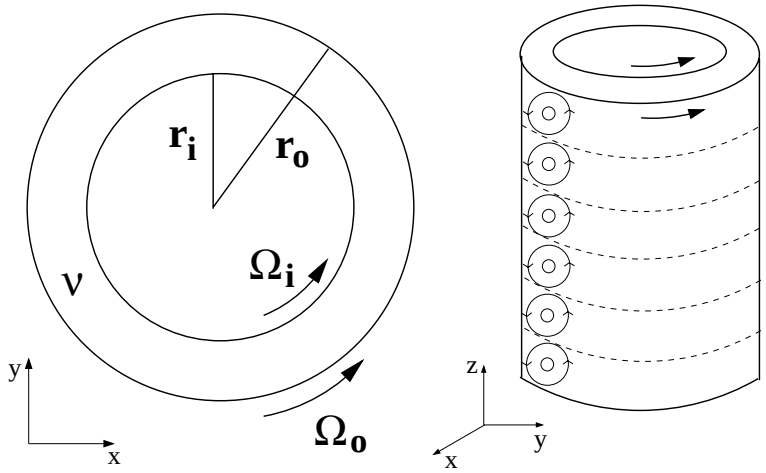

Figure 2.7: In a Taylor-Couette system fluid placed between two concentric rotating cylinders exhibits a turbulent flow in the form of stripes when the angular frequencies $\Omega_i - \Omega_o$ exceeds a certain threshold value. For the explanation of the parameters, see the text.

the Taylor-Couette flow the friction is again due to viscosity, but the destabilizing force is the centrifugal force. More rigorous explanation of the phenomena can be found from Manneville (1990).

The Taylor-Couette instability can be analyzed by employing dimensional analysis in the same way as in the case of Rayleigh-Benard convection. If r_i and r_o are defined as the radii of the inner and outer cylinders, denotes kinematic viscosity of the fluid by ν, the so called Reynolds number can be found as a dimensionless combination of the relevant parameters such that

$$R_e = \frac{r_i r_o (1-\eta)\ \Omega}{\nu}, \tag{2.7}$$

where $\eta = r_i/r_o$. More often one uses the Taylor number defined as $T = 4R_e^2\eta(1-\eta)/(1+\eta)$, which has the critical value $T_c \approx 3416$ above which Taylor-vortices are observed. This approximation is the best when it is assumed that the cylinders are of infinite height and the thickness of the fluid layer is small compared to the radius of the outer cylinder ($\eta \to 1$). After the primary subcritical bifurcation of the laminar flow state to the Taylor-vortex at $T = T_c$ state there are subsequent bifurcations to wavy vortices, modulated wavy vortices and chaotic states Walgraef (1997).

2.3 Chemical reaction-diffusion systems

Chemical systems have been an important part of the field of pattern formation ever since the first experimental observation of chemical oscillations in the early 1950s. Chemical reactions, especially when combined with diffusion, may produce very complex spatio-temporal behavior. Studies of pattern formation in reaction-diffusion systems are based on analytical or numerical studies of mathematical models and experimental chemical systems (see Kapral and Showalter (1995) for a review). Typically a simplified mathematical model is derived describing the essential characteristics of the experimental reaction-diffusion system (Lengyel and Epstein, 1992).

Since this thesis deals with mathematical reaction-diffusion models let us outline the derivation of the reaction-diffusion equation system from the basic principles. Let $\mathbf{w} = (u(\mathbf{x}, t), v(\mathbf{x}, t))^T$ be a vector holding the chemical concentrations of two chemical species at the position $\mathbf{x} \in \Omega \subset \ ^N$ at the time $t \in [0, \infty)$. T denotes a transpose and Ω is an arbitrary simply connected bounded and fixed domain with a closed boundary domain denoted by $\partial\Omega$. Due to the conservation of matter the rate of change of a chemical in Ω is equal to the sum of the net flux of the chemical through the boundary of the domain and the net production of the chemical within the domain. Thus we can write

$$\frac{d}{dt}\int_\Omega \mathbf{w} d\Omega = -\int_{\partial\Omega} F \cdot d\mathbf{S} + \int_\Omega \mathbf{f}(\mathbf{w}) d\Omega, \tag{2.8}$$

where $\mathbf{F} = (F_u, F_v)^T$ is a vector containing the chemical fluxes per unit area and $\mathbf{f} = (f, g)^T$ is a vector of net production rates per unit volume. Applying the Gauss theorem to the first term on the right hand side of Eq. (2.8) one obtains

$$\int_\Omega \left(\frac{\partial \mathbf{w}}{\partial t} + \nabla \cdot \mathbf{F} - \mathbf{f}(\mathbf{w}) \right) d\Omega = 0. \tag{2.9}$$

The integral and differential operator can be interchanged since Ω is fixed and the integrand is bounded. Since Eq. (2.9) holds for any simply connected bounded domain Ω and the integrand is continuous we get

$$\frac{\partial \mathbf{w}}{\partial t} = -\nabla \cdot \mathbf{F} + \mathbf{f}(\mathbf{w}). \tag{2.10}$$

In order to obtain a closed system, we need equations for the fluxes defined by F. According to Fick's law the chemical flux goes from higher to lower concentration. More specifically, the chemical flux is proportional to the concentration gradient. This can be formulated as

$$\mathbf{F} = -\mathbf{D}\nabla\mathbf{w}, \tag{2.11}$$

where the diagonal matrix **D** contains the diffusion coefficients of the chemicals such that $D_{11} = D_u$ and $D_{22} = D_v$. Substitution of Eq. (2.11) to Eq. (2.10) yields the standard form of a reaction-diffusion model

$$\frac{\partial \mathbf{w}}{\partial t} = \mathbf{D}\nabla^2\mathbf{w} + \mathbf{f}(\mathbf{w}). \tag{2.12}$$

The exact form of the reaction kinetics **f** can be derived from the experimental chemical formulae by using the law of mass action (Murray, 1989). For a well-defined differential problem also the initial and boundary conditions are needed. A typical choice is to use the *Neumann zero-flux boundary conditions*, where the system behaves as the boundaries were impermeable. This can be formulated as

$$\mathbf{n} \cdot \nabla \mathbf{w} = 0 \ \ on \ \ \partial\Omega. \tag{2.13}$$

Periodic boundary conditions may also be used and then it would follow that the system behaves as an infinite system provided that it is not too small. The above derivation of a two-component reaction-diffusion system can easily be generalized to any number of chemical species.

Turing systems, which are extensively studied in this thesis, are only one type of reaction-diffusion models and there are numerous other reaction-diffusion models fitting into the generic form of Eq. (2.12). Turing systems produce stationary spatial patterns and satisfy particular conditions related to the destabilization of the stationary state and the competitive reactions of chemical species. In Turing systems pattern-forming phenomena are due to the so-called diffusion-driven instability, which was first discussed by Nicolas Rashevsky in 1938, but Turing gave the first mathematical treatment and analysis of such a model in 1952 (Turing, 1952). Since Chapters 3-5 are devoted to Turing systems we will, in this section, present two other fundamental reaction-diffusion models that exhibit oscillatory dynamics.

2.3.1 Belousov-Zhabotinsky reaction

In the early 1950's a Russian biochemist Boris Belousov observed an oscillation in a chemical reaction while he was experimentally trying to reproduce some processes related to the metabolic cycle of cells. Belousov could not get the results published since he was unable to back up his observations theoretically, which were claimed to contradict the second law of thermodynamics (Ball, 2001). Prior to Prigogine's work (Nicolis and Prigogine, 1977) it was held that entropy has always to increase in a process and thus a chemical oscillation was deemed to be impossible with entropy increasing and decreasing by turns. It was not before the late 1960s, when Zhabotinsky confirmed Belousov's findings and it was noticed that the reaction first observed by Belousov exhibits a pattern formation mechanism with similarities to the mechanism Turing had proposed. However, it is

important to remember that the Belousov-Zhabotinsky reaction produces traveling waves, whereas Turing patterns are time-independent.

The basic mechanism of Belousov-Zhabotinsky (BZ) reaction consists of cerium-catalyzed oxidation of malonic acid in an acid medium by bromate ions. According to the mechanism suggested by Field et al. (1972) the whole process involves 10 different reactions of 14 different chemical compounds. Oscillations are observed with respect to the concentration ratio of the cerium ions $[Ce^{4+}]/[Ce^{3+}]$ and the bromide ion concentration $[Br^{-}]$ (see e.g. Murray (1989)). Field and Noyes (1974) proposed a mathematical model for the BZ reaction by deriving the reaction kinetics using the law of mass action for the key elements of the reaction. The three-component Oregonator model is given by

$$\begin{aligned} \frac{\partial x}{\partial t} &= qy - xy + x(1-x) + D_x \nabla^2 x, \\ \frac{\partial y}{\partial t} &= -qy - xy + fz + D_y \nabla^2 y, \\ \frac{\partial z}{\partial t} &= x - z + D_z \nabla^2 z, \end{aligned} \tag{2.14}$$

where x, y and z correspond to the scaled concentrations $[HBrO_2]$, $[Br^{-}]$ and $[Ce^{4+}]$, respectively. D_x, D_y and D_z are the respective diffusion coefficients and q and f are parameters that adjusts the dynamics of the model. The Oregonator model exhibits limit cycle oscillations and in the presence of the diffusion term (spatial dependence) the mechanism produces concentric waves (target wave patterns) or spiral waves (see e.g. Murray (1989)). The importance of the Oregonator model arises from the fact that the findings of numerical studies can be readily applied to experimental studies of the BZ reaction and vice versa.

Another model showing a behavior similar to the BZ reaction is the FitzHugh-Nagumo (FHN) model

$$\begin{aligned} \frac{\partial x}{\partial t} &= (x - x^3 - y)/\epsilon + D_u \nabla^2 x, \\ \frac{\partial y}{\partial t} &= x - \gamma y + \delta + D_v \nabla^2 y, \end{aligned} \tag{2.15}$$

where D_u and D_v are diffusion coefficients and ϵ, γ and δ are adjustable parameters. The FHN model was originally developed to describe the function of neural cells and the propagation of neural signals along axons (see e.g. Murray (1989) for an introduction). The FHN model exhibits, in addition to other more complex behavior (bistable and excitable regimes), a Hopf bifurcation and similar spatio-temporal behavior as the Oregonator model. This is why we next turn to the complex Ginzburg-Landau equation, which is the prototype of all such models.

2.3.2 Complex Ginzburg-Landau equation

Reaction-diffusion systems may have different local mechanisms that give rise to global oscillatory dynamics. However, near a supercritical Hopf bifurcation (see Fig. 2.4) the dynamics of all such models can be reduced to the complex Ginzburg-Landau equation (CGLE) which describes the time evolution of the amplitude of the oscillatory mode. This amplitude equation is given by

$$\frac{\partial A}{\partial t} = (1 - i\omega)A - (1 + i\alpha)|A|^2 A + (1 + i\beta)\nabla^2 A, \tag{2.16}$$

where A is the complex amplitude of the oscillation, i is the imaginary unit, and ω, α and β are adjustable parameters. Due to its generic nature the CGLE is perhaps the most studied of all reaction-diffusion models (Schöpf and Kramer, 1991; Weber et al., 1992; Aranson et al., 1998). It shows rich behavior and it has been applied in a variety of contexts. The CGLE shows the typical wave solutions (plane, spiral, target), but also localized coherent structures and even spatio-temporal chaotic behavior. For an introduction to the world of the CGLE model the reader is referred to a review article by Aranson and Kramer (2002).

To deepen our understanding of the CGLE, we present the idea of an analytical treatment of the model in the context of uniform oscillations. A spatially uniform system corresponds to the Stuart-Landau equation, which is simply the CGLE without the diffusion term, i.e.,

$$\frac{dA}{dt} = (1 - i\omega)A - (1 + i\alpha)|A|^2 A. \tag{2.17}$$

By comparing Eq. (2.17) to the Fisher-Kolmogorov kinetics (Eq. (2.4)) discussed in Sec. 2.1.2 it can be noticed that the FK-kinetics actually correspond to the real CGLE. The oscillations exhibited by the Stuart-Landau model have a real amplitude and phase. This can be formulated by writing the complex amplitude as $A = |A|e^{-i\phi}$. The substitution of this trial solution into the Stuart-Landau equation yields two coupled equations describing the time evolution of the amplitude (real) and phase (imaginary) parts

$$\begin{aligned} \frac{d|A|}{dt} &= (1 - |A|^2)|A|, \\ \frac{d\phi}{dt} &= \omega + \alpha|A|^2. \end{aligned} \tag{2.18}$$

The nonlinear nature of this oscillator system is evident form the fact that the changes in the amplitude ($|A|$) and phase of the oscillator (ϕ) are nonlinearly dependent on the amplitude of the oscillator $|A|$. The first equation defines the steady-states $|A_c| = 0$ and $|A_c| = 1$, which yields the constant frequency $\omega + \alpha$. Thus the stable limit cycle is defined by $A(t) = exp(-i(\omega + \alpha)t)$ and it is the only attractor of the Stuart-Landau equation. For a discussion concerning other solutions and the descriptive power of the CGLE see Stich (2003).

2.4 Patterns in natural systems

Alan Turing's (1952) pioneering work in the field of reaction-diffusion systems was inspired by the complexity of self-organizing biological systems. Turing's goal was to understand processes that could explain how a fertilized egg becomes an organism through the process of *morphogenesis* (see Murray (1988) and Maini (2003)). At the beginning the embryo of any mammal is in a spherically symmetrical blastula stage, which is comprised of undifferentiated stem cells. Similarly a seed of a plant is much simpler than the full-grown plant. Both the above mentioned initial stages of a living system contain the knowledge of the final structure in their DNA. For example, the human DNA has only three billion (3×10^9) base pairs, whereas human brain has a hundred billion neural (10^{11}) cells with complex interconnections. The whole human being consists of some tens of trillions of cells (10^{13})! Thus it seems plausible that there are some spontaneous physico-chemical processes that implement the instructions of DNA and drive self-organization. Even if all the orders coded in the genes were found out, biological growth still could not be explained since it is due to complex interaction of various biochemical signals and mechanisms.

The work by Turing belongs to the field of pattern formation, a subfield of mathematical biology. The study of biological pattern formation has gained popularity since the 1970s, when Gierer and Meinhardt (1972) gave a biologically justified formulation of a Turing model and studied its properties by employing computer simulations. As opposed to Turing's ideas, mathematical biology, in general, aims on developing mathematical models that capture the essential characteristics of some biological phenomenon at least qualitatively (Meinhardt, 1982; Mosekilde and Mouritsen, 1995). The main purpose of mathematical biology could also be defined as building models that explain biological phenomena at one hierarchical level by mechanisms at a lower level (Gyllenberg, 2004). For example, collective phenomena can be explained by actions of individuals. In general, mathematical biologists model, for example, population dynamics, biological signaling mechanisms, epidemics and mechanical aspects of morphogenesis such as the development of feathers, teeth or limbs (Murray, 1989, 2003). By understanding not only the function of genes, but also the processes behind physiology, for example diseases, such as cancer, can be studied and understood better (Gatenby and Maini, 2003). Applications of reaction-diffusion schemes in mathematical biology vary from modeling of the growth of bacterial colonies (Mimura et al., 2000) to the propagation of the nerve pulses (Murray, 1989). Another popular way of modeling natural systems have been models that are based on cellular automata. Interestingly, it has been shown by Schepers and Markus (1992) that cellular automata can reproduce patterns typically observed in reaction-diffusion systems (spiral waves and Turing patterns).

The breaking of symmetry in embryos has been speculated to be due to pos-

itional information that arises because of activating genes. According to the hypothesis the genes encoding proteins give rise to morphogen gradients and cells react to their chemical surroundings (see e.g. Hunding and Engelhardt (1995)). The cells that are in the region of high concentration of a morphogen act differently from the cells that are in the region of low concentration. The existence of morphogens has been shown in the experiments by developmental biologist. Some 15 years ago researchers identified protein *bicoid* to be responsible for organization of the fruit fly embryo. The first experimental evidence of morphogens in vertebrates has been obtained very recently in zebra fish embryo (Chen and Schier, 2001) and nowadays there is also some very detailed knowledge available concerning the forces related to morphogenesis (Hutson et al., 2003). Recent results in the context of microtubule self-organization (Tabony et al., 2002) would suggest that gravity can cause a symmetry-breaking in a reaction-diffusion system, which is very favorable for the biological applicability of Turing systems. A reader interested in detailed explanations and modeling the formation of biological structure is advised to start from the review article by (Koch and Meinhardt, 1994).

One of the most intriguing applications of mathematical biology and Turing systems has been the modeling of animal coat patterns such as the spots of a cheetah and stripes of a zebra. More exotic patterns include the polygonal patterns of giraffes and tubular arcs of leopards. For example, Murray (1989) and Koch and Meinhardt (1994) offer many examples of Turing models that can imitate the above mentioned as well as other animal patterns. Also the patterns found on fish (Kondo and Asai, 1995; Barrio et al., 1999), butterflies (Sekimura et al., 2000) and beetles (Liaw et al., 2002) have been modeled using Turing models. According to James Murray's hypothesis it is assumed that the Turing model describes morphogens spreading on the skin of an animal. After the pattern is established the melanocytes, i.e., the pigment producing cells in the skin differentiate and start to produce either eumelanin (black/brown) or phaeomelanin (yellow/orange). The melanocytes are well understood apart from the fact how the color they produce is determined.

The most important feature of the Turing models is that they generate the pattern with respect to the chemical concentration from any arbitrary initial state and the pattern can be changed from stripes to spots by changing only one parameter of the model. In a biological system this would correspond to a small change in the production of a morphogen. Turing himself was aware that any merely chemical model trying to explain biological growth is a too simplified, but he emphasized the importance of understanding the general mechanisms. While pursuing a holistic view of natural systems one has to start from a theoretical model that neglects factors that are assumed to be of secondary importance. Naturally there have also been some bottom-up approaches. For example, experimentally backed up protein dynamics of cell division has been modeled using reaction-diffusion equa-

tions (Howard et al., 2001; Howard and Rutenberg, 2003). Also the distribution of ATP in the cell cytoplasm has been modeled with a Turing model (Hasslacher et al., 1993).

In addition to their simplicity and generic nature, Turing systems have also many other desirable features as theoretical models for morphogenesis. The Turing models generate non-uniform spatial distributions thus enabling greater complexity as compared to simple gradients. The models describe the effects of the spatial geometry of the domain on the pattern formation. In addition, the chemical evolution and the final Turing structures are very robust against random noise and distortions (see Sec. 5.3) as are most natural systems. Turing models are an example of very simple and generic mechanism showing an amazingly complex behavior and in addition to their descriptive power they have a connection to some very fundamental ideas of non-equilibrium systems.

However, there are some drawbacks in applying reaction-diffusion mechanism to animal patterns. First, there is not enough experimental evidence of the existence of morphogens related to patterns on the animal skin. For the models to be plausible, developmental biologists are asking for the identification of morphogens and their reactions such that the models have correspondence to real life. Secondly, the spreading of morphogens in living tissue involves complex biochemical signaling mechanisms, which cannot be captured by the simple diffusion mechanism in the models. Thirdly, also the electrical and mechanical aspects of living tissues should somehow be taken into account in the models, not only chemical processes. In addition, theoretical requirements for the spontaneous symmetry-breaking might not be met in a living tissue since the diffusion constants of many molecules are of the same order of magnitude. The existence of Turing patterns requires a substantial difference in the pace of diffusion between the two chemical species.

It could also be argued that theorists cannot be blamed for the inadequacy of the technology available to the developmental biologists. It should also be remembered that the primary idea of Turing models is not to capture the details, but the salient features of the process. In addition, although all proteins diffuse approximately at the same pace ($\sim 10^{-8} cm^2 s^{-1}$), small molecules diffuse much faster ($\sim 10^{-6} cm^2 s^{-1}$) (Koch and Meinhardt, 1994) and could thus act as morphogen pairs to proteins resulting in a Turing instability *in vivo*.

Although there is no doubt that reaction-diffusion systems can imitate a variety of patterns that animals have on their skin, it is true that the evidence linking Turing systems to biology is still missing. The most convincing evidence of the existence of Turing patterns so far has been presented by Kondo and Asai (1995). They showed that a Turing model could be matched with the stripe formation and stripe addition on two different kinds of angelfish. Not only were they able to imitate the branching of the stripes, but also to relate the time scales of the pattern changes in the real fish to the time scales of computer simulations. Based

on the computer simulations they could estimate the diffusion coefficients of the morphogens on real fish to be of the correct order of magnitude. On the basis of their findings the authors suggest that reaction-diffusion mechanism is a viable mechanism for pattern formation in angelfish. Their claim is plausible, but more conclusive evidence is still needed. The angelfish studies have been extended by Varea et al. (1997), who studied pattern formation in two-dimensional domains of realistic geometry, and by Painter et al. (1999) who increased the biological accuracy of the description by considering the effects of cell movement due to chemotaxis.

Because of the diversity of patterns generated by Turing models, they could probably be used to imitate also many other biological patterns and structures. Three-dimensional Turing structures (see Sec. 5.2.2) vary from planar layers to complex lamellar networks and lattices of droplets. For example, many parts of the human body show mesoscopic periodicity. Radivoj V. Krstić's (1997) has illustrated the three-dimensional structure of human organs in his magnificent ink drawings carefully prepared based on experimental micrographs. His drawings show many structures similar to three-dimensional Turing structures. For example cerebral cortex, cornea of the eye and arteries show layered structure. Many organs and glands could be speculated to correspond to the droplet phase. As an example Fig. 2.8 shows a three-dimensional Turing structure obtained from our numerical simulations (see Chapter 5 for details), where the cellular boundaries and nuclei have been rendered manually. The resulting structure can be seen qualitatively very similar to parenchyma of different organs (see Krstic (1997)).

Recently, Turing systems have been proposed to explain the formation of convolutions found on the cerebral cortex (Cartwright, 2002). It would seem that the organization of human anatomy is probabilistic at the lower level (e.g. all neural connections in the brain are not pre-determined), whereas at the higher level it is guided by some spontaneous physico-chemical processes (e.g. human brain has particular structure), which are controlled by the genes. Whether or not Turing instability is a central part of these physico-chemical processes remains to be studied.

In addition to the various forms and shapes found in living organisms, also many inanimate natural or social systems show self-organizing behavior. For example vegetation patterns and desertification have been modeled using a Turing-type model (von Hardenberg et al., 2001). A reaction-diffusion model has also been suggested for modeling the dynamics of language competition and spreading in societies (Patriarca and Leppänen, 2004). On the other hand, collective behavior of ants has been modeled by using random walker models (Schweitzer et al., 1997). In the book *Self-made tapestry* Philip Ball (1999) gives numerous examples of self-organization ranging from chemical waves with length scales of the order of millimeters to the more than billion times bigger structures of the heavenly bodies. The book is written at a popular level and suitable for anyone,

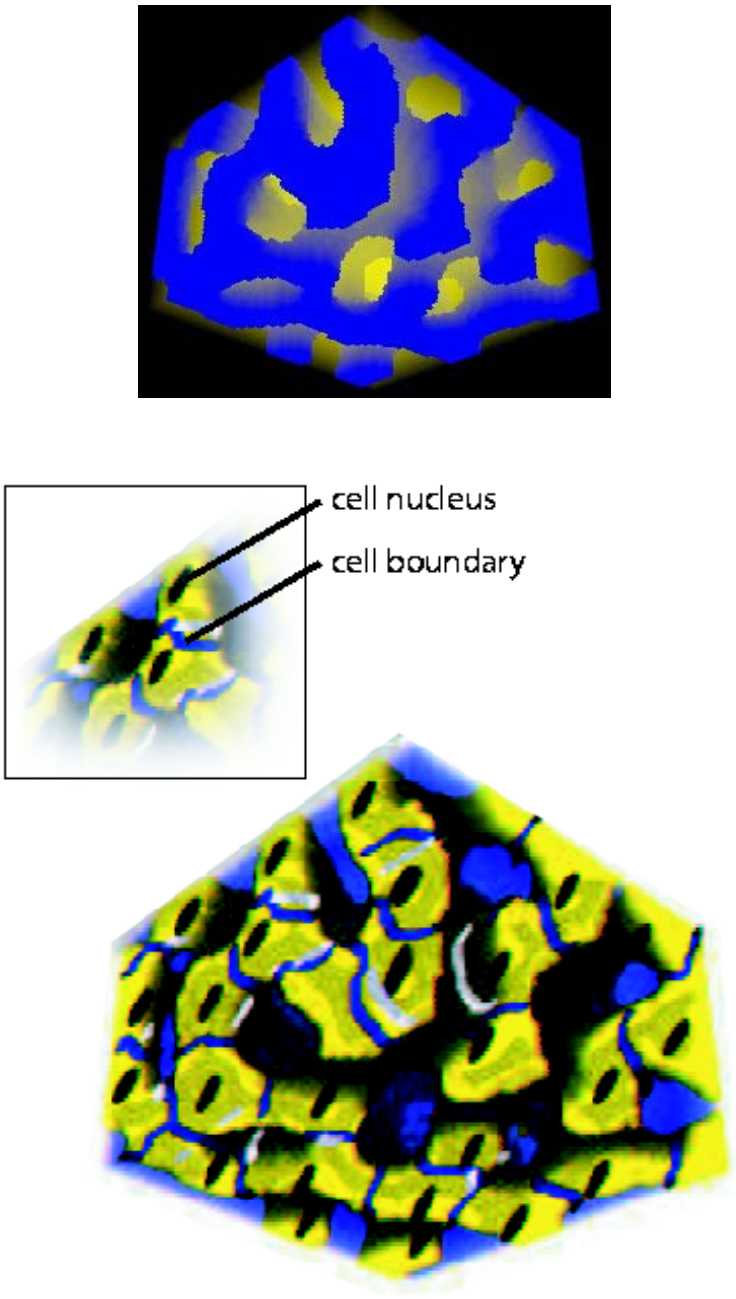

Figure 2.8: Top: Three-dimensional Turing structure obtained from a numerical simulation of the BVAM model (see Chapter 5). Bottom: The Turing structure resembles much the structure of mesenchymal tissue after the cellular boundaries and cell nuclei are manually rendered to the picture. (Image: Murat Ünalan.)

who is interested in the mechanisms behind the morphological richness of the world.

2.5 Summary

In this chapter, the field of pattern formation was introduced by discussing the definition of pattern formation, related concepts and well-known systems exemplifying the phenomenon. According to the author's definition, pattern formation is a dissipative non-equilibrium process giving rise to spatio-temporal behavior governed by intrinsic properties or external constraints. Spontaneous symmetry-breaking is one of the most fundamental concepts related to pattern formation, since it is a prerequisite for the formation of any kind of order into a system. As a bifurcation parameter is varied symmetry-breaking occurs and the system goes through a bifurcation, where the stability properties of the stationary states change. These concepts were illustrated with a standing metal strip, which bends due to perturbations if an attached weight is moved higher. Hydrodynamical systems showing spatially inhomogeneous movement of fluid and chemical reaction-diffusion systems exhibiting temporal oscillations were introduced as examples of pattern formation in non-equilibrium systems. Although there is not yet enough evidence linking Turing systems to biology, Turing systems have indeed been shown to provide a very simple and generic mechanism for imitating many natural formations.

Chapter 3

Pattern formation in Turing systems

A Turing system consists of two or more coupled nonlinear partial differential equations (PDEs), which describe reactions and diffusion of chemicals or *morphogens*. The remarkable feature of the Turing mechanism is that it is capable of generating beautiful time-independent spatial patterns from any random initial configuration provided that particular conditions are satisfied (Murray, 1989).

In its most general form a Turing model describing the time variation of two chemical concentrations U and V due to reaction and diffusion can be written in the form (see Section 2.3)

$$\begin{aligned} \frac{\partial U}{\partial t} &= D_U \nabla^2 U + f(U,V) \\ \frac{\partial V}{\partial t} &= D_V \nabla^2 V + g(U,V), \end{aligned} \tag{3.1}$$

where D_U and D_V are the diffusion coefficients setting the pace of diffusion for chemicals U and V, respectively. For Turing instability to occur the diffusion coefficient of the inhibitor chemical must be larger than that of the activator chemical. The dynamics of the model is determined by the reaction kinetics $f(U,V)$ and $g(U,V)$, which are nonlinear functions of the concentrations. These can be derived from chemical reaction formulae by using the law of mass action and other physical conditions (Murray, 1989). There are many alternatives to the exact form of the reaction terms, some of which are reviewed in Section 3.2. The scalar parameters within f and g govern the pattern selection in the model. Turing models typically generate either linear (2D stripes, 3D lamellae) or radial (2D spots, 3D droplets) structures, although numerous other stable structures are possible (Callahan and Knobloch, 1999) too. Notice that for the reaction kinetics $f(U,V) \equiv g(U,V) \equiv 0$ the system of Eq. (3.1) reduces to two independent diffusion equations.

In this chapter we will discuss the characteristics of Turing systems in general and review some of the work that has been done in the field so far. In the first section we will discuss characteristics of Turing instability and learn the principles of studying Turing systems mathematically. After that three well-known Turing models will be introduced. Finally, this chapter is concluded by an introduction to a real chemical Turing reaction and a brief review of experimental work.

3.1 Turing instability

Turing instability is a phenomenon that causes certain reaction-diffusion systems (Eq. (3.1)) to spontaneously give rise to stationary patterns with a characteristic length scale from an arbitrary initial configuration. The key factor in inducing the instability is diffusion and this is why Turing instability is often called *diffusion-driven instability*. A remarkable feature of Turing systems as compared to many other instabilities in systems out of equilibrium (Cross and Hohenberg, 1993; Ball, 2001) is that the characteristics of the resulting patterns are not determined by externally imposed length scales or constraints, but by the chemical reaction and diffusion rates that are intrinsic to the system. The spirals, target patterns and traveling waves generated by the Belousov-Zhabotinsky (BZ) reaction (see Section 2.3.1) are not due to a Turing instability since they are not stationary and the diffusion rates of the chemicals involved in BZ reaction are usually more or less the same. The difference in the diffusion rates of the chemical substances is a necessary, but not a sufficient condition for the Turing instability (Murray, 1989). In this section, we will present how Turing instability can be formalized and treated analytically.

3.1.1 Linear stability

Linear stability analysis is an often used method for studying the response of the system to perturbations in the vicinity of a fixed point. Introductory illustrations of the linear analysis method can be found in various sources (Murray, 1989; Strogatz, 1994; Nicolis, 1995). In linear analysis one takes into account only the linear terms and thus the results are insufficient for describing the dynamics of the full nonlinear system. However, in the context of Turing systems, within its limitations the method is effective in predicting the existence of an instability and the characteristic wavelength of it.

To introduce the method, let us approach the Turing instability more quantitatively by writing the most general form a reaction-diffusion system (cf. Eq. (3.1)) as

$$\frac{\partial \mathbf{w}}{\partial t} = \mathbf{D}\,\nabla^2\mathbf{w} + \mathbf{F}(\mathbf{w}, \Theta), \tag{3.2}$$

where $\mathbf{w} = (U, V)^T$ is a "vector" containing the concentration fields, the matrix $\mathbf{D}$ holds the diffusion coefficients (for a two-species model in the absence of cross-diffusion: $D_{11} = D_U$, $D_{22} = D_V$, $D_{12} = D_{21} = 0$), and the reaction kinetics is described by $\mathbf{F} = (f(U, V), g(U, V))^T$, which is adjusted by the parameter set Θ including the bifurcation parameter. The homogeneous stationary state $\mathbf{w}_0(\Theta)$ of the system is defined by the zeros of the reaction kinetics, i.e., $\mathbf{F}(\mathbf{w_0}, \Theta) = 0$. The stability of this stationary state can be analyzed by studying the behavior of the system, when a small inhomogeneous perturbation is introduced to the system at state $\mathbf{w}_0$. We write $\mathbf{w} = \mathbf{w}_0 + \mathbf{dw}$, where the perturbation can be written as a spectral decomposition given by

$$\mathbf{dw}(x, t) = \sum_j c_j e^{\lambda_j t} e^{-ik_j \cdot x}. \tag{3.3}$$

Here the spatial part is governed by the wave modes k_j and the temporal part by the corresponding eigenvalues $\lambda_j = \lambda(k_j)$ describing the growth rate of the perturbation. Substituting Eq. (3.3) to Eq. (3.2) and dropping the nonlinear terms one obtains for each k_j the equation

$$|\mathbf{A} - \mathbf{D}k_j^2 - \lambda_j \mathbf{I}| = 0, \tag{3.4}$$

where $k_j^2 = \vec{k}_j \cdot \vec{k}_j$ and in the case of a two-species model the matrix $\mathbf{A}$ is given by

$$\mathbf{A} = \begin{pmatrix} \partial_U f & \partial_V f \\ \partial_U g & \partial_V g \end{pmatrix}_{(U_0, V_0)}, \tag{3.5}$$

where the elements are the partial derivatives of the reaction kinetics evaluated at the stationary state (U_0, V_0). Now Eq. (3.4) can be solved, yielding the so called characteristic polynomial of the original problem (Eq. (3.2))

$$\begin{aligned} \lambda^2 + \left[(D_U + D_V)k^2 - f_U - g_V\right]\lambda + \\ D_U D_V k^4 - k^2(D_V f_U + D_U g_V) + f_U g_V - f_V g_U &= 0. \end{aligned} \tag{3.6}$$

The dispersion relation $\lambda(k)$ predicting the unstable wave numbers can be solved from Eq. (3.6). The growing modes are of the form $We^{i\vec{k}\cdot\vec{r}}e^{\lambda(k)t}$, where W is the amplitude and $\lambda(k)$ is the growth rate defined by the dispersion relation. Thus the wave numbers k with $\mathrm{Re}\{\lambda(k)\}) > 0$ grow exponentially until the nonlinearities in the reaction kinetics bound this growth, whereas the wave numbers k with $Re\{\lambda(k)\} < 0$ will be damped. The schematic example of a real part of a dispersion relation presented in Fig. 3.1 shows a wave window with growing modes and predicts the characteristic length of the pattern.

One can obtain an estimate for the most unstable wave number and the critical value of the bifurcation parameter Θ_C by considering the fact that at the onset of

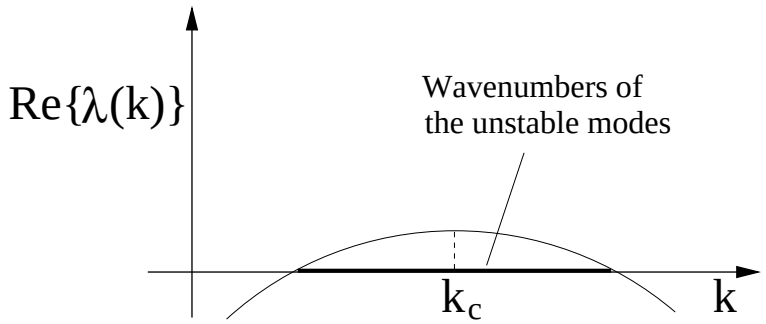

Figure 3.1: A schematic presentation of the real part of a dispersion relation $\lambda(k)$ corresponding to a Turing instability with the most unstable wave number k_c. Other unstable wave modes are all those with $\mathrm{Re}\{\lambda(k_j)\} > 0$.

the instability $\lambda(k_c) = 0$. The term independent of λ in Eq. (3.6) evaluated at k_c has to equal to zero resulting in an equation having only a single solution at the onset. As a result the critical wave number can be written as

$$k_c^2 = \frac{D_V f_U + D_U g_V}{2 D_U D_V} = \sqrt{\frac{f_U g_V - f_V g_U}{D_U D_V}}, \tag{3.7}$$

and the corresponding characteristic length of the pattern is defined by $\lambda_c = 2\pi/k_c$. Furthermore, the critical value of the bifurcation parameter for a Turing bifurcation Θ_C^T above which unstable wave numbers are obtained, can be solved as a function of other parameters from the inequality

$$(D_V f_U + D_U g_V)^2 > 4 D_U D_V (f_U g_V - f_V g_U). \tag{3.8}$$

Further conditions for the Turing instability can be derived based on stability considerations (Murray, 1989; Kapral, 1995) and the *Turing space* consisting of parameters resulting in Turing instability is widely known to be bounded by the inequalities given by

$$\begin{aligned} f_U + g_V &< 0 \\ f_U g_V - f_V g_U &> 0 \\ D_V f_U + D_U g_V &> 0. \end{aligned} \tag{3.9}$$

The Hopf instability or bifurcation is another important instability in reaction-diffusion systems for which the conditions resulting in a stable limit cycle (oscillations) were first formulated by Andronov. In terms of the linearized problem (Eq. (3.4)) the onset of Hopf instability corresponds to the case, when a pair of imaginary eigenvalues crosses the real axis from the negative to the positive

side, i.e., $\mathrm{Re}\{\lambda(k_c)\} > 0$ and $\mathrm{Im}\{\lambda(k_c)\} \neq 0$, whereas $\mathrm{Im}\{\lambda(k_c)\} = 0$ for Turing instability by definition. The critical value of bifurcation parameter for a Hopf bifurcation Θ_c^H can be solved from $\mathrm{Re}\{\lambda(k_c)\} = 0$, which with help of the characteristic equation (Eq. (3.6)) can be written as

$$(D_U + D_V)k^2 - f_U - g_V = 0. \tag{3.10}$$

The so called co-dimension-two Turing-Hopf point is defined by the parameter values that yield $\Theta_c^H = \Theta_c^T$. As discussed in Sec. 2.1.3 the co-dimension of the bifurcations refers to the number of parameters that one has to adjust in order to find the bifurcation point. The interaction between Turing and Hopf instabilities will be studied in Section 5.6.

To summarize, linear stability analysis can be used for predicting the parameter values that result in the Turing instability in a particular reaction-diffusion system. Based on the linear approximation one can also effectively predict the characteristic length of the resulting pattern. In Section 4.2 linear analysis is applied in the context of a Turing model. Linear analysis cannot, however, predict the spatial characteristics of the resulting patterns, since the pattern selection is governed by complex nonlinear dynamics. Thus some more general tools as nonlinear bifurcation analysis are needed.

3.1.2 Pattern selection problem

The linear analysis predicts which wave numbers become unstable in the system, but does not give any insight into symmetries that might arise as a result of nonlinear coupling of the unstable wave modes. Typically, Turing systems (and also many other physical systems) exhibit stripes and hexagonally arranged spots, but also other morphologies such as rhombic arrays and labyrinthine patterns have been observed in two dimensions (Kapral and Showalter, 1995). In three dimensions pattern selection becomes even more complex since there are numerous structures with a characteristic length that can fill a three-dimensional space (Callahan and Knobloch, 1999). The use of amplitude equation formalism makes the analysis of a Turing system universal in the sense that the presentation in terms of the amplitude equations does not capture the dynamics and characteristics of the original chemical system, but only those of the related symmetry groups (Newell et al., 1993; De Wit, 1999).

The study of pattern selection requires nonlinear analysis instead of linear. Typically the concentration fields $\mathbf{w} = (U, V)$ are presented as a superposition of the active Fourier modes that are permitted by the studied symmetry and correspond to the N unstable wave vectors with $|\vec{k}| = k_c$, i.e.,

$$\mathbf{w} = \mathbf{w}_0 \sum_{\vec{k}_j} (W_j e^{i\vec{k}_j \cdot \vec{r}} + W_j^* e^{-i\vec{k}_j \cdot \vec{r}}), \tag{3.11}$$

where $\mathbf{w}_0$ is the an eigenvector of the linear matrix $\mathbf{A}$ in Eq. (3.5). W_j and W_j^* are the time-dependent amplitudes of the corresponding modes $+\vec{k}_j$ and $-\vec{k}_j$. Notice that the sum of complex conjugates is real. The unstable modes have slow dynamics, whereas the stable modes relax quickly and are said to be slaved to the unstable modes. Typically the bifurcation analysis is carried out by observing changes in the stability of the amplitude equation system as a function of the bifurcation parameter, which adjusts the distance to the onset of the instability.

The time variation of the amplitudes W_j and W_j^* is described by a system of ordinary differential equations of the form

$$\frac{dW_j}{dt} = \lambda_c W_j + f_j(W_1, \ldots, W_n), \tag{3.12}$$

where $\lambda_c = \lambda(k_c)$ is the linear growth rate and the exact form of the nonlinear term f_j is defined by the normal form of the symmetry under study (Crawford, 1991). The parameters for the amplitude equations can be obtained by various techniques, e.g. multiscale expansion (see De Wit (1993)) or center manifold reduction (see Callahan and Knobloch (1999)). The stability of different symmetries can be studied by linear analysis of the amplitude equation system. One must, however, remember that the nonlinear analysis is qualitative in nature and the approximation works only for relatively low nonlinearities in the vicinity of the onset. Linear and nonlinear analysis of the BVAM model will be presented in Chapter 4.

3.1.3 Degeneracies

There are two kinds of degeneracies related to the Turing instability. The first one is the orientational degeneracy, which is due to isotropy, i.e., there are many wave vectors $\vec{k}$ having the same wave number $k = |\vec{k}|$. The linear stability analysis predicts only the wavenumber associated with the instability and does not give any information concerning the direction of the unstable wave vectors. It can be thought that the two-dimensional wave vectors corresponding to the wavenumber k_c are vectors pointing from the center of a circle with radius k_c to the circumference. This follows that the number of linear combinations of unstable wave vectors (Eq. (3.11)) is infinite. Which of these wavevectors is chosen depends on the phase induced by the random initial conditions and the boundary conditions.

The second degeneracy is due to the unstable sideband. The width of the unstable wave window associated with a Turing instability (see Fig. 3.1) allows more than one unstable mode, i.e., there are some $k_i \neq k_c$ with $\mathrm{Re}\{\lambda(k_i)\} > 0$. The unstable modes that differ from k_c, the highest point of the dispersion relation curve are said to form the sideband. The sideband widens (the peak of the dispersion curve rises) with the distance to onset $a_c - a$ as the bifurcation parameter a is varied. The linear analysis does not tell, which of these unstable modes will

grow, although it is typically safe to assume that the modes dominating the pattern selection are not far away from k_c. In large systems there may be numerous unstable modes forming a quasi-continuous ensemble of modes affecting greatly the dynamics of the model. This effect can be studied analytically by introducing spatial dependence to the amplitudes W_j of the modes. The resulting envelope equations for amplitudes are of the form (cf. Eq. (3.12))

$$\frac{dW_j}{dt} = \lambda_c W_j + f_j(W_1, \ldots, W_n) + \xi_0^2 \ ^2 W_j, \tag{3.13}$$

where $\xi_0 \sim k_c^{-1}$ is the coherence length and is a spatial operator describing the modulation of the pattern by the modes on the sideband. Envelope equation formalism allows general studies of the mechanisms of pattern formation (Manneville, 1990; Newell et al., 1993; Cross and Hohenberg, 1993).

A third factor affecting the pattern selection is not exactly due to intrinsic degeneracy, but due to the numerical methods that are often employed while studying pattern formation in Turing systems. In a discrete three-dimensional system the wave numbers are defined by

$$|\vec{k}| = 2\pi \sqrt{\left(\frac{n_x}{L_x}\right)^2 + \left(\frac{n_y}{L_y}\right)^2 + \left(\frac{n_z}{L_z}\right)^2}, \tag{3.14}$$

where L_x, L_y and L_z denote the system size in respective directions, and n_x, n_y and n_z the respective wave number indices. For a one-dimensional system we would have $n_y = n_z = 0$ and for a two-dimensional system $n_z = 0$. Since the system is discrete it is not precisely isotropic and thus the underlying lattice may bias the pattern selection. For example, simulations carried out in a square lattice might favor the formation of patterns with square symmetry. In addition, the number of modes on the sideband is reduced by the discrete lattice, which does not allow all the modes of the continuous spectrum. The degeneracy due to numerical methods is usually not a big problem and it can be attenuated by choosing small enough discretization length, using alternative lattice symmetries or non-lattice based methods (Madzvamuse, 2000).

3.2 Examples of Turing models

There is a variety of Turing models with different reaction kinetics and their own specific characteristics. In the studies presented in this thesis we use the BVAM model. To get a general idea of Turing models, we will next review three other well-known models, namely the Brusselator, Gray-Scott and Lengyel-Epstein models. Other important Turing models that are not introduced here include the Gierer-Meindhardt model (Gierer and Meinhardt, 1972; Bose and

Chaudhuri, 1997), Selkov model (Hunding, 1980; Hunding and Engelhardt, 1995; Vance and Ross, 1999), and Schnackenberg model (Dufiet and Boissonade, 1991, 1992).

3.2.1 The Brusselator model

The Brusselator model was developed by Ilya Prigogine among others in the late 1960s at the University of Brussels and it is one of the simplest chemical models exhibiting Turing instability (Nicolis and Prigogine, 1977). In the case of the Brusselator model the phenomenological chemical reaction formulae are given by

$$A \rightarrow U \tag{3.15}$$
$$B + U \rightarrow V \tag{3.16}$$
$$2U + V \rightarrow 3U \tag{3.17}$$
$$U \rightarrow E, \tag{3.18}$$

where U and V are spatially and temporally varying chemical concentrations, whereas the concentrations of the chemicals A, B and E are kept constant. The law of mass action states that the rate of a reaction is proportional to the product of the concentrations of the reactants (Murray, 1989). Thus based on Eqs. (3.15)-(3.18) one can find out the changes in the concentrations of chemicals U and V. The first reaction (Eq. (3.15)) results in contributions $+A$ and 0 to concentrations U and V, respectively. Similarly, the second reaction (Eq. (3.16)) results in contributions $-BU$ and $+BU$ to U and V. In addition, Eq. (3.16) yields the contributions $-2U^2V + 3U^2V$ and $-U^2V$ and Eq. (3.16) gives $-U$ and 0. By summarizing the above considerations, the Brusselator model can be written as (Nicolis and Prigogine, 1977)

$$\begin{aligned} U_t &= D_U\nabla^2 U + A - (B+1)U + U^2V \\ V_t &= D_V\nabla^2 V + BU - U^2V, \end{aligned} \tag{3.19}$$

where A denotes the value of the source term and B is the bifurcation parameter setting the distance to the onset of instability. The chemical U is the activator and V is the inhibitor such that always $D_V > D_U$. The stationary state of the model is given by $(U_0, V_0) = (A, B/A)$. The threshold for the Turing instability is $B_c^T = [1+A\sqrt{D_U/D_V}]^2$, whereas a Hopf instability occurs for $B > B_c^H = 1+A^2$. The wave number corresponding to the most unstable Turing mode is given by $k_c^2 = A/\sqrt{D_U D_V}$. The full nonlinear analysis of the Brusselator model has been carried out by De Wit (1993) (see also Walgraef (1997)).

In the absence of the Turing instability the Brusselator model shows temporal behavior similar to the Belousov-Zhabotinsky reaction. This was an important

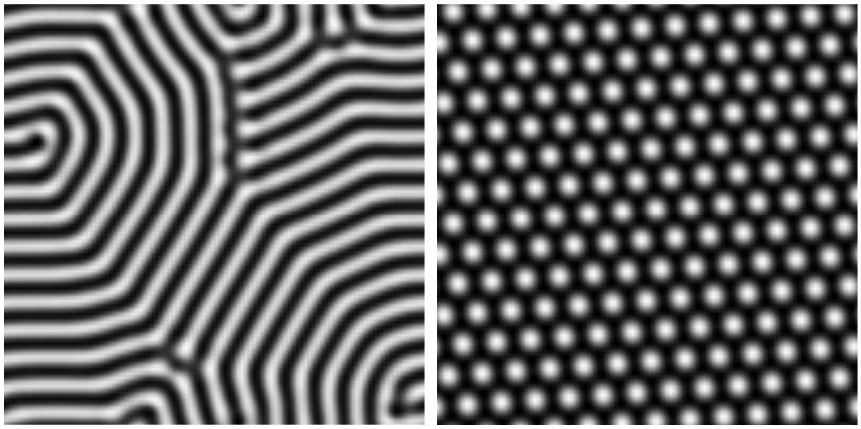

Figure 3.2: Stripes and spots in a two-dimensional numerical simulation of the Brusselator model (Eq. (3.19)). Parameters were $A = 4.5$, $D_V/D_U = 8$ resulting in $B_c^T = 6.71$. Thus $B = 7.5$ for stripes and $B = 6.75$ for spots. The initial configuration was random perturbations around the uniform stationary state.

finding in 1968, since it implied that there is a connection between the mechanism of these two chemical instabilities, which subsequently facilitated the first experimental observation of a Turing pattern in a chemical reactor over 20 years later (see Section 3.3). Figure 3.2 shows two typical patterns generated by the Brusselator model from a random initial configuration.

The Brusselator model has been studied extensively both theoretically and numerically. Some of the first studies were concerned with theoretical concepts such as symmetry-breaking and bifurcations (Nicolis and Prigogine, 1977; Walgraef et al., 1980). Later studies employed the computational approach and addressed the problem of pattern selection as a function of system parameters in two-dimensional (Verdasca et al., 1992; Borckmans et al., 1992) and three-dimensional systems (De Wit et al., 1992, 1997). Most recently temporal dynamics of the Brusselator model, i.e., Turing-Hopf interaction (De Wit et al., 1996) and spatial resonances (Yang et al., 2002) have been studied. Callahan (2003) has studied Hopf bifurcations in three-dimensional systems using amplitude equations.

3.2.2 Gray-Scott model[1]

The Gray-Scott model was developed by P. Gray and S. K. Scott at the University of Leeds in the 1980s. The model was of great importance since it describes an experimentally observable auto-catalytic reaction in an isothermal continuous-

[1] This subsection is based on Leppänen et al. (2002).

flow stirred tank reactor (CSTR). The Gray-Scott model could be said to be the simplest chemical model, which shows oscillations in the same type of reactor, where the first experimental evidence of Turing patterns was found later (see Section 3.3). The Gray-Scott model corresponds to two irreversible chemical reactions Gray and Scott (1983, 1984, 1985)

$$\begin{aligned} \mathrm{U} + 2\mathrm{V} &\rightarrow_1 3\mathrm{V} \\ \mathrm{V} &\rightarrow_K \mathrm{P}, \end{aligned} \tag{3.20}$$

where U and V are the reacting chemicals, and 1 and K define the reaction rates. Due to the irreversible nature of the reactions, the chemical P is an inert product and thus two equations of motion are sufficient for describing the system. In addition, it is assumed that the chemical U is in contact with a reservoir and the chemical V is removed from the system at constant rate F. Using the law of mass action one obtains in dimensionless units

$$\begin{aligned} \partial_t U &= D_U \nabla^2 U - UV^2 + F(1-U) \\ \partial_t V &= D_V \nabla^2 V + UV^2 - (F+K)V, \end{aligned} \tag{3.21}$$

where F and K are reaction parameters and D_U and D_V are the diffusion coefficients of the inhibitor and activator chemicals, respectively. The stationary states of the model are defined as

$$U_0 = \frac{1 \pm \sqrt{1 - 4(F+K)^2/F}}{2}, V_0 = \frac{F(1-U_0)}{F+K}, \tag{3.22}$$

where by fixing $U_0 = 1$ one obtains the trivial stationary state $(U_0, V_0) = (1, 0)$. In chemical experiments of the Gray-Scott reaction the difference of diffusion coefficient has not been established and thus Turing patterns have been observed only in numerical simulations of the Gray-Scott reaction.

The Gray-Scott model has been studied analytically and numerically in two dimensions by John Pearson, who mapped the phase diagram of the system in terms of the two rate constants F and K Pearson (1993). The model exhibits a very rich behavior ranging from time-independent stationary solutions to oscillatory and time-dependent phase turbulent behavior. The dynamics of self-replicating spotty patterns have been studied in the Gray-Scott model (Reynolds et al., 1994, 1997). Furthermore, Vastano et al. (1987) have shown that a one-dimensional Gray-Scott system can exhibit stable stationary patterns as a response to finite amplitude perturbations even when the two diffusion constants are equal. These patterns cannot, however, arise spontaneously due to the Turing instability. Nonlinear analysis of the model has been carried out by Ipsen et al. (2000).

We have studied numerically the pattern formation in the Gray-Scott model in the presence of chemical sources (Leppänen et al., 2002). In this study we added

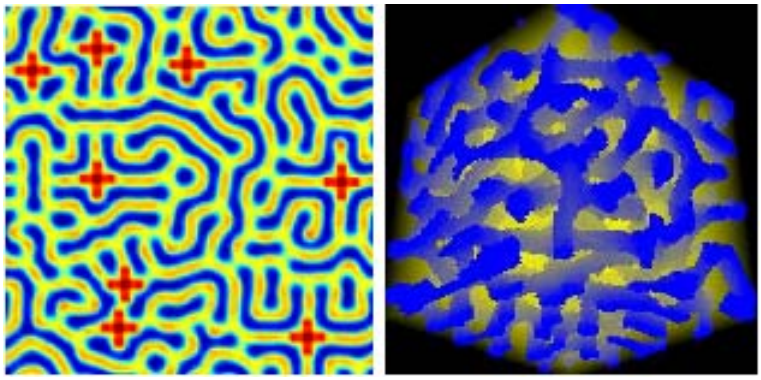

Figure 3.3: Left: Pattern obtained in a two-dimensional 120×120 lattice with periodic boundary conditions using the Gray-Scott model in the presence of eight sources of morphogen V with parameters $F = 0.065$, $K = 0.0625$, $D_u = 0.125$, $D_v = 0.05$. The sources appear as "cross-like" patterns. Right: Pattern obtained using the three-dimensional Gray-Scott model with four sources of V, $F = 0.045$, $K = 0.065$, $D_u = 0.125$, $D_v = 0.05$.

a small number of sources of the chemical V to random positions and otherwise initialized the system randomly. The sources were set to feed the chemical V at a constant rate ($+0.01$). The motivation for adding the sources was to investigate the formation of connections between the sources, thus attempting to mimic the formation of synaptic contacts between neurons. We used the Gray-Scott model since it produces labyrinthine or tubular patterns more easily than the other reaction-diffusion models. Here the chemical sources can be thought of as representing neurons whereas the growing dendrites must connect them. Our numerical simulations show that the Gray-Scott model produces robust tubular patterns in both two and three dimensions (see Fig. 3.3).

The concepts of positional information and chemical signaling present in the Turing systems could play an important role as an inductive mechanism for neuronal connections by acting as chemical pathways for other biochemical factors. We are particularly interested in pursuing this idea, but it should be remembered that any specific mechanism for Turing patterning in a real tissue has to happen in three dimensions. Neurons do not always form connections with the nearest neurons, but also with neurons far away, behind other cells. We believe that Turing patterns could explain this spatial selectivity by providing the signaling pathways for neurotrophic factors. Simple diffusion of these substances cannot explain the complexity of neuronal patterning.

Previous studies have often employed highly elaborate random walk models, which include neurophysiological data (Segev and Ben-Jacob, 2000; van Ooyen,

2001). Our idea is that a chemical Turing pattern forms a pre-pattern for the randomly growing dendrites describing the neurotrophic factors (see Leppänen (2001) for details). By using Hoshen-Kopelman algorithm (Hoshen and Kopelman, 1976) it was confirmed that also in the three-dimensional structure the sources are connected by the chemical dendrites. Currently, it is unclear whether Turing systems could act as an inductive signaling mechanism for neural patterning, but we have shown that simple reaction and diffusion can generate connected patterns spontaneously, which makes the idea plausible.

3.2.3 The Lengyel-Epstein model

After the first experimental observation of a Turing pattern in 1989 in the chlorite-iodide-malonic acid (CIMA) reaction (see Section 3.3), Istvan Lengyel, Gyula Rabai and Irving Epstein proposed a model for the oscillations in the chlorine dioxide-iodine-malonic acid (CDIMA) reaction after the initial chlorite and iodide ions were consumed (Lengyel et al., 1990a,b). The reactions that CDIMA reaction are given by

$$\begin{aligned} MA + I_2 &\rightarrow IMA + I^- + H^+ \\ ClO_2 + I^- &\rightarrow ClO_2^- + \frac{1}{2} I_2 \\ ClO_2^- + 4I^- + 4H^+ &\rightarrow 2I_2 + Cl^- + 2H_2O \end{aligned} \tag{3.23}$$

Later Lengyel and Epstein showed that in the presence of starch and the subsequent complexation of the iodide ions, i.e., $S + I_2 + I^- \quad SI_3^-$ the pattern formation phenomena in the CIMA system could be approximated by only two kinetic equations corresponding to the dominant components, that is iodide ions (I^-, the activator) and chlorite ions (ClO_2^-, the inhibitor). The Lengyel-Epstein model is given by the normalized equations of motion (Lengyel and Epstein, 1991, 1992; Lengyel et al., 1992)

$$\begin{aligned} U_t &= \frac{1}{\sigma}(\nabla^2 U + a - U - 4\frac{UV}{1+U^2}) \\ V_t &= d\nabla^2 V + b(U - \frac{UV}{1+U^2}), \end{aligned} \tag{3.24}$$

where a, b, d and σ are parameters, which can be adjusted based on experimental reaction rates. U is the normalized iodide ion concentration and V is the normalized chlorite ion concentration. The stationary state is given by $(U_0, V_0) = (a/5, 1 + a^2/25)$. For more details on the analytical treatment of the Lengyel-Epstein model we refer the reader to Rudovics et al. (1999) (see also Callahan and Knobloch (1999)). For a more profound review of chemical modeling and the

experimental background of the Lengyel-Epstein model the reader is referred to Lengyel and Epstein (1995) and Lengyel et al. (1996).

The Lengyel-Epstein model is important in the sense that it captures the essential features of the CIMA reaction, where experimental Turing structures are observed. The Lengyel-Epstein model has been studied by employing theoretical approaches and numerical simulations (e.g. Rovinsky and Menzinger (1992) or Jensen et al. (1993)). In these studies chemical experiments and numerical simulations have also often been used in parallel. For more details of the experimental studies the reader is guided to Section 3.3.2.

3.3 Experimental Turing structures

The confirmation of Turing's ideas turned out to be challenging since the existence of chemical spatial patterns as predicted by his mathematical formulations could not be confirmed experimentally. The first unambiguous experimental observation of a stationary Turing pattern was preceded by theoretical studies Vastano et al. (1987, 1988) and the practical development of a new kind of continuously stirred tank reactors (see e.g. (Lengyel and Epstein, 1995)). It was not until 1989, when Patrick De Kepper's group observed a stationary spotty pattern in a chemical system involving the reactions of chlorite ions, iodide ions and malonic acid (CIMA reaction) (Castets et al., 1990).

3.3.1 CIMA reaction

It was mostly the required difference in the diffusion rates of the chemical substances that delayed the first experimental observation of chemical Turing patterns. In aqueous solutions all small molecules have approximately same diffusion coefficients ($\propto 10^{-5}\ cm^2/s$) and thus the realization of an activator-inhibitor mechanism with a difference in diffusion coefficients seemed extremely difficult. The Gray-Scott reaction showing oscillations in a continuously fed reactor (see Sec. 3.2.2) was an important intermediate step in the experimental observation of a real chemical Turing pattern.

There are numerous chemical systems exhibiting oscillations (see e.g. Epstein and Showalter (1996)) and De Kepper et al. happened to be studying oscillations in the chlorine dioxide-iodine-malonic acid (CDIMA) reaction in 1989 (see Eq. (3.23) above). In order to increase the color contrast of their results, they introduced starch to the slab of gel, where fresh reagents were fed from the side. This addition resulted in the reversible complexation of the iodine ions by large starch molecules thus reducing their diffusion rate in the gel significantly. Due to the difference in the diffusion coefficients and other appropriate conditions Turing patterns were observed with respect to the iodine and chlorite ion concentrations (Castets et al., 1990). The results by Castets et al. (1990) are shown in Figure 3.4.

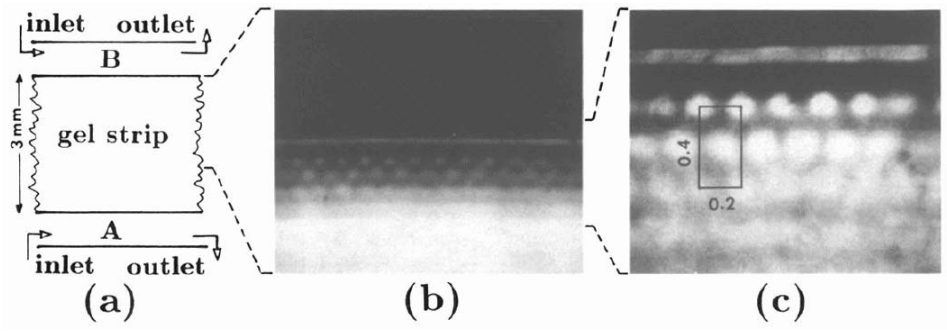

Figure 3.4: a) The reactor is fed from the both sides with fresh reagents, b) Turing pattern in the gel, c) Enlarged pattern (scales in mm). The figure is reproduced from Castets et al. (1990).

There were many facts that made the chemical pattern that Castets et al. (1990) observed unambiguously a Turing pattern. Firstly, the symmetry-breaking took place to a direction not imposed by feeding gradients. Secondly, the gel dampened out any convective motion of molecules and thus the pattern was known to arise solely due to reaction and diffusion. Thirdly, the pattern remained stationary as long as the system parameters stayed the same, i.e., a constant feeding rate of reagents was provided ($\sim$ 20 hours). Fourthly, the characteristic wavelength of the pattern $\lambda \approx 0.2\ mm$ was different from any external length scale and thus it seemed to be intrinsic. In addition, similar patterns were observed repeatedly for the same feed concentrations in the reactor and the pattern could be destroyed by a perturbation (e.g. intense light) only momentarily (Boissonade et al., 1995).

A year later Qi Ouyang and Harry L. Swinney observed also stripes in the CIMA reaction by using different feeding rates for the reagents and in addition showed using a new kind of visualization technique that experimental Turing patterns can be grown also over large domains (Ouyang and Swinney, 1991). The complexation step in the CIMA reaction scheme has received a lot of attention due to its importance in chemical Turing pattern formation. Agladze et al. (1992) have shown that Turing patterns can exist even in gel-free media, i.e., the use of gel for slowing down the starch complex is not necessary for obtaining Turing patterns. On the other hand, Noszticzius et al. (1992) have found out that the complexation agent affects exclusively on the iodide-complex formation, which results in unequal diffusion coefficients, and it has no effect on the dynamics of the CIMA reaction. It should be noted that both Turing and Hopf instabilities can be observed in the CIMA reaction by varying the concentration of the color indicator in the reactor (Perraud et al., 1992; De Wit, 1999).

3.3.2 Recent experimental work

After the first experimental observation of a Turing pattern, the studies of the pattern formation in CIMA reaction have been extended to the spatio-temporal regime, where the system exhibits for example traveling waves and chemical flip-flops (Perraud et al., 1992; Dewel et al., 1995; Rudovics et al., 1996). Some studies have also addressed the problem of dimensionality and studied the pattern formation on different depths in the reactor gel (Ouyang et al., 1992) or in ramped systems (Dulos et al., 1996) (see also Section 5.5). Most of the experimental research, however, has been carried out with the photosensitive CDIMA reaction in the presence of forcing.

The effect of temporally (Horváth et al., 1999) and spatially periodic illumination (Dolnik et al., 2001b,a; Berenstein et al., 2003) on the pattern formation in the CDIMA reaction has been investigated. Also the problem of spatially correlated forcing of varying intensity has been addressed in the context of both spotty (Sanz-Anchelergues et al., 2001) and stripe (Pena et al., 2003) patterns. In addition, Petrov et al. (1997) have interestingly observed a transition from a spiral pattern to a Turing-like labyrinthine pattern as a result of temporally periodic forcing of the Belousov-Zhabotinsky reaction. For a more extensive review of relevant experimental work the reader is referred to other sources (Kapral and Showalter, 1995; De Kepper et al., 2000; Borckmans et al., 2002).

3.4 Summary

This chapter focused on specific kind of reaction-diffusion systems, namely Turing systems, and introduced the typically employed research methodology. Turing instability, which results in chemical concentration patterns with a characteristic wave length, was illustrated with help of hungry cannibals and biking missionaries on an island. More formal introduction of the topic was done by discussing the strengths of linear stability analysis and pattern selection theory. Degeneracies that affect the pattern formation are the orientational degeneracy and sideband degeneracy. Also the discretization due to numerical simulations causes some degeneracy. The characteristics of the Brusselator, Gray-Scott, and Lengyel-Epstein models were discussed in order to illustrate the general features of Turing models. The chapter was concluded with an introduction to experimental research and the CIMA reaction, which is the most important chemical system exhibiting a Turing instability.

Chapter 4

Mathematical analysis of Barrio-Varea-Aragon-Maini model

The study of any given Turing model starts with a mathematical analysis of the model. As outlined in the previous chapter, one first carries out a linear stability analysis, which is typically followed by a nonlinear bifurcation analysis. The linear analysis is an effective tool for finding the suitable parameter values for the Turing instability and analyzing the onset of the instability. The nonlinear analysis, on the other hand, is required for analyzing the stability of different symmetries or *morphologies* in the system.

In this chapter we will carry out the full mathematical analysis of the Barrio-Varea-Aragon-Maini (BVAM) model introduced by Barrio et al. (1999). In the first section, we will derive and normalize the model. Then, we will analyze the model by using a linear approximation and discuss our findings. Since the presentation of the nonlinear bifurcation analysis has often been somewhat vague in the literature, this chapter is concluded with a meticulous report of the nonlinear analysis of the BVAM model. The algebra involved in the nonlinear analysis is rather lengthy and thus some details are left to the appendices A.1 and A.2.

4.1 Derivation of BVAM model

The BVAM model is a formal or phenomenological Turing model and it is not based on any real chemical reactions. The model was introduced by Barrio et al. (1999) as a general model, which could be applied for imitating the pattern formation on the skins of various fish species. The general form of a Turing model describing the spatial and temporal variations of the concentrations U and V is

defined as (see Sec. 2.3)

$$\begin{aligned} U_t &= D_U \nabla^2 U + f(U,V) \\ V_t &= D_V \nabla^2 V + g(U,V). \end{aligned} \tag{4.1}$$

The BVAM model is obtained by Taylor expanding the reaction kinetics (the nonlinear functions f and g in Eq. (4.1)) around a stationary solution of the system denoted by (U_c, V_c). If the terms of the fourth and higher order are neglected, the reaction-diffusion equations can be written as (Barrio et al., 1999)

$$\begin{aligned} u_t &= D\delta\nabla^2 u + \alpha u(1 - r_1 v^2) + v(1 - r_2 u) \\ v_t &= \delta\nabla^2 v + v(\beta + \alpha r_1 u v) + u(\gamma + r_2 v), \end{aligned} \tag{4.2}$$

where $u = U - U_c$ and $v = V - V_c$, which makes $(u_0, v_0) = (0, 0)$ a stationary state. The terms uv and uv^2 describe the nonlinear inhibition of the activator chemical u by the inhibitor chemical v. The nonlinear term $u^2 v$ cannot be included since it would describe reverse behavior. The parameters r_1, r_2, α, β and γ are scalars defining the reaction kinetics. The diffusion coefficients are written in terms of a scaling factor δ and ratio of the diffusion coefficients D. Since the chemical u is the activator and the chemical v is the inhibitor, we must always have $D < 1$ for Turing instability to occur.

To reduce the number of parameters and simplify the analysis we carry out non-dimensionalization (Murray, 1989) of the Eq. (4.2) by rescaling the concentrations, and the time and length scales with constants such that $u = U\overline{u}$, $v = V\overline{v}$, $t = T\overline{t}$, and $x = L\overline{x}$. The substitution of these new notations into Eq. (4.2) yields

$$\begin{aligned} \frac{U}{T}\overline{u}_t &= \frac{\delta D U}{L^2}\nabla^2\overline{u} + \alpha U\overline{u} - \alpha r_1 U V^2 \overline{u}\overline{v}^2 + V\overline{v} - r_2 U V \overline{u}\overline{v} \\ \frac{V}{T}\overline{v}_t &= \frac{\delta V}{L^2}\nabla^2\overline{v} + \beta V\overline{v} + \alpha r_1 U V^2 \overline{u}\overline{v}^2 + \gamma U\overline{u} + r_2 U V \overline{u}\overline{v}, \end{aligned} \tag{4.3}$$

which can be written as

$$\begin{aligned} \overline{u}_t &= \frac{\delta D T}{L^2}\nabla^2\overline{u} + \alpha T\overline{u} - \alpha r_1 V^2 T \overline{u}\overline{v}^2 + \frac{TV}{U}\overline{v} - r_2 V T \overline{u}\overline{v} \\ \overline{v}_t &= \frac{\delta T}{L^2}\nabla^2\overline{v} + \beta T\overline{v} + \alpha r_1 U V T \overline{u}\overline{v}^2 + \gamma\frac{UT}{V}\overline{u} + r_2 U T \overline{u}\overline{v}. \end{aligned} \tag{4.4}$$

This system can be further simplified by fixing $T = L^2/\delta$, $U = V = 1/\sqrt{r_1}$ and introducing the new parameters

$$a = 1/\alpha, \tag{4.5}$$

$$b = \beta/\alpha, \tag{4.6}$$

$$h = \gamma/\alpha, \tag{4.7}$$

$$C = r_2/(\alpha\sqrt{r_1}), \tag{4.8}$$

$$\eta = L^2\alpha/\delta. \tag{4.9}$$

This yields the dimensionless model

$$\begin{aligned} \overline{u}_t &= D\nabla^2\overline{u} + \eta(\overline{u} + a\overline{v} - C\overline{uv} - \overline{uv}^2) \\ \overline{v}_t &= \nabla^2\overline{v} + \eta(b\overline{v} + h\overline{u} + C\overline{uv} + \overline{uv}^2), \end{aligned} \tag{4.10}$$

where the time-space relation is given by $T = L^2/\delta$ (we have used $L = 1$ for simplicity). The term C adjusts the relative strength of the quadratic and cubic nonlinearities favoring spotty and striped patterns, respectively. From now on we shall omit the overlines for simplicity.

One can easily see that the normalized system of Eq. (4.10) has a unique stationary state at $(u_0^0, v_0^0) = (0, 0)$ for $h = -1$. For $h \neq -1$ the system has also two other stationary states defined by $f(u_0, v_0) = g(u_0, v_0) = 0$ given by

$$v_0^j = \frac{-C + (-1)^j + \sqrt{C^2 - 4(h - bK)}}{2} \tag{4.11}$$

and

$$u_0^j = -v_0^j/K, \tag{4.12}$$

where $K = \frac{1+h}{a+b}$ and $j = 1, 2$. The behavior of the system around these stationary states can be studied by using linear analysis, which we will carry out next.

4.2 Linear stability analysis

As discussed in Section 3.1.1, linear analysis is an effective method for studying the response of the a Turing system to perturbations in the vicinity of a stationary state. Next we apply linear analysis in the context of the BVAM model to determine the appropriate parameter values resulting in the Turing instability and to study the stability of the stationary states.

Substituting a trial solution into a Turing model (Eq. (4.1)) one obtains the eigenvalue problem (see Sec. 3.1.1)

$$|\mathbf{A} - \mathbf{D}k^2 - \lambda\mathbf{I}| = 0, \tag{4.13}$$

where the matrix $\mathbf{A}$ is defined by the partial derivatives of the reaction kinetics evaluated at the stationary state (u_0, v_0), the stability of which one is to study. For the BVAM model the matrix $\mathbf{D}$ is defined by $D_{11} = D$, $D_{22} = 1$, $D_{12} = D_{21} = 0$, $\mathbf{I}$ is the identity matrix and $\mathbf{A}$ is given by

$$\mathbf{A} = \begin{pmatrix} f_u & f_v \\ g_u & g_v \end{pmatrix}_{(u_0, v_0)} = \eta \begin{pmatrix} 1 - v_0^2 - Cv_0 & -2u_0v_0 + a - Cu_0 \\ v_0^2 + h + Cv_0 & b + 2u_0v_0 + Cu_0 \end{pmatrix}, \tag{4.14}$$

where u_0 and v_0 are defined by $(u_0, v_0) = (0, 0)$ or Eqs. (4.11) and (4.12). The determinant defined by Eq. (4.13) gives the characteristic equation (cf. Eq. (3.6)).

Around the primary stationary solution $(u_0, v_0) = (0, 0)$, which is the only solution if $h = -1$, the characteristic equation for the BVAM model reads as

$$\begin{aligned} \lambda^2 + \left[(1+D)k^2 - \eta(1+b)\right]\lambda + \\ Dk^4 - \eta k^2(Db+1) + \eta^2(b-ah) &= 0. \end{aligned} \tag{4.15}$$

The dispersion relations $\lambda(k)$ for the BVAM model are defined by the eigenvalues defined by the characteristic equation. Now $\mathrm{Re}\{\lambda(k)\}$, which predicts the unstable wave modes can be obtained from Eq. (4.15). One can estimate the most unstable wave number and the critical value of the bifurcation parameter by noticing that at the onset of the instability $\lambda(k_c) = 0$. Thus the constant term in Eq. (4.15) must be zero at k_c. In the case of the BVAM model this condition is a second order equation on k_c^2, i.e.,

$$Dk_c^4 - k_c^2\eta(Db+1) + \eta^2(b-ah) = 0. \tag{4.16}$$

and as a result the most unstable wave number is given by $k_c^2 = \eta(Db+1)/(2D)$. The critical bifurcation parameter value, which corresponds to the onset of the instability is defined by Eq. (4.16). In the BVAM model a is the bifurcation parameter adjusting the distance to the onset of the instability. The discriminant of Eq. (4.16) equals zero for a_c and an instability takes place for $a < a_c = (Db-1)^2/(4D)$. To confirm that this instability is, indeed, a Turing instability more conditions must be satisfied.

The Turing space is the region of the parameter space in which the conditions for the Turing instability are met. In the case of the BVAM model with $h = -1$ the conditions for the Turing space (see Eqs. (3.9)) yield the constraints $-b < a < a_c$ and $-1/D < b < -1$. Based on this one can sketch the phase space diagram for the BVAM model and it is presented in Fig. 4.1. From the stability diagram one can notice that the number of the parameter combinations exhibiting Turing instability, i.e., the size of the Turing space (shaded region) is relatively small. Other regions in the diagram correspond to a stable stationary state, oscillatory Hopf instability (see Sec. 3.1.1) and complex spatio-temporal instabilities.

Based on the stability diagram one can choose parameters that result in the Turing instability and plot the corresponding dispersion relations. In the studies presented in this thesis we have mostly used two sets of parameters defined by $D = 0.516$, $a = 1.112$, $b = -1.01$ and $\eta = 0.450$ for $k_c = 0.46$ ($a_c = 1.121$) and $D = 0.122$, $a = 2.513$, $b = -1.005$ and $\eta = 0.199$ for $k_c = 0.85$ ($a_c = 2.583$). The dispersion relation is obtained by solving Eq. (4.15) with respect to λ and plotting the real part of the solution as a function of the wave number k. The dispersion relations corresponding to the onset of the instability (at $a = a_c$) and the above parameter sets resulting in the instability around the stationary state $(u_0, v_0) = (0, 0)$ are shown in Fig. 4.2. As discussed in Sec. 3.1.1, the

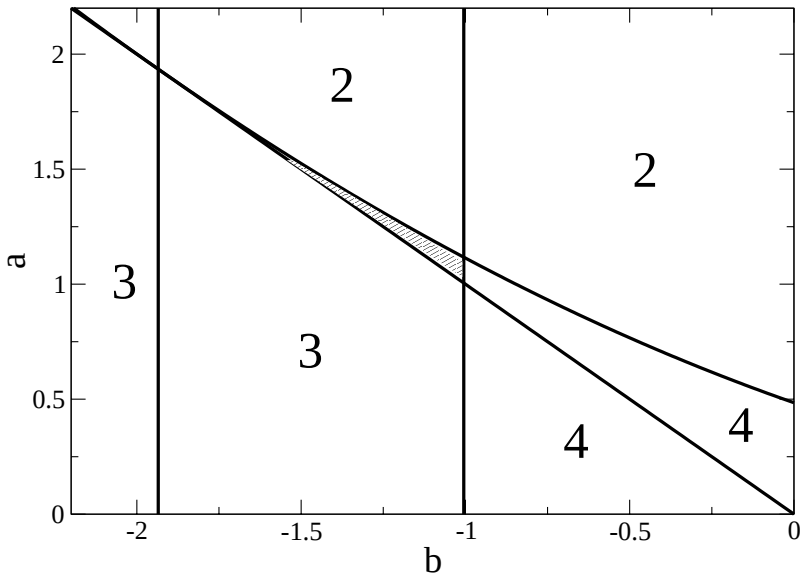

Figure 4.1: The phase space diagram of the BVAM model (Eq. (4.10)). The Turing space (shaded region) is bounded by lines $b = -1/D$, $b = -1$, $b = -a$ and the curve $a = (Db-1)^2/(4D)$. For the plot the ratio of the diffusion coefficients was fixed to $D = 0.516$. The other regions: stable state (2), other complex spatio-temporal instabilities (3) and Hopf instability (4).

wave numbers k with $\mathrm{Re}\{\lambda(k)\} < 0$ are stable, whereas the wave numbers with $\mathrm{Re}\{\lambda(k)\} > 0$ correspond to the growing unstable modes.

The real part of the dispersion relation depicts the growth rate of the unstable wave modes. The imaginary part, on the other hand, describes the frequency of the temporal behavior. The real and imaginary parts of the eigenvalues corresponding to the stationary state $(u_0, v_0) = (0, 0)$ are shown in Figure 4.3 for two sets of parameters corresponding to a Turing bifurcation (a k_c unstable) and a Hopf bifurcation (k_0 unstable) in a monostable system. The parameters used in Fig. 4.3 were the ones derived above for the Turing instability around $(0, 0)$ with critical wave number $k_c = 0.85$ and the same except $b = -0.8$ for the Hopf instability.

From Fig. 4.3 one can observe that a Turing bifurcation corresponds to the case, where there is some k_i such that $\mathrm{Re}\{\lambda(k_i)\} > 0$ and $\mathrm{Im}\{\lambda(k_i)\} = 0$. On the other hand, a Hopf bifurcation corresponds to the situation, where a pair

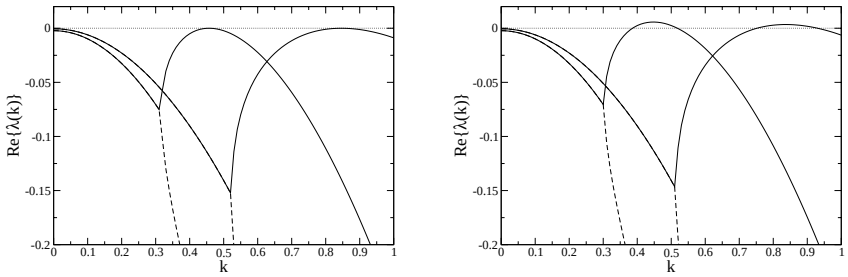

Figure 4.2: The real part of the dispersion relation $\lambda(k)$ corresponding to two different parameter sets with $k_c = 0.46$ and $k_c = 0.85$, respectively. Left: At the onset of instability $a = a_c$ and there are no unstable modes. Right: For $a < a_c$ there is a finite wave length Turing instability corresponding to the wave numbers k for which $\mathrm{Re}\{\lambda(k)\} > 0$.

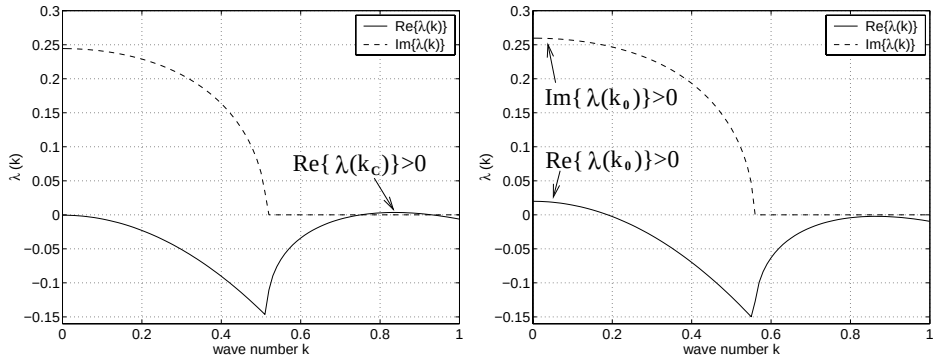

Figure 4.3: The largest eigenvalue of the linearized system corresponding to a Turing (left) and Hopf bifurcation (right). The real and imaginary parts of the eigenvalues correspond to solid and dashed lines, respectively.

of imaginary eigenvalues crosses the imaginary axis, i.e., there is some k_i with $\mathrm{Re}\{\lambda(k_i)\} > 0$ and $\mathrm{Im}\{\lambda(k_i)\} \neq 0$. The parameters of the BVAM model can also be adjusted such that $k_c = 0$ for Turing instability (corresponding to a characteristic length of system-size) or so that there is a combined Turing-Hopf bifurcation from one stationary state. Interaction between Turing and Hopf instabilities will be studied numerically in Sec. 5.6, in particular in the presence of multiple stationary states. The critical parameter value for the Hopf bifurcation in the BVAM model with $h = -1$ is $b_c^H = -1$ and for the Turing bifurcation $b_c^T = (1 - \sqrt{4Da})/D$.

From the results of the linear analysis we can identify the parameter domain,

which results in the Turing instability and approximate the characteristic wave lengths of the patterns. The BVAM model has been devised in such a way that by adjusting the parameter C one can favor either stripes or spots (Barrio et al., 1999). Striped pattern and hexagonally arranged spots are typical for reaction-diffusion systems in two dimensions (Boissonade et al., 1995). To find out which morphology will be chosen in the BVAM system, one needs the nonlinear bifurcation analysis and it is the subject of next section.

4.3 Nonlinear bifurcation analysis[1]

Bifurcation theory is a mathematical tool that is generally used for studying the dynamics of nonlinear systems (Crawford, 1991; Newell et al., 1993; Manneville, 1990). The result of bifurcation analysis or weakly nonlinear analysis describes the changes taking place in the dynamics of the system as an outcome of changing the system parameters. In the case of Turing systems the bifurcation analysis answers the question concerning the changes in the stability of different morphologies as the bifurcation parameter is varied. Bifurcation analysis has previously been applied in the cases of the Brusselator model (Walgraef, 1997) and the Lengyel-Epstein model (Rovinsky and Menzinger, 1992). The published analyses and text books often omit many mathematical details, which are necessary for fully understanding the technique. Here special attention will be paid to the details.

As discussed in Sec. 3.1.2, the idea of bifurcation analysis is to find a presentation for the concentration field $\vec{w} = (u, v)$ in terms of the active Fourier modes, i.e.,

$$\vec{w} = \vec{w}_0 \sum_{\vec{k}_j} (W_j e^{i\vec{k}_j \cdot \vec{r}} + W_j^* e^{-i\vec{k}_j \cdot \vec{r}}), \tag{4.17}$$

where W_j and W_j^* are the amplitudes corresponding to the modes $+\vec{k}_j$ and $-\vec{k}_j$. By using bifurcation analysis one obtains the amplitude equations that describe the time evolution of the amplitudes W_j. The BVAM model of Eq. (4.10) has been devised in such a way that one can adjust the relative strength of the quadratic and cubic nonlinearities. Thus the parameter C dominates the instability by imposing symmetry requirements to the system and governs the pattern selection. This parameter controls the morphology selection between linear (stripe) and radial (spot) structures instead of the bifurcation parameter. Thus some additional algebraic manipulations must be carried out at the end of the bifurcation analysis. In this way the BVAM model is different from the Brusselator (Nicolis and Prigogine, 1977) and the Lengyel-Epstein (Lengyel and Epstein, 1992) models, which

[1] Most of the work presented in this section has been published in Leppänen (2004).

have only one nonlinear term and the morphology of the resulting pattern is determined by the value of the bifurcation parameter, i. e., the distance to the onset of instability.

The main idea of the bifurcation analysis is to get insight into the the chemical system by mapping the chemical dynamics to the center manifold, where the reduced dynamics captured by the amplitude equations can be studied more easily. Here I have divided the bifurcation analysis for pedagogical reasons into three parts: derivation of the normal form for the amplitude equations in a particular symmetry, determining the parameters of the amplitude equations, and finally analyzing the stability of different morphologies by applying linear analysis to the system of amplitude equations. These three phases will be the respective topics of the following subsections.

4.3.1 Derivation of amplitude equations

The time variation of the amplitudes W_j of the unstable modes $\vec{k}_j$ ($j = 1, \ldots, n$) can be described with a system of n coupled amplitude equations. Amplitude equations have a linear part, which describes the linear growth predicted by the positive eigenvalue of the linearized system defined by Eq. (4.15) and a nonlinear part describing the nonlinear coupling of the unstable modes. Thus in the most general form of an amplitude equation is given by

$$\frac{dW_j}{dt} = \lambda_c W_j + f_j(W_1, \ldots, W_n). \tag{4.18}$$

The eigenvalue may be approximated from Eq. (4.15) in the vicinity of the onset by a linear approximation given by

$$\lambda_c = \left.\frac{d\,\lambda}{da}\right|_{a=a_c} (a - a_c) = \frac{\eta^2(\eta - 2R)}{(\eta(1+b) - 2R)(\eta - R)}(a - a_c), \tag{4.19}$$

where $R = \eta(Db+1)/2$ with notations of the BVAM model (Eq. (4.10)). The exact form of the term $f(W_1, \ldots, W_n)$ in Eq. (4.18) depends on the symmetry under study and the generic form of it for a particular symmetry can be constructed by geometrical arguments. Typically one approximates the dynamics of the system by writing down the amplitude equations only for the most unstable mode k_c. The effects of the unstable modes on the sideband can be evaluated by using envelope amplitude equations as discussed in Sec. 3.1.3.

In two dimensions, reaction-diffusion systems typically exhibit either stripes or hexagonally arranged spots (see e.g. Fig. 3.2). If one considers the chemical concentration wave forming a pattern of spots, the maxima of the inhibitor (or minima of the activator) correspond to a triangular lattice. On the other hand, the minima (or maxima) form the dual lattice of the triangular lattice, namely the

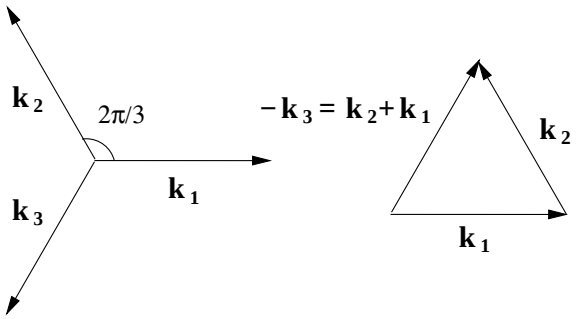

Figure 4.4: The vectors describing the set of nearest neighbors in two-dimensional hexagonal lattice are not linearly independent and thus there are resonant modes.

hexagonal lattice. In three dimensions there are various possibilities for arrangement: One can study the simple cubic lattice (SC), body-centered cubic lattice (BCC) or face-centered cubic lattice (FCC) (for illustrations of the lattice structures see e.g. Ashcroft and Mermin (1976)). Callahan and Knobloch have been among the first to address the problem of bifurcations in three-dimensional Turing systems (Callahan and Knobloch, 1996, 1997, 1999, 2001; Callahan, 2004). In the following we will derive the general form for the amplitude equations of the two-dimensional hexagonal lattice and three-dimensional SC-, FCC-, and BCC-lattices.

Two-dimensional hexagonal lattice

As for symmetries, one must differentiate between the real (concentration) space and the Fourier (wave vector) space. The symmetries of the concentration patterns correspond to the symmetries of the reciprocal lattice in the wave vector space (see e.g. Ashcroft and Mermin (1976)). For example, the reciprocal lattice of the two-dimensional hexagonal lattice is another hexagonal lattice translated by $\pi/6$ with respect to the original lattice. The vectors forming a two-dimensional hexagonal lattice can be chosen to be $\vec{k}_1 = k_c(1,0)$, $\vec{k}_2 = k_c(-1/2, \sqrt{3}/2)$ and $\vec{k}_3 = k_c(-1/2, -\sqrt{3}/2)$ with $|\vec{k}_{1,2,3}| = k_c$. Since for example $-\vec{k}_1 - \vec{k}_2 = \vec{k}_3$, we can say that a hexagonal lattice exhibits *resonant modes*. Resonant modes are described by a quadratic coupling term and must be taken into account, while deriving the amplitude equations. In a simple square lattice there would not be any resonant modes, since any subset of the vectors capturing the symmetry operations does not sum up to another vector. The vectors constructing a hexagonal lattice and the idea of resonant modes is illustrated in Fig. 4.4.

The set of wave vectors presented in Fig. 4.4 defines the wave vectors that form the chemical concentration pattern. The alignment of the triad is irrelevant

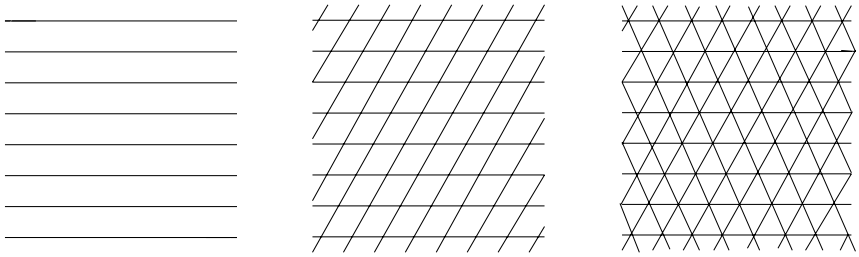

Figure 4.5: The symmetries enabled by the three basis vectors of a hexagonal lattice are striped patterns, rhombic arrays and hexagonal lattices.

to the pattern selection problem since one is only interested in the symmetry. One unstable wave vector ($\vec{k}_2 = \vec{k}_3 = 0$) would result in an essentially one-dimensional period pattern, namely rolls or stripes. Two unstable wave vectors ($\vec{k}_3 = 0$) would be able to form a rhombic pattern, whereas three non-zero wave vectors are sufficient to describe the two-dimensional hexagonal lattice. The two-dimensional symmetries that are observed in a variety of physical systems (Cross and Hohenberg, 1993; Walgraef, 1997) can be generated from the basis vectors of a hexagonal lattice of Fig. 4.4 as illustrated in Fig. 4.5.

Since there are resonant modes, one would expect that there is a quadratic coupling term in the amplitude equations. In a hexagonal lattice the negative sum of two modes may contribute to a third mode and thus there must be a term of the form $W_{j+1,j+2}e^{ik_j\cdot r} = (-W^*_{j+1}e^{i(-k_{j+1})\cdot r})(-W^*_{j+2}e^{i(-k_{j+2})\cdot r})$ in $f_j(W_1, W_2, W_3)$ of Eq. (4.18) ($j = 1, 2, 3\ (mod\ 3)$). The combinations of wave vectors that sum up to $\vec{k}_j$ in addition to the resonant pair are $\vec{k}_j - \vec{k}_j + \vec{k}_j$, $\vec{k}_{j+1} - \vec{k}_{j+1} + \vec{k}_j$, and $\vec{k}_{j+2} - \vec{k}_{j+2} + \vec{k}_j$. The respective contributions to $f_j(W_1, W_2, W_3)$ are $-|W_j|^2 W_j$, $-|W_{j+1}|^2 W_j$ and $-|W_{j+2}|^2 W_j$. We assume that the saturation occurs at the third order and thus take into account only the sums of maximum three vectors. Now the full amplitude equation for the two-dimensional hexagonal lattice can be written as

$$\frac{dW_j}{dt} = \lambda_c W_j + \Gamma W^*_{j+1} W^*_{j+2} - g[|W_j|^2 + \kappa(|W_{j+1}|^2 + |W_{j+2}|^2)]W_j, \quad (4.20)$$

where $j = 1, 2, 3\ (mod\ 3)$, the λ_c is given by Eq. (4.19) and the coefficients Γ, g and κ can be presented in terms of the parameters of the original reaction-diffusion system (Eq. (4.10)). The coefficients are obtained via complicated mathematical techniques, which will be discussed next.

Three-dimensional SC-lattice

The reciprocal lattice of a three-dimensional simple cubic (SC) lattice is of the same symmetry. The three wave vectors describing the symmetry of the SC-

lattice can be chosen to be $\vec{k}_1 = k_c(1,0,0)$, $\vec{k}_2 = k_c(0,1,0)$ and $\vec{k}_3 = k_c(0,0,1)$ with $|\vec{k}_{1,2,3}| = k_c$. Now the vectors are linearly independent and thus there are no resonant modes. The combinations of wave vectors that sum up to $\vec{k}_j$ are $\vec{k}_j - \vec{k}_j + \vec{k}_j$, $\vec{k}_{j+1} - \vec{k}_{j+1} + \vec{k}_j$, and $\vec{k}_{j+2} - \vec{k}_{j+2} + \vec{k}_j$. By considering the contributions of these combinations as in the case of the two-dimensional hexagonal lattice, one can deduce the form of the amplitude equations to be

$$\frac{dW_j}{dt} = \lambda_c W_j - g[|W_j|^2 + \kappa(|W_{j+1}|^2 + |W_{j+2}|^2)]W_j, \tag{4.21}$$

where $j = 1,2,3$ $(mod\ 3)$, again λ_c is given by Eq. (4.19), and g and κ are parameter dependent coefficients.

Three-dimensional FCC-lattice

The three-dimensional face-centered cubic (FCC) lattice is not as simple. The reciprocal lattice of the FCC-lattice is the body-centered cubic (BCC) lattice described by a set of four vectors given by

$$\begin{aligned} \vec{k}_1 &= k_c(1,1,1)/\sqrt{3}, \quad \vec{k}_2 = k_c(1,1,-1)/\sqrt{3}, \\ \vec{k}_3 &= k_c(1,-1,1)/\sqrt{3}, \quad \vec{k}_4 = k_c(1,-1,-1)/\sqrt{3} \end{aligned}$$

with $|\vec{k}_{1,2,3,4}| = k_c$. These are not linearly independent and there are resonant modes since e.g. $\vec{k}_2 + \vec{k}_3 - \vec{k}_4 = \vec{k}_1$. Thus there is a cubic resonant coupling term and in addition there are the other nonlinear terms that can be derived as in the previous cases. The amplitude equations are given by

$$\frac{dW_j}{dt} = \lambda_c W_j - \Gamma W_{j+1} W_{j+2} W_{j+3}^* - g[|W_j|^2 + \kappa(|W_{j+1}|^2 + |W_{j+2}|^2 + |W_{j+3}|^2)]W_j, \tag{4.22}$$

where $j = 1,2,3,4$ $(mod\ 4)$, again λ_c is given by Eq. (4.19), and Γ, g and κ are parameter dependent coefficients.

Three-dimensional BCC-lattice

The reciprocal lattice of the three-dimensional BCC-lattice is the FCC-lattice with the corresponding symmetry group defined by six vectors

$$\begin{aligned} \vec{k}_1 &= k_c(1,1,0)/\sqrt{2}, \quad \vec{k}_2 = k_c(0,1,1)/\sqrt{2}, \quad \vec{k}_3 = k_c(1,0,1)/\sqrt{2}, \\ \vec{k}_4 &= k_c(1,-1,0)/\sqrt{2}, \quad \vec{k}_5 = k_c(0,1,-1)/\sqrt{2}, \quad \vec{k}_6 = k_c(1,0,-1)/\sqrt{2} \end{aligned}$$

with $|\vec{k}_{1,2,3,4,5,6}| = k_c$. Again the vectors are not linearly independent, but there is both quadratic and cubic resonant coupling. For example the resonant modes of k_1 are defined by $\vec{k}_2 + \vec{k}_6 = \vec{k}_1$, $\vec{k}_3 + \vec{k}_5 = \vec{k}_1$, $\vec{k}_2 + \vec{k}_4 + \vec{k}_5 = \vec{k}_1$, and $\vec{k}_3 - \vec{k}_4 + \vec{k}_6 =$

$\vec{k}_1$. Notice that since k_j and k_{j+3} are in the same plane, their coupling must be treated separately. Combining the contributions of resonant and other modes to the amplitude W_j yields the following general form

$$\begin{aligned}\frac{dW_j}{dt} &= \lambda_c W_j + \Upsilon(W_{j+1}W_{j+5} + W_{j+2}W_{j+4}) + \\ &\quad \Gamma(W_{j+1}W_{j+3}W_{j+4} + W_{j+2}W^*_{j+3}W_{j+5}) - g|W_j|^2 - \\ &\quad g[\chi|W_{j+3}|^2 + \kappa(|W_{j+1}|^2 + |W_{j+2}|^2 + |W_{j+4}|^2 + |W_{j+5}|^2)]W_j,\end{aligned} \tag{4.23}$$

where $j = 1, 2, 3, 4, 5, 6$ $(mod\ 6)$, again λ_c is given by Eq. (4.19), and Υ, Γ, g, χ and κ are coefficients dependent on the model parameters.

4.3.2 Center manifold reduction

There are various methods for determining the parameters for the above amplitude equations. Often one uses the multiscale expansion, where the bifurcation parameter and the chemical concentrations are expanded around a small parameter (e.g. $a - a_c = \epsilon a_1 + \epsilon^2 a_2 + \ldots$). The coefficients for the amplitude equations are obtained based on the solvability conditions of the resulting linear differential equations at different degrees of ϵ (see e.g. Newell et al. (1993) or Walgraef (1997)). In our studies we have employed another method called the center manifold reduction.

The amplitude equations derived in the previous section can be expressed in terms of the reaction-diffusion parameters (Eq. 4.10) by devising a mapping from the concentration space to the center manifold of the wave vector space. The mapping from the concentration space (Eq. (4.10)) to a high-dimensional equivariant amplitude space (Eq. (4.18)) can be found by employing *center manifold theorem* (see Sec. 2.1.3). The center manifold reduction confines the nonlinear effects in the system to the center manifold and thus one can obtain good approximations for the stability of different structures. In the following, we will sketch the general procedure for mapping the dynamics of a Turing model to the center manifold (see Callahan and Knobloch (1999)).

In general, we can write the component h of a Turing system with n chemical species ($h \in \{1, ..., n\}$) as

$$\begin{aligned}\frac{dX^h}{dt} &= D^h\,\nabla^2 X^h + \sum_{i=1}^{n} A^{h,i}X^i + \sum_{i=1}^{n}\sum_{j=1}^{n} A^{h,ij}X^iX^j + \\ &\quad \sum_{i=1}^{n}\sum_{j=1}^{n}\sum_{k=1}^{n} A^{h,ijk}X^iX^jX^k + \ldots\end{aligned} \tag{4.24}$$

where $X^h = X^h(\vec{x}, t)$ is the spatially varying concentration of one chemical species such that $X^h = 0$ in the uniform stationary state. The tensors $A^{h,i}$, $A^{h,ij}$ and $A^{h,ijk}$ define the parameters for the component h and are symmetric with respect to permutations of the indices. In a discrete system we can write the concentration field as

$$X^h(\vec{x}, t) = \sum_{l \in L} \tilde{X}_l^h(t) e^{i\vec{k}_l \cdot \vec{x}}, \tag{4.25}$$

where L is the set of all lattice points. From now on we write species indices (e.g. h) as superscripts and lattice point indices (e.g. l) as subscripts. Substituting Eq. (4.25) into Eq. (4.24) yields

$$\frac{dX_l^h}{dt} = -D^h |\vec{k}_l|^2 X_l^h + A^{h,i} X_l^i + A^{h,ij} \sum_{l_1+l_2=l} X_{l_1}^i X_{l_2}^j + A^{h,ijk} \sum_{l_1+l_2+l_3=l} X_{l_1}^i X_{l_2}^j X_{l_3}^k, \tag{4.26}$$

where we have used the Einstein summation convention for the indices i, j and k, and included only the terms up to cubic order. The linear part the previous equation defines the unstable modes (see Sec. 4.2) and the linear matrix can be written in the form

$$J_l^{h,i} = -D^h k_l^2 \delta^{h,i} + A^{h,i}, \tag{4.27}$$

where it is assumed that there is no cross-diffusion ($\delta^{h,i} = 1$ only when $h = i$). For each lattice point we may now choose a matrix

$$S_l = \begin{pmatrix} \alpha_l^{11} & \dots & \alpha_l^{1n} \\ \vdots & \ddots & \vdots \\ \alpha_l^{n1} & \dots & \alpha_l^{nn} \end{pmatrix}, \tag{4.28}$$

with $\det(S_l) = 1$. In addition, we require that it has an inverse matrix $S_l^{-1} = \{\beta_l^{ij}\}$ such that

$$S_l^{-1}\, J_l S_l = \begin{pmatrix} \lambda_l^1 & & \\ & \ddots & \\ & & \lambda_l^n \end{pmatrix}. \tag{4.29}$$

The conditions for this similarity transformation are widely known (Kreyszig, 1993). Now we can map the original concentrations to a new basis defined by $X_l = S_l W_l$. In this new basis Eq. (4.26) reads as

$$\begin{aligned} \frac{dW_l^g}{dt} \;=\; & \lambda_l^g W_l^g + \beta_l^{gh} A^{h,ij} \sum_{l_1+l_2=l} \alpha_{l_1}^{ii'} W_{l_1}^{i'} \alpha_{l_2}^{jj'} W_{l_2}^{j'} + \\ & \beta_l^{gh} A^{h,ijk} \sum_{l_1+l_2+l_3=l} \alpha_{l_1}^{ii'} W_{l_1}^{i'} \alpha_{l_2}^{jj'} W_{l_2}^{j'} \alpha_{l_3}^{kk'} W_{l_3}^{k'}, \end{aligned} \tag{4.30}$$

where the coefficient of the linear term is defined by Eq. (4.19). The center manifold and coefficients of the amplitude equations can be found at the onset ($a = a_c$)

by noticing that the contributions to the modes on the stable manifold come from nonlinear coupling of the unstable modes. By using this condition one can derive the amplitude equations for the modes on the center manifold (see Callahan and Knobloch (1999) for details). Further simplification of Eq. (4.30) for a critical wave vector m at the onset ($\lambda_l^g = 0$) yields

$$\begin{aligned}\frac{dW_m^1}{dt} &= \beta^{1h} A^{h,ij} \alpha^{i1} \alpha^{j1} \sum_{m_1+m_2=m} W_{m_1}^1 W_{m_2}^1 + \\ &\sum_{m_1+m_2+m_3=m} F(m_2+m_3) W_{m_1}^1 W_{m_2}^1 W_{m_3}^1, \end{aligned} \tag{4.31}$$

where

$$F(l) \equiv -2\,\beta^{1h} A^{h,ij} \alpha^{i1} (J_l^{-1})^{ja} A^{a,bc} \alpha^{b1} \alpha^{c1} + \beta^{1h} A^{h,ijk} \alpha^{i1} \alpha^{j1} \alpha^{k1}. \tag{4.32}$$

One should notice that the coefficient $F(l)$ depends on the argument l only through the square of its length (see Eq. 4.27)). Thus the previous treatment is general and not specific to any particular symmetry. For the calculation of the coefficients of the amplitude equations (e.g. Eq. (4.20)) using the center manifold reduction, we follow a computational procedure that has been used earlier by Callahan and Knobloch (1999). The derivation of the coefficients is based on finding the number and type of resonant modes that contribute to the amplitude of a particular mode as shown in Eq. (4.31). Because of symmetry, the coefficients of all the amplitude equations (all j) in a particular amplitude system (cf. Eq. (4.20)) are the same. The coefficients for the two-dimensional hexagonal lattice and three-dimensional SC-, FCC-, and BCC-lattices are derived in the Appendix A.1.

4.3.3 Stability analysis of amplitude equation systems

After we have obtained the system of coupled amplitude equations written with respect to the parameters of the original reaction-diffusion equations, we may employ linear analysis to study its stability around the stationary states corresponding to different symmetries. First one has to determine the stationary states W_c of the amplitude system and then one can linearize the system (as in Eq. (3.5)) and construct the corresponding Jacobian matrix $\mathbf{A}$ with the elements defined as

$$\{\mathbf{A}\}_{ij} = \left| \frac{df_i}{d|W_j|} \right|_{(W_1^c, W_2^c, W_3^c)}, \tag{4.33}$$

where f_i denotes the right-hand side of the corresponding amplitude equation i and the derivative is evaluated at the stationary state $W_c = (W_1^c, W_2^c, W_3^c)$. Based on this one can plot the bifurcation diagram, i.e., the eigenvalues of the linearized system $dW/dt = \mathbf{A}W$ as a function of the parameter C of the BVAM model

(Eq. (4.10)), which contributes to the morphology selection in the BVAM model. In the following, we will present the bifurcation diagrams and the results concerning the stability of different symmetries for the two-dimensional hexagonal lattices and three-dimensional SC-, FCC-, and BCC-lattices. Most of the details are left to Appendix A.2.

Two-dimensional hexagonal lattice

In the case of two-dimensional patterns we are interested in the stability of stripes ($W_c = (W_1^c, 0, 0)^T$), rhombic patterns ($W_c = (W_1^c, W_2^c, 0)^T$) with $W_1^c = W_2^c$), and hexagonally arranged spots ($W_c = (W_1^c, W_2^c, W_3^c)^T$ with $W_1^c = W_2^c = W_3^c$ or $W_1^c = W_2^c \neq W_3^c$). The system of amplitude equations for a two-dimensional hexagonal lattice can be written based on Eq. (4.20).

By carrying out the linearization of the complete amplitude system around the stationary states corresponding to different symmetries one can study the stability of patterns by calculating the eigenvalues of the linear system (see Appendix A.2 for details). For stripes the eigenvalues of the linearized matrix are given by $\mu_1^s = -2\lambda_c$, $\mu_2^s = -\Gamma\sqrt{\lambda_c/g} + \lambda_c(1-\kappa)$ and $\mu_3^s = \Gamma\sqrt{\lambda_c/g} + \lambda_c(1-\kappa)$. Noticing that $\mu_1^s < 0$ and $\mu_3^s > \mu_2$ follows that the stability of stripes is determined solely by the sign of μ_3^s. The stripes are unstable for $\mu_3^s > 0$ and stable for $\mu_3^s < 0$. The rhombic patterns and mixed modes are always unstable.

In the case of the hexagonally arranged spots the eigenvalues of the system are given as $\mu_{1,2}^h = \lambda_c - |W_\pm^c|(\Gamma + 3g|W_\pm^c|)$ and $\mu_3^h = \lambda_c + |W_\pm^c|(2\Gamma - 3g(2\kappa + 1)|W_\pm^c|)$, where $|W_\pm^c|$ is defined by Eq. (A.15). Since there are two stationary states corresponding to the hexagonal symmetry one must analyze the stability of them both. For stability all the eigenvalues must be negative, i.e., $\mu_{1,2}^h < 0$ and $\mu_3^h < 0$. After writing the eigenvalues in terms of the original parameters of the BVAM model by using Eqs. (4.19), (A.1), (A.2), (A.3) one can plot the eigenvalues as a function of the nonlinear coefficient C, which is known to adjust the competition between stripes and spots (Barrio et al., 1999). The result is shown in Fig. 4.3.3, from where one can determine the parameter regimes for which a given pattern is stable, i.e., $\mu(C) < 0$.

Fig. 4.3.3 implies that the hexagonal branch corresponding to W_c^+ is always unstable. Thus there is only one isotropic hexagonal solution to the equations that is stable within certain parameter regime. While using the parameters of mode $k_c = 0.85$ (see Sec. 3.1.1) the analysis predicts that stripes are stable for $C < 0.161$. On the other hand, the other hexagonal branch is predicted to be stable for $0.084 < C < 0.611$. The most important information obtained from Fig. 4.3.3 is the region of bistability, which is predicted to be between $0.084 < C < 0.161$. For the parameters of the mode $k_c = 0.45$ the stripes are predicted to be stable for $C < 0.139$ and the hexagons for $0.073 < C < 0.529$. This yields the bistable regime $0.073 < C < 0.139$. Since the bifurcation analysis

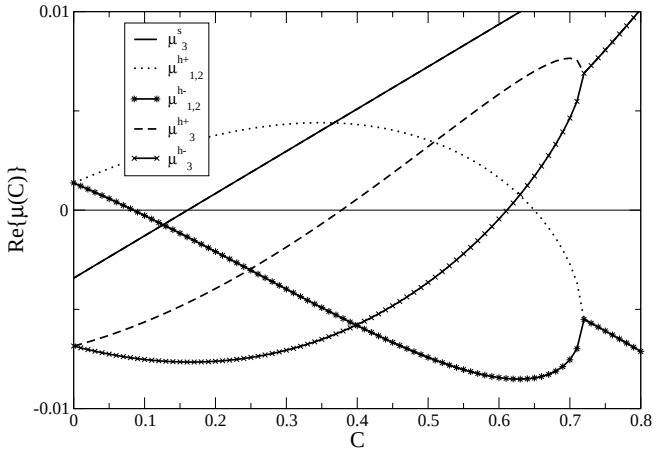

Figure 4.6: The real part of the eigenvalues $\mu(C)$ of the linearized amplitude system of the two-dimensional hexagonal symmetry as a function of the parameter C for the parameters corresponding to the wave mode $k_c = 0.85$. Eigenvalue μ_3^s determines the stability of the stripes, $\mu_{1,2}^{h+}$ and μ_3^{h+} determine the stability of one hexagonal branch, and $\mu_{1,2}^{h-}$ and μ_3^{h-} determine the stability of the other hexagonal branch. The morphology is stable if the corresponding $\mu(C) < 0$.

is based on weakly nonlinear approximation of the dynamics, it can be expected that it fails, when a strong nonlinear action is present. For example, based on the result of the numerical simulation presented in the next chapter one notices that the hexagonal spot pattern exists for $C = 1.57$. However, the bifurcation analysis predicts that hexagons are unstable for all $C > 0.611$. This discrepancy is due to the approximations made in the bifurcation analysis, the predictions of which are more precise for weak nonlinearities.

Three-dimensional SC-lattice

In the case of three-dimensional simple cubic lattice there are three possibilities for the structure. One may get planar structures ($W_c = (W_1^c, 0, 0)^T$), cylindrical structures ($W_c = (W_1^c, W_2^c, 0)^T$) or spherical droplet structures ($W_c = (W_1^c, W_2^c, W_3^c)^T$). The amplitude equations of the three-dimensional SC-lattice are defined by Eq. (4.21).

The linearization of the amplitude equation system corresponding to the SC-lattice is explained in detail in the Appendix A.2. For the planar lamellae the eigenvalues of the linearized matrix are given by $\mu_1^{Lam} = -2\lambda_c$ and $\mu_{2,3}^{Lam} =$

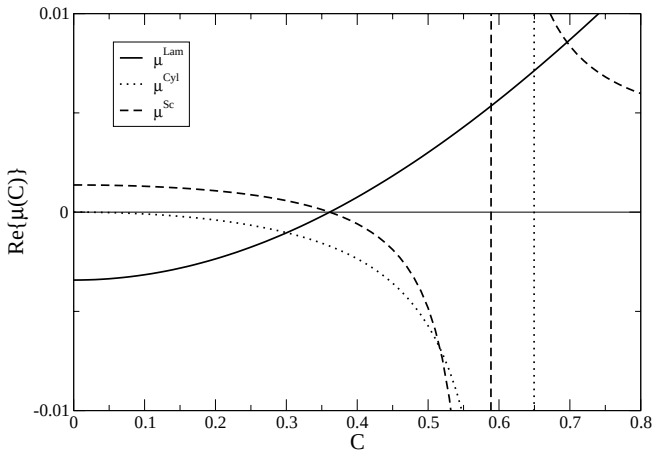

Figure 4.7: The real part of the eigenvalues $\mu(C)$ of the linearized amplitude system of the three-dimensional SC-lattice as a function of the parameter C for the parameters corresponding to the wave mode $k_c = 0.85$. Eigenvalue μ^{Lam} determines the stability of the planar lamellae, μ^{Cyl} determines the stability of cylindrical structures, and μ^{Sc} determines the stability of the spherical droplets organized in a SC-lattice. The morphology is stable if $\mu(C) < 0$.

$\lambda_c(1-\kappa)$. Noticing that $\mu_1^{Lam} < 0$ follows that the stability of the planar structures is determined by $\mu_{2,3}^{Lam}$. By repeating the same treatment for the cylindrical structures we find that the real part of the dominant eigenvalue is $\mu_{2,3}^{Cyl} = \lambda_c - 3g|W_c|^2$. For the SC-droplets the stability determining eigenvalue is given by $\mu_{2,3}^{Sc} = \lambda_c - 3g|W_c|^2$. The real parts of the eigenvalues are presented in Fig. 4.3.3.

Based on Fig. 4.3.3 it can be reasoned that the bifurcation analysis does not predict a bistability between planes and spherical shapes in three dimensions, but the stability of those structures is exclusive for $k_c = 0.85$. The planes are predicted to be stable for $C < 0.361$ and the spherical shapes stable for $0.361 < C < 0.589$. The square packed cylinders, however, are predicted to be stable for all $C < 0.650$. For $k_c = 0.45$ the planar lamellae is stable for $C < 0.241$, the spherical droplets for $0.241 < C < 0.375$, and the cylinders for all $C < 0.402$. It should again be noticed that the bifurcation analysis fails for strong nonlinear interaction, i.e., high values of parameter C.

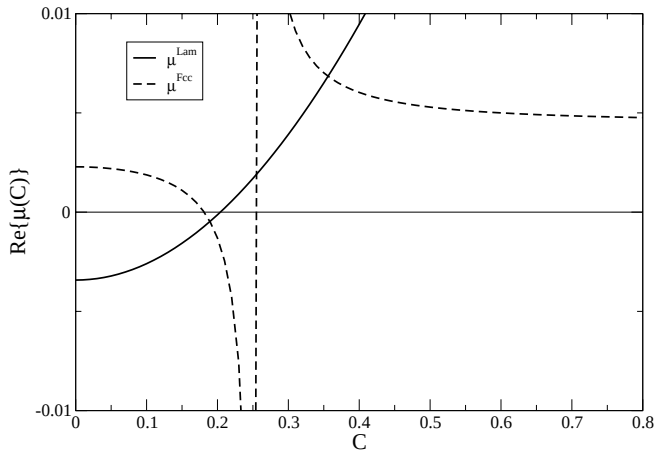

Figure 4.8: The real part of the eigenvalues $\mu(C)$ of the linearized amplitude system of the three-dimensional FCC-lattice as a function of the parameter C for the parameters corresponding to the wave mode $k_c = 0.85$. Eigenvalue μ^{Lam} determines the stability of the planar lamellae and μ^{Fcc} determines the stability of the spherical droplets organized in a FCC-lattice. The morphology is stable if $\mu(C) < 0$.

Three-dimensional FCC-lattice

In the case of three-dimensional FCC-lattice there are numerous possibilities for the structure (Callahan and Knobloch, 1999). Here we analyze only the stability of lamellar structures ($W_c = (W_1^c, 0, 0, 0)^T$) and spherical droplets organized in a FCC-lattice ($W_c = (W_1^c, W_2^c, W_3^c, W_4^c)^T$). The amplitude equations of the three-dimensional FCC-lattice are defined by Eq. (4.22).

For the planar lamellae the eigenvalues the linearized matrix (Appendix A.2) are given by $\mu_1^{Lam} = -2\lambda_c$ and $\mu_{2,3,4}^{Lam} = \lambda_c(1-\kappa)$. Noticing that $\mu_1^{Lam} < 0$ follows that the stability of the planar structures is again determined by $\mu_{2,3,4}^{Lam}$. For the FCC-droplets, on the other hand, the stability determining eigenvalue is given by $\mu_{2,3,4}^{Sc} = \lambda_c - 3(\Gamma + g(K+3))W_c^2$. The real parts of these eigenvalues are presented in Fig. 4.3.3 as a function of C.

From Fig. 4.3.3 one can see that there is a bistability between planes and FCC-droplet structures for $0.181 < C < 0.204$ with $k_c = 0.85$. The planes are predicted to be stable for $C < 0.204$ and the spherical shapes stable for $0.181 < C < 0.255$. Again it can be observed that the bifurcation analysis fails already at a reasonable low nonlinear interaction predicting that the spherical structures become unstable at $C = 0.255$. On the other hand, for the parameters

of the wave mode $k_c = 0.45$, the planes are stable for $C < 0.133$ and the FCC-droplets for $0.118 < C < 0.164$ yielding in a bistability for $0.118 < C < 0.133$. Most probably, there is a multistability of various FCC-symmetries. The stability of the other possible structures in FCC-lattice has been studied by Callahan and Knobloch (1999).

Three-dimensional BCC-lattice

As in a three-dimensional FCC-lattice, also in BCC-lattice there are numerous possibilities for the structure (Callahan and Knobloch, 1999). Here we analyze only the stability of lamellar structures ($W_c = (W_1^c, 0, 0, 0, 0, 0)^T$) and spherical droplets organized in a FCC-lattice ($W_c = (W_1^c, W_2^c, W_3^c, W_4^c, W_5^c, W_6^c)^T$). The amplitude equations of a three-dimensional BCC-lattice are defined by Eq. (4.23).

For the planar lamellae the eigenvalues of the linearized matrix (see Appendix A.2 for details) are given by $\mu_1^{Lam} = -2\lambda_c$, $\mu_{2,3,5,6}^{Lam} = \lambda_c(1-\kappa)$, and $\mu_4^{Lam} = \lambda_c(1-\chi)$. Noticing that $\mu_1^{Lam} < 0$ follows that the stability of the planar structures is determined by the greater eigenvalue from $\mu_{2,3,5,6}^{Lam}$ and μ_4^{Lam}. For the FCC-droplets, on the other hand, the stability determining eigenvalue cannot be solved in closed form, but only numerically due to the complexity of the stability matrix. The real parts of these eigenvalues are presented in Fig. 4.3.3 as a function of C.

From Fig. 4.3.3 one can see that there is a bistability between planes and BCC-droplet structures for $0.264 < C < 0.355$ for $k_c = 0.85$. The planes are predicted to be stable for $C < 0.355$ and the spherical shapes stable for $0.264 < C < 0.450$. Again it can be observed that the bifurcation analysis fails already at a reasonable low nonlinear interaction predicting that the spherical structures become unstable at $C = 0.450$. The analysis of FCC-symmetries required further approximations due to the discontinuity of $F(l)$ (Eq. 4.32) at the onset ($l = 1$) to obtain the center manifold dynamics (see (Callahan and Knobloch, 1999)) and our *ad hoc* approximation failed in the case of $k_c = 0.45$. The stability of structures other than planes or droplets in the BCC-lattice remains to be studied in the context of the BVAM model.

4.4 Summary

In this chapter it was shown how the BVAM model can be derived and studied from basic principles. Based on the mathematical analysis one can select parameters for the numerical simulations and obtain predictions for the results numerical simulations (see Chapter 5). In this way the mathematical analysis provides some additional confirmation to the results of the numerical simulations. Based on the analysis of the linearized system one could predict the parameters corresponding to an onset of Turing instability and determine the characteristic length of

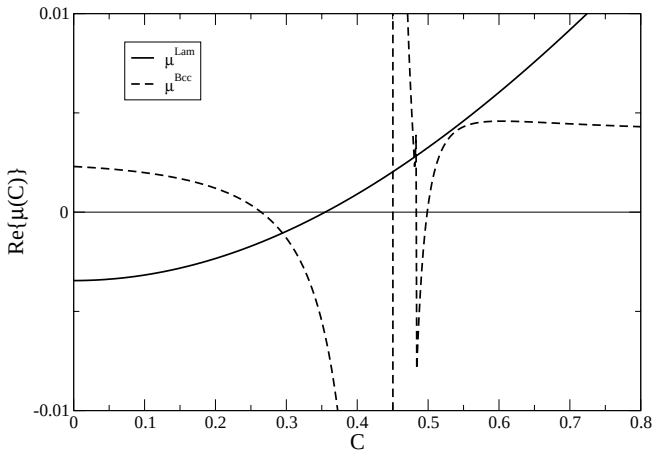

Figure 4.9: The real part of the eigenvalues $\mu(C)$ of the linearized amplitude system of the three-dimensional BCC-lattice as a function of the parameter C for the parameters corresponding to the wave mode $k_c = 0.85$. Eigenvalue μ^{Lam} determines the stability of the planar lamellae and μ^{Bcc} determines the stability of the spherical droplets organized in a BCC-lattice. The morphology is stable if $\mu(C) < 0$.

the resulting concentration patterns by finding the unstable wave modes. In order to understand the pattern selection in the system one had to carry out a mathematically demanding nonlinear bifurcation analysis. The bifurcation analysis enabled the study of the full system dynamics by studying only the reduced dynamics at the center manifold described by the amplitude equations. As a result the bifurcation analysis gave the parameter regimes that correspond to particular symmetries in two- and three-dimensional systems.

Chapter 5

Numerical studies of Barrio-Varea-Aragon-Maini model

In general, reaction-diffusion equations describe the time evolution of the spatial distribution of chemical concentrations. The non-uniform stationary states of a model that corresponds to spatial patterns cannot be found analytically, but iterative computer simulations are required. If the model parameters are chosen appropriately the computer simulations give rise to beautiful two-dimensional patterns and three-dimensional structures. The analytical studies presented in the previous chapter confirm the results of the numerical simulations. The characteristic length of the patterns is predicted by linear analysis, and based on bifurcation analysis one knows, which structures could appear while using a certain parameter set. The analytical methods are not sufficient to fully understand the system, which is a reason for using computer simulations.

This chapter begins with an introduction to the computational method, which is followed by the results of the numerical simulations using the BVAM model introduced and analyzed in the previous chapter. First, I will present typical results of simulations carried out in two- and three-dimensional domains and study the effect of parameters and initial conditions on the resulting patterns. Then I will present results concerning the robustness of Turing patterns against Gaussian noise. After that we will discuss morphological transitions due to changing parameters, and pattern selection in a bistable system, in which both striped and spotty patterns are possible states. Then I will present results showing morphological changes while moving continuously from a quasi-two-dimensional system to a three-dimensional system in BVAM and Lengyel-Epstein models. This chapter is concluded with some results of complex spatio-temporal dynamics in the BVAM model.

5.1 Methods

To solve differential equations by computer one has to discretize the space and time of the problem, i.e., to transform it from an infinite dimensional (continuous) to a finite dimensional (discrete) form. In practice the continuous problem defined by the reaction-diffusion system is solved in a discrete domain with $M \times N$ lattice sites (in 2D). When the problem is solved in three dimensions, the size of the fixed domain is $M \times N \times P$ grid points. For simplicity, the equations are usually solved in a square or cubic mesh, but one can use also, e.g., triangular mesh. The spacing between the lattice points is defined by the lattice constant dx. In the discrete system the Laplacian describing diffusion is calculated using finite differences, i.e., the derivatives are approximated by differences over dx. For $dx \to 0$ the differences approach the derivatives. The time evolution is also discrete, i.e., the time goes in steps of dt. The time evolution can be solved for example by using the so-called Euler method (Press et al., 1995), which means approximating the value of the concentration at the next time step based on the change rate (slope) of the concentration at the previous time step.

Details of the discretization and stability analysis of the numerical scheme are presented in appendix A.3. By employing the von Neumann stability analysis (Press et al., 1995) we found the discretization values $dx = 1$ and $dt = 0.05$ suitable for the BVAM model (see appendix A.3). In these types of problems the finite difference scheme and Euler method (Harris and Stocker, 1998) are often employed (Karttunen et al., 1998; Barrio et al., 1999; Dolnik et al., 2001a). It is possible, and sometimes even desirable, to use the Euler method since it is fast and stable under appropriate conditions, which can be checked by simple linear stability analysis. The Euler scheme has been shown to be stable for the BVAM model even in a radial disc domain, where step control was needed (Aragon et al., 2002). The resolution of the spatial discretization does not affect the pattern selection provided that the characteristic wave length of the pattern is a multiple times the lattice constant (dx). We have performed extensive simulations for system sizes up to 5×10^5 lattice cells and let the system to evolve up to 2×10^6 time steps in order to reach a stationary state.

5.2 General results[1]

In numerical simulations Turing systems are often solved in a two-dimensional square domain of fixed size, but also the effect of domain symmetry (Barrio et al., 2002) and growing domains have been studied (Madzvamuse et al., 2003). We have extended the study of Turing pattern formation to three-dimensional sys-

[1] The work presented in this section has been published in Leppänen et al. (2002) and Leppänen et al. (2004a).

tems. The initial concentration distribution corresponds to random perturbations around the trivial stationary state ($(u_0, v_0) = (0, 0)$ in the BVAM model) with a variance significantly lower than the amplitude of the final patterns. The boundary conditions can be chosen to be either periodic or zero-flux. If not otherwise stated, we have used periodic boundary conditions. The parameters were chosen based on the mathematical analysis carried out in the previous chapter.

5.2.1 Simulations in two dimensions

The most often observed patterns in two-dimensional Turing systems include parallel stripes and hexagonally arranged spotty patterns as discussed in the previous chapter. While selecting parameters for the simulation, one must first determine the linearly most unstable mode by fixing the coefficients of the linear terms in the model. In the previous chapter we found two parameter sets that correspond to the most unstable wave numbers, $k_c = 0.45$ and $k_c = 0.85$. The higher the wave number, the shorter the characteristic length $\lambda_c = 2\pi/k_c$ of the pattern. On the other hand, the nonlinear parameter C adjusts morphology selection. In the previous chapter we found out that small values of C result in stripes, whereas with $C > 0.084$ one may obtain spots.

Figure 5.1 shows results from a numerical simulation in a two-dimensional 128×128 domain. The spotty pattern was obtained by using $k_c = 0.45$ and $C = 1.57$. The striped pattern, on the other hand, corresponds to $k_c = 0.84$ and $C = 0$. Based on these results we can also notice the failure of the weakly nonlinear approximation, which predicted none of the patterns to be stable for high nonlinearities ($C > 0.611$). Both systems were simulated for 1 000 000 iterations starting from an initial state with Gaussian perturbations with zero-mean and a variance of 0.01. From Fig. 5.1 one can easily notice that the characteristic length of the spotty pattern ($\lambda_c = 14.0$, about 9 spots fit to the box with side length 128) is approximately twice the characteristic length of the striped pattern ($\lambda_c = 7.4$, about 17 stripes).

The final Turing patterns are stationary, i.e., they do not change as a function of time. In the presence of a Turing instability the chemical evolution approaches the final stationary state asymptotically, which is why one observes imperfections in the patterns obtained from numerical simulations. Concerning the patterns in Fig. 5.1, the stripes would most probably become straight and arrange in parallel if one continued the simulation indefinitely long. In the hexagonal lattice of spots the imperfections manifest in the form of topological defects or dislocations (Karttunen et al., 1999). Since one cannot simulate indefinitely, one can, for example, measure the change in the concentration at a particular site and stop the simulation as the time derivative of the concentration becomes sufficiently small.

Figure 5.2 shows how a two-dimensional pattern changes as the nonlinear parameter is gradually changed. One should notice that there is a very narrow

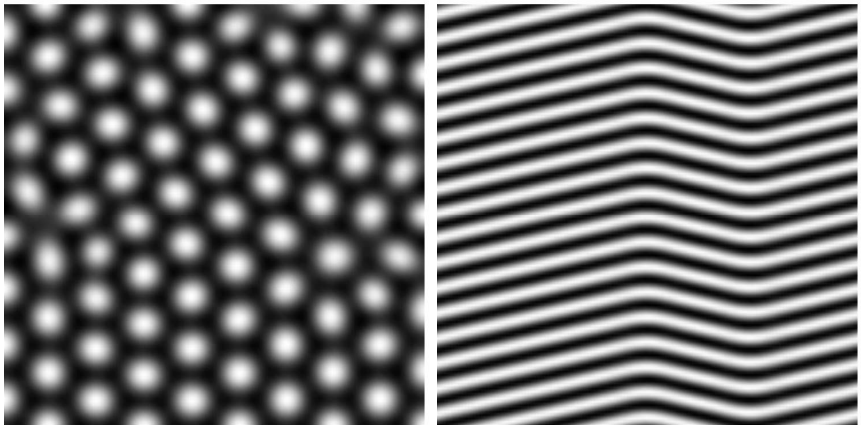

Figure 5.1: The stationary concentration patterns obtained in simulations of a two-dimensional system of size 128×128. The patterns arise due to instability of inhomogeneous infitesimal perturbations around the stationary state during the evolution lasting up to 1 000 000 iteration steps.

parameter regime, where the pattern changes from predominantly spotty to predominantly striped. The bottom row of Fig. 5.2 shows the diffraction patterns or structure factors defined with help of the Fourier transforms of the concentration field w given by

$$S(\vec{k}) = \int_0^\infty (w(\vec{x}) - \overline{w}) e^{i\vec{k}\cdot\vec{r}} d\vec{r}, \tag{5.1}$$

where $\overline{w}$ is the average concentration of the stationary distribution w obtained from the computer simulation. The diffraction patterns shown in Fig. 5.2 describe the magnitude $|S(\vec{k})|^2$ of the unstable wave vectors with respect to their orientation (see also Sec. 5.3). The morphological transitions taking place in the bistable region are discussed in more length in Sec. 5.4.

5.2.2 Simulations in three dimensions

In three dimensions there are more possible morphologies. Previously three-dimensional Turing structures have been studied by initializing an appropriate symmetry to the system to guide the chemical mechanism (De Wit et al., 1992, 1997), whereas we study spontaneous formations of structures from random initial configurations. From the structures visualized in Fig. 5.3 it is clear that the competition between the modes in the three-dimensional Turing system can lead to very interesting morphologies, when starting from an random initial state. The structures on to the top row of Fig. 5.3 were obtained by using the parameters corresponding to stripes in two dimensions ($C = 0$), whereas the structures on

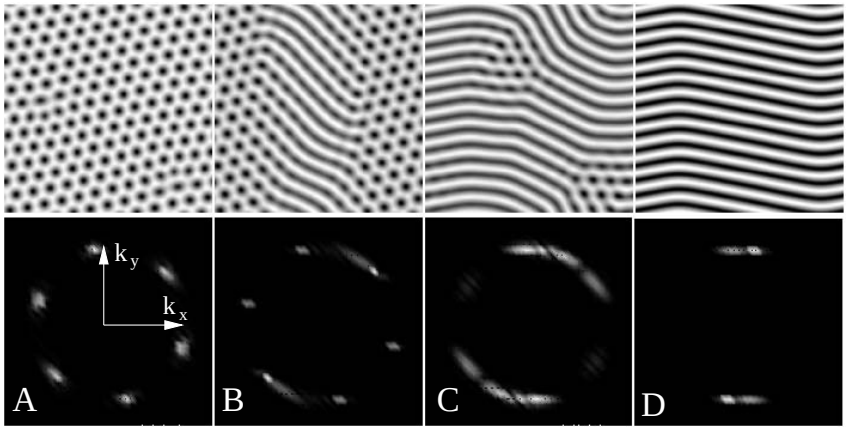

Figure 5.2: Transition from spots to stripes in the real space (top row) and the corresponding diffraction patterns in wave vector (k_x, k_y)-space (bottom row). The patterns have been obtained from random initial conditions after 500 000 iterations in a 200×200 system with $k_c = 0.45$. The nonlinear parameter was from left to right $C = 0.289$, $C = 0.131$, $C = 0.127$ and $C = 0$. In the real space black corresponds to areas dominated by chemical U and the lighter color by chemical V. In the reciprocal space $(k_x, k_y) = (0, 0)$ is in the middle of the diffraction pattern.

the bottom row correspond two-dimensional spotty patterns ($C = 1.57$). The columns in Fig. 5.3 correspond to the most unstable mode, which is $k_c = 0.45$ on the left column and $k_c = 0.85$ for the right column.

The straightforward extension of two-dimensional stripes in three dimensions would be lamellar planes with periodicity to only one direction. The results in Fig. 5.3a-b, however, do not show this kind of ordering, but instead one observes complex aligned lamellae, which is characterized to have both positive and negative local principal curvature. One can think of it as a superposition of plane waves, i.e., aligned planes crossing each other forming a continuous minimal surface. The system dynamics is unable to organize the three-dimensional structure into a more regular shape due to increased degeneracy of the three-dimensional system (see Sec. 3.1.3). In the case of enhanced quadratic nonlinear interaction (Fig. 5.3c-d) one obtains three-dimensional spherical droplets as one would expect, but their packing is not SC, BCC or FCC.

In two dimensions it seems that all the patterns combining stripes and spots (see Fig. 5.2) are transient, i.e., only one symmetry will eventually dominate in a system as the simulation is continued long enough. In three dimensions it does not seem to be so. Fig. 5.4 shows a structure that was obtained after 2 000 000 time steps. The unstable wave mode corresponds to the structures in Fig. 5.3a and c ($k = 0.45$). The control parameter C is, however, between those resulting in pure

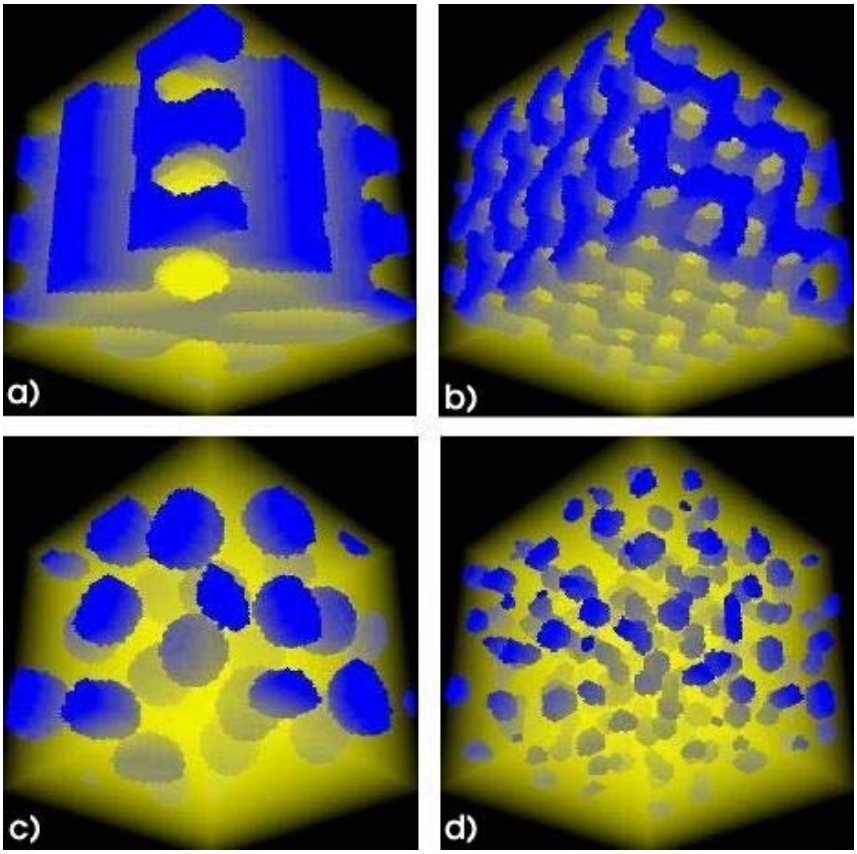

Figure 5.3: The stationary concentration structures obtained in simulations of a three-dimensional system of size $50 \times 50 \times 50$. The patterns arise due to instability of inhomogeneous infitesimal perturbations around the stationary state during the evolution lasting up to 500 000 iteration steps. The parameters were a) $C = 0$, $k_c = 0.45$, b) $C = 0$, $k_c = 0.85$, c) $C = 1.57$, $k_c = 0.45$, d) $C = 1.57$, $k_c = 0.85$.

lamellae or pure droplets ($C = 0.119$) and one can easily notice that the resulting structure is different from any of the structures presented in Fig. 5.3.

If one uses spatially inhomogeneous initial conditions favoring particular structure, the system dynamics may be confined to only a small part of the phase space and one can obtain the chemical concentration patterns that one would expect to be optimal. For example, by introducing the chemical U only to the mid-plane and V everywhere as random perturbations one obtains lamellar planes that are aligned according to the symmetry imposed by the initial condition (see Fig. 5.5). By introducing an initial concentration distribution close to hexagonally packed cylinders, one obtains the HPC structure as shown in Fig. 5.5. Similarly, a BCC

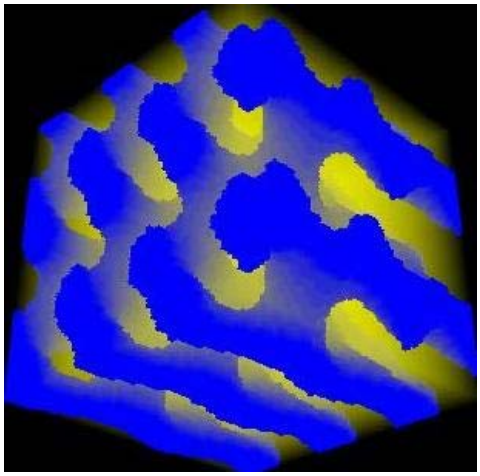

Figure 5.4: The concentration surface obtained in simulations of a three-dimensional system of size $50 \times 50 \times 50$ with the control parameter between those resulting in lamellae and droplets ($C = 0.119$). One can see that both the linear and radial characteristics are combined in the final structure.

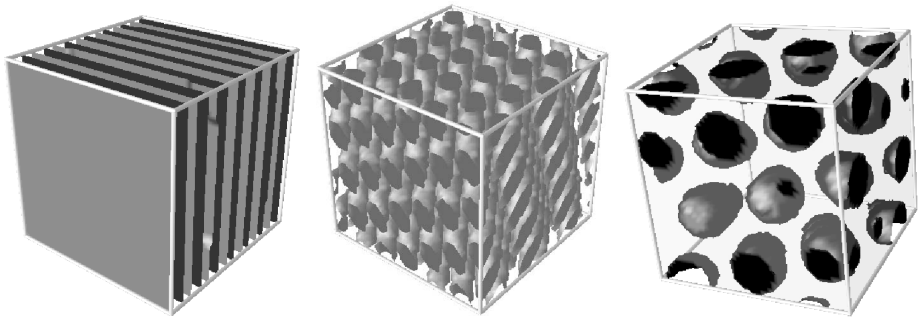

Figure 5.5: Starting from non-random initial conditions simulations of a three-dimensional system ($50 \times 50 \times 50$) may result in planar lamellae ($k_c = 0.84$, $C = 0$), hexagonally packed cylinders ($k_c = 0.84$, $C = 0.754$) or BCC droplets ($k_c = 0.45$, $C = 1.57$) after 400 000 iterations.

symmetry in the initial conditions results in a droplet structure with BCC symmetry. These structures resemble those that have been predicted and simulated in diblock copolymer melts (Matsen and Bates, 1996; Groot et al., 1999) and also those obtained by De Wit et al. (1992) using the Brusselator model.

The pattern selection can be understood by considering the phase space of the system. The dynamics and evolution of a particular morphology is governed by

the parameters of the model. For dominating cubic nonlinearities (low C) the system favors linear symmetry (planes), whereas dominating quadratic nonlinearity (high C) should result in radial symmetry (droplets). There are numerous possible three-dimensional structures that satisfy the symmetry requirements imposed by the nonlinearities. The planar lamellae correspond to the case, where there is only one growing (unstable) wave vector $\vec{k}_c = (k_c, 0, 0)$ and no degeneracy. This situation can be made more likely by using initial conditions that have this symmetry instead of random initial configuration, which does not favor any symmetry and enables all possible superpositions of plane waves such that $|\vec{k}_c| = k_c$. The closer the initial structure is to a state that satisfies the symmetry requirements, the smaller is the phase space that the system explores. It should be noticed that the system may find states shown in Fig. 5.5 also from random initial configuration. The probability of this happening, however, is very small. Nevertheless, we have observed the formation of the HPC structure from a random initial configuration in our computer simulations.

The complex three-dimensional lamellar surfaces generated by the Turing mechanism (see top row of Fig. 5.3) are interesting, since their existence is difficult to study analytically and the grounds of the state selection are not known. Most probably the system is trying to form some kind of minimal surface with respect to curvature. Numerous surfaces of this kind have been observed and characterized for example in the context of amphiphilic systems and block co-polymer melts (Matsen and Bates, 1996). Ball (2001) offers very clear illustrations of the so-called D-, G-, and P-surfaces.

There is an optimal minimal surface for connecting perpendicular planes such that the local principal curvatures (c_1 and c_2) have opposite signs yielding zero local mean curvature ($H = (c_1 + c_2)/2 = 0$). This surface is called a Scherk surface, which is a well-known minimal surface solution for twisted lamellar surfaces (Thomas et al., 1988). A stable Scherk surface has previously been observed in the case of the Brusselator model by initializing the minimal surface into the system (De Wit et al., 1997). In Fig. 5.6 we show the final structure obtained in a simulation by initializing the chemicals into two perpendicular planar domains. It is more favorable for the system to connect the perpendicular domains with a minimal surface than to align one half of the system to match with the orientation of the other. Based on the close-up of one of the connections we notice that also spontaneous formation of the Scherk surface is possible in the BVAM model.

5.3 Effect of noise[2]

The stability and robustness of Turing patterns can be studied by randomly varying the chemical concentration in the system. If one thinks of the possible

[2]The work presented in this section has been published in Leppänen et al. (2003a).

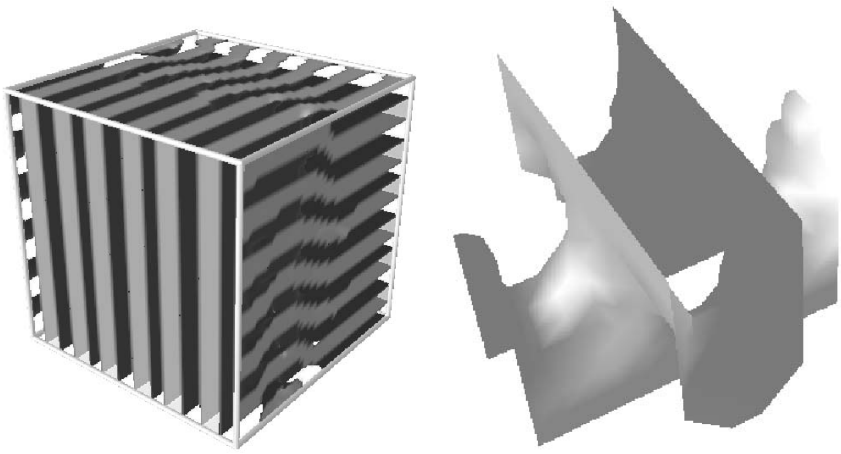

Figure 5.6: A minimal isoconcentration surface connects two crosswise planar structures in a three-dimensional $50 \times 50 \times 50$ system with $k_c = 0.84$ and $C = 0$. The close-up reveals the morphology of the Scherk surface.

biological applications of Turing systems, the robustness of patterns and structures is of great importance. Morphogenesis must be stable against random excitations to some extent and thus the mathematical models describing it must possess the same property. We will study the effect of Gaussian noise in the BVAM model and present results for both two- and three-dimensional systems.

Previously, the Brandeis group has extensively studied the effects of periodic forcing to Turing pattern formation experimentally in the photosensitive CDIMA reaction (see Sec. 3.3) (Horváth et al., 1999; Dolnik et al., 2001b,a; Berenstein et al., 2003). The robustness of the Turing mechanism has also been studied by introducing spatially inhomogeneous or defective reaction-diffusion mechanism (Bose and Chaudhuri, 1997). In addition, Sanz-Anchelergues et al. (2001) have shown both experimentally and numerically that Turing structures may still appear under spatially correlated external forcing provided that the correlation length of the forcing is not too small. This would imply that Turing structures possess some kind of error-correcting property.

In order to study the effect of noise we introduce a Gaussian noise source $\xi = \xi(\vec{x}, t)$ such that

$$\begin{aligned} u_t &= D\nabla^2 u + f(u, v) + \xi_u \\ v_t &= \nabla^2 v + g(u, v) + \xi_v, \end{aligned} \tag{5.2}$$

where the first and second moments of ξ are defined as

$$\begin{aligned} \langle \xi(\vec{x},t) \rangle &= 0 \\ \langle \xi(\vec{x},t)\xi(\vec{x}',t') \rangle &= A^2 \delta(\vec{x}-\vec{x}')\delta(t-t'). \end{aligned} \tag{5.3}$$

The angular brackets denote an average and A is the intensity of the noise. Noise is added at every time step to each lattice site of the system. Because of the discretization, the noise has to be normalized such that

$$\xi = A(dx)^{d/2}/\sqrt{dt}, \tag{5.4}$$

where d is the dimension of the system, dx the lattice constant and dt the time step. As discussed in Sec. 5.1, we have used the values $dx = 1$ and $dt = 0.05$ in the simulations. We used periodic boundary conditions and initially both chemicals were introduced randomly over the whole system.

Figure 5.7 shows a two-dimensional spotted pattern under noise for four different intensities with system parameters $k_c = 0.45$ and $C = 1.57$. Here we have used spots in a two-dimensional square lattice as a special initial condition to create a metastable state in the system. The pattern shown in top-left corner of Figure 5.7 is in accord with system dynamics, but it is not the optimal state for spotty structures. If no noise is applied, the initial condition will persist and the system will remain indefinitely long in this metastable state. On the other hand, if any non-zero amount of noise is applied, a change from the simple square symmetry to a hexagonally symmetric lattice is observed (top row of Fig. 5.7), which is the optimal structure for two-dimensional spots. As the noise amplitude is further increased (bottom row of Fig. 5.7) to about 20% of the amplitude of the concentration wave, the spots still persist and the interfaces are clearly visible although they are noisy and not round.

In materials science the structure factor is commonly used to describe the structural properties of a material (see e.g. (Ashcroft and Mermin, 1976)). According to Braggs' idea of constructive and destructive interference of scattered X-rays, characteristics of the structure can be concluded based on the distribution of scattered X-rays. For an atomistic system the structure factor is defined by the Fourier transform of the pair correlation function. In the context of Turing systems we do not have atoms but a uniform scalar field defined over the domain. In this case, the static structure factor is just a straightforward Fourier transform of the stationary concentration field (see Eq. (5.1)). Often one is interested in the magnitude of the structure factor, i.e., the power spectrum defined as $S(\vec{k},t)S^*(\vec{k},t) = |S(\vec{k},t)|^2$. The power spectrum is typically not examined with respect to the wave vector $\vec{k}$, but wave number k, which gives the characteristic length of the pattern.

Figure 5.8 shows the power spectrum $|S(k)|^2$ for three different noise intensities in the case of spots. The solid line represents the case of a hexagonal lattice

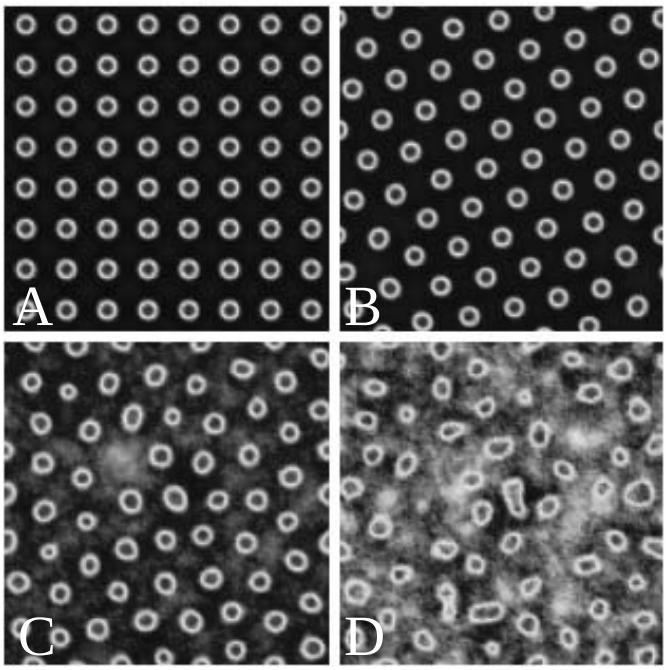

Figure 5.7: Two-dimensional spotty pattern in a 128×128 system. The amplitude of the noise A was A) 0, B) 0.01, C) 1.0 and D) 2.0, corresponding to $0 - 20\%$ of the amplitude of the modulated concentration wave.

without noise. There are two peaks, the higher one corresponding to the separation between spots and the lower one to their diameter. As the intensity of the noise is increased, the lower peak is not present anymore since the spots are no longer spherical (bottom right corner of Fig. 5.7). For very high noise intensity the spectrum becomes uniform for $k < k_c = 0.45$.

The three-dimensional droplet structures corresponding to the parameters of two-dimensional spotty patterns proved to be extremely robust against noise. Figure 5.9 shows a droplet structure without noise and in the presence of noise with intensity of 30%. The domains between the spheres become noisy and interfaces deformed. However, even when the relative noise intensity exceeds 50% one can still locate the domain boundaries. By comparing Figs. 5.8 and 5.10 one can see that the three-dimensional structures are more robust against additive Gaussian noise than the two-dimensional patterns. The characteristic length is present in the power spectrum of the three-dimensional system (Fig. 5.10) for much higher noise intensities, although the peak is very broad due imperfections in the structure (the distances between the droplets are not constant) and finite-size effects. The peak near zero in Fig. 5.10 describes system-sized correlations in the noisy

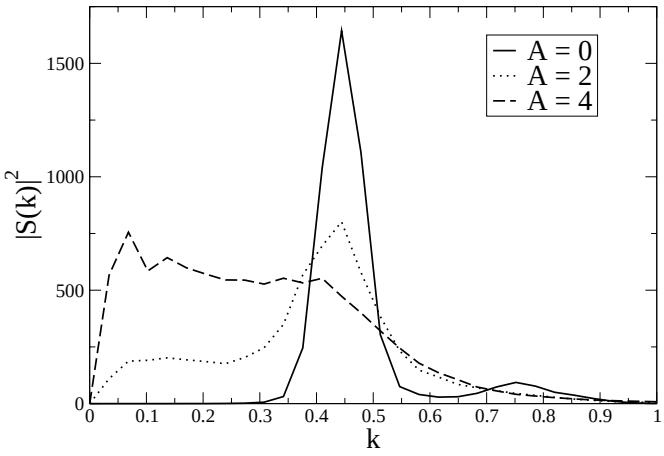

Figure 5.8: The power spectrums for three different noise intensities in two-dimensional, $A = 0$ (solid), $A = 2$ (dotted) and $A = 4$ (dashed line). The pattern ($k_c = 0.45$) fades into noise.

system.

When the quadratic interaction favoring spots is dominant (large C) the amplitude is always almost two decades larger in comparison to the case when the cubic interaction favoring stripes prevails (small C), i.e., the spotty pattern sustains over 100 times higher noise intensity as compared to the stripes or lamellae. We have also studied the effect of noise to stripes in two dimensions and planar lamellae in three dimensions. Figure 5.11 shows the expected results of the melting of a two-dimensional striped pattern as the amplitude of the noise is increased. The use of the conditions for the three-dimensional planar structure (see Sec. 5.2.2) results in perforated lamellae in the presence of noise as shown in Fig. 5.12.

The studies showed that Turing patterns are robust irrespective of the dimensionality of the system. The three-dimensional structures remain more ordered under intensive noise than two-dimensional patterns. This is what one would expect based on statistical mechanics, where the robustness of the system often increases as the dimension increases. The fact that the patterns evolve and persist under signal to noise ratio of 2 to 1 is remarkable. An additional effect of the noise is that the simulation time for finding the final structure decreases exponentially as a function of the noise amplitude even in the presence of very weak noise, because the noise facilitates overcoming metastable states during the evolution. One can decrease the simulation time to one fifth by applying a noise that does not affect

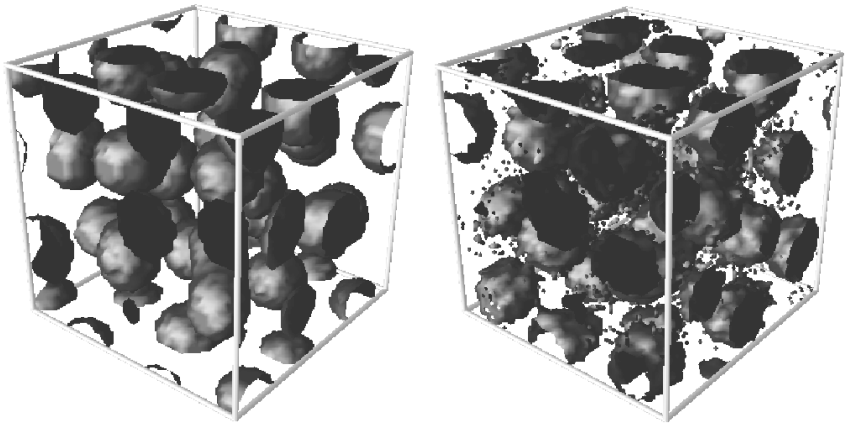

Figure 5.9: Three-dimensional droplet structure in a $50 \times 50 \times 50$ system. Left: No noise; Right: $A = 3$ corresponding approximately to 30% of the amplitude of the modulated concentration wave.

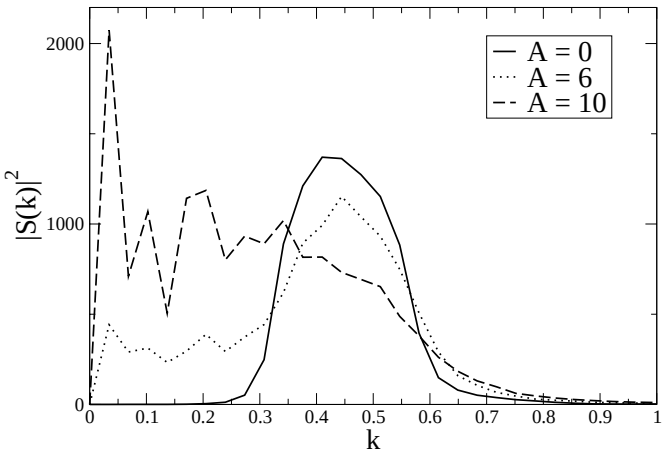

Figure 5.10: The power spectrums corresponding to three-dimensional droplet structures with noise amplitudes $A = 0$ (solid line), $A = 6$ (dotted) and $A = 10$ (dashed). The pattern ($k_c = 0.45$) is extremely robust.

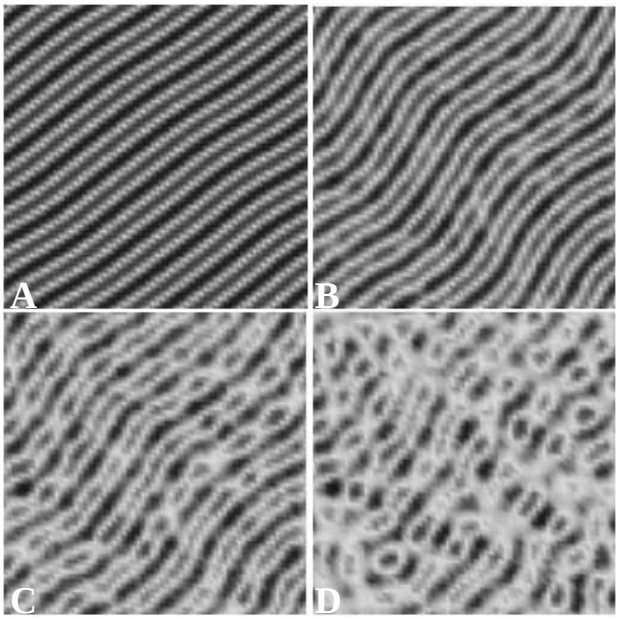

Figure 5.11: Two-dimensional striped pattern in a system of size 64×64 with parameters $k_c = 0.45$ and $C = 0$. The amplitude of the noise is A) $A = 0$, B) $A = 0.02$, C) $A = 0.04$ and D) $A = 0.06$ corresponding approximately to $0 - 40\%$ of the amplitude of the modulated concentration wave.

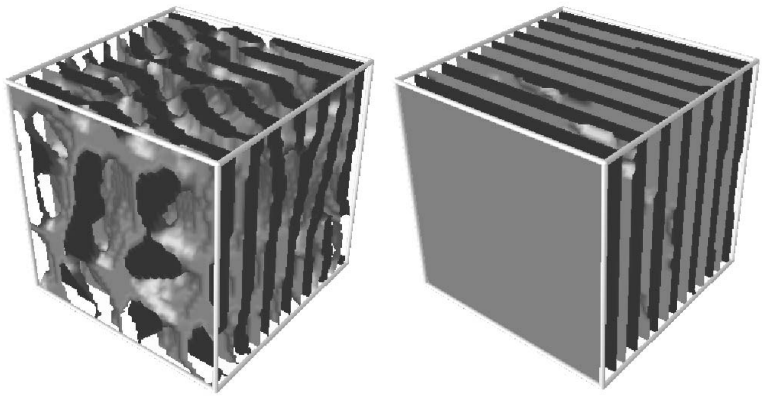

Figure 5.12: Three-dimensional planar structure in a system of size $50 \times 50 \times 50$ with $k_c = 0.85$ and $C = 0$. The structure on the left is without noise and the one on the right with the noise amplitude $A = 0.02$, which corresponds approximately to 10% of the amplitude of the modulated concentration wave.

the morphology in any noticeable way. The method is very effective while applied to numerical integration of reaction-diffusion equations (Press et al., 1995).

5.4 Morphological transitions and bistability[3]

The studies of Turing systems have typically concentrated on reaction kinetics and stability aspects (see e.g. Lengyel and Epstein (1992), Szili and Tóth (1993), Rudovics et al. (1999) and Judd and Silber (2000)), while the issues of pattern structure and connectivity have received less attention. In this section we focus on the connectivity of Turing patterns and its dependence on the parameters of the system. We present a simple way to quantitatively characterize Turing structures and their connectivity based on statistical analysis of the patterns obtained from simulations. The connectivity of a pattern with given parameters cannot be predicted analytically in the presence of bistability of both striped and spotty patterns. We also study the "connectivity transition", which occurs when the parameters of the system are between those giving rise to either spots or stripes in two dimensions (monostable regime) or lamellae and droplets in three dimensions. We will first discuss the concept of connectivity in these systems and the methods for characterizing the transition between different patterns and structures. We then present results of our extensive numerical simulations and discuss their importance.

The state selection is a fundamental problem in non-equilibrium physics and appears in very different contexts ranging from driven superconductivity (Tarlie and Elder, 1998) to chemical systems (Landauer, 1975; Nicolis and Prigogine, 1977). In this paper we address this problem in the context of reaction-diffusion systems (Metens et al., 1997) and characterize the pattern selection in the presence of a bistability by analyzing the statistical properties of the resulting patterns in systems with different sizes. The transition between monostable patterns can occur only through a bistable regime, where the pattern selection will be shown to be probabilistic. This non-equilibrium transition bears some resemblance to a first order equilibrium phase transition: the system exhibits hysteresis. This phenomenon has been addressed previously in the context of reaction-diffusion systems. Hysteresis has been observed in experimental (Ouyang et al., 1992) as well as numerical (Dufiet and Boissonade, 1992) studies of Turing systems, but the transition mechanisms have not been studied in great detail.

In the numerical simulations of the BVAM model (Eq. (4.10)) one deals with two concentration fields with characteristic wave lengths. In order to visualize this, the concentration of only one of the chemicals is typically plotted with a gray scale, since in these system the fields are in anti-phase, i. e., if there is a large amount of chemical U in some sub-domain, the concentration of chemical

[3]The work presented in this section has been published in Leppänen et al. (2004b).

V would be low there. These concentration fields vary continuously having diffuse boundaries. Now, the connectivity of chemicals in the system can be studied by defining sub-domains dominated by either chemical U or V, provided that the amplitude of the pattern is large enough. If we define the boundary as the interface between sub-domains dominated by different chemicals, we can easily locate the boundaries, where the concentrations change rapidly, typically within one or two lattice sites of the discretized system. Now, if two points belong to the same domain, i. e., are not separated by a boundary, they are considered to be connected. This definition of the boundaries is only conceptual in the sense that in the U-dominated domains the concentration of V does not have to be zero, only much less than the concentration of U.

In Fig. 5.13 we show changes in a two-dimensional concentration field for different values of the quadratic nonlinear coefficient C of the BVAM model. The patterns in Fig. 5.13 are snapshots taken after 50 000 iterations in order to make the transition more gradual and visible within a wider parameter range. This causes the patterns not being perfectly symmetric and leads to distortions. If one continued simulations for an indefinitely long time, Figs. 5.13A-E would most likely evolve towards aligned stripes, whereas Figs. 5.13F-I would evolve towards a hexagonal lattice of spots, i.e., the presented patterns are transient.

When the cubic term dominates (small C), the resulting stationary pattern is striped with a small number of imperfections, see Fig. 5.13A. These imperfections can be considered as topological defects, or dislocations, which could serve as nucleation sites for spots. More dislocations appear (see Figs 5.13B-C) when the relative strength of the quadratic term is made larger. As the quadratic term grows, more spots nucleate and they arrange themselves to hexagonal structure, and at the same time getting rid of the remaining stripes (see Figs. 5.13F-H). Similar nucleation processes have earlier been observed in numerical simulations of a reaction-diffusion system generating dissipative quasi-particles (Liehr et al., 2001). Finally, when the quadratic term is enhanced even further, only spots remain (Fig. 5.13I). As the present discussion concerning the nucleation of structure is purely qualitative it should be mentioned that, e.g., Hagberg and Meron (1997) have previously employed a more rigorous approach. They studied the dynamics of curved fronts in bistable two-dimensional media using a set of kinematic equations.

In this sequence of simulations the transition from stripes to spots was enforced by using a single control parameter C. Nevertheless, the transition from striped to spotty pattern seems to occur quite abruptly with respect to C. Note that the difference in parameters between the figures is not constant: From A to I, $C = 0.007, 0.091, 0.116, 0.124, 0.129, 0.135, 0.169, 0.258, 1.000$. In this context for $k_c = 0.45$ the bistability is predicted to occur for $0.073 < C < 0.139$, as discussed in Sec. 4.3. This corresponds to Figs. 5.13B-F.

Now, let us discuss the patterns in Fig. 5.13 from the clustering point of view.

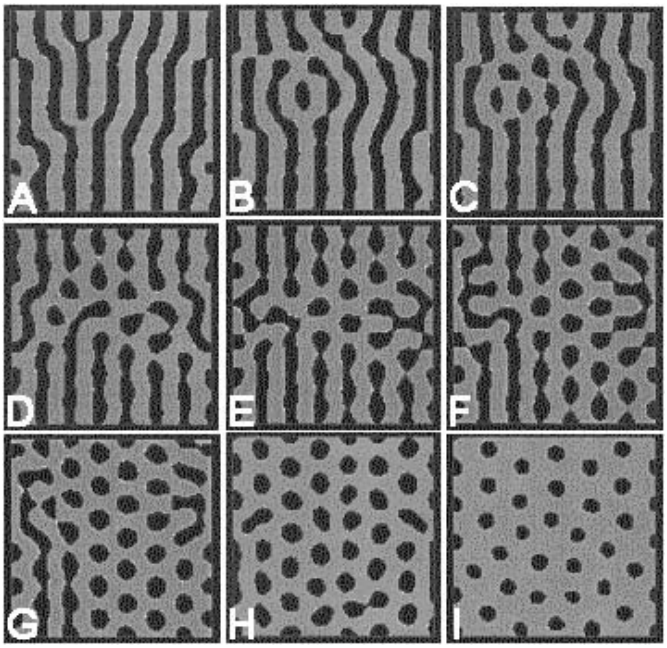

Figure 5.13: Transition from stripes to spots. The patterns obtained after 50 000 iterations in a 100×100 system with $k_c = 0.45$. Black corresponds to areas dominated by chemical U (zeros) and the lighter color chemical V (ones). C varies from 0.007 to 1.000 from A to I)

Since the interfaces are sharp, the situation can be simplified without loss of generality by assigning zeros and ones to the whole lattice based on the chemical that dominates a given domain. With this mapping we consider the number of clusters, which is calculated using the well-known Hoshen-Kopelman algorithm (Hoshen and Kopelman, 1976) as in typical percolation problems. In Fig. 5.13A one can see that in the case of stripes the number of U- and V-dominated clusters is almost the same, and both types are extended dominantly in one of the dimensions (both chemicals have percolated). However, in the case of a spotty structure (Fig. 5.13I), chemical U appears as separate round clusters or spots, whereas chemical V forms one connected cluster (V has percolated). Between these two limiting cases there is the transition region, depicted in Figs. 5.13D-F, where U-dominated clusters appear as spots and stripes in the form of a "string-of-pearls".

In order to compare the number of clusters $N(C)$ for systems of different size, we normalize it by dividing with N_c^d, where $N_c = k_c L/2\pi$, L denotes the linear system size (square or cube in 2D or 3D), and d the spatial dimension. N_c^d is the maximum number of spherically symmetric clusters in a d-dimensional system as if the clusters were uniformly distributed and the effect of boundaries

was neglected. Due to the periodicity of the chemical structure, the number of clusters in the d-dimensional system can be estimated to be $N^d = (N_c + 1/2)^d$. However, an additional correction is required to take into account the effect of boundaries. Now, one can estimate the number of additional partial clusters due to boundaries by approximating the length (area) of the boundary and the number of clusters within this domain ($d\,N^{d-1}$). As a result we propose the scaling function for the number of clusters to be

$$F_d(N(C), N_c) = \frac{N(C)}{N_c^d}\left(1 - \frac{d}{N_c + \frac{1}{2}}\right), \tag{5.5}$$

where $N(C)$ is the calculated number of clusters for control parameter C.

We studied the connectivity, or the number of clusters, in the patterns as a function of the control parameter C, which adjusts the morphology selection between stripes and spots. The first result is shown in Fig. 5.14, where we have plotted the number of U clusters, calculated using the Hoshen-Kopelman algorithm as a function of the nonlinear parameter C. Here we did not start from a random initial configuration, but instead started from a pattern corresponding to some value C_i, fixed $C_{i+1} = C_i + dC$, and let the pattern stabilize for 250 000 iterations. These three steps were carried out repeatedly. In this way we could change the control parameter C in steps and observe hysteresis (the direction is shown by the arrows in Fig. 5.14) characterized by the number of clusters. The bifurcation analysis discussed before predicts bistability for $0.084 < C < 0.161$. Numerical results shown in Fig. 5.14 do not match precisely, because as the control parameter is changed during the simulation, the present symmetry tends to persist. For longer stabilization times the hysteresis loop tends to become even wider, i. e., the bistability region widens.

Hysteresis has recently been observed while studying the space-averaged density of one substance in a one-dimensional reaction-diffusion system as a function of a feeding parameter (Rakos et al., 2003). We observe similar behavior also with respect to the amplitude of the concentration wave in the Turing system as earlier (Ouyang et al., 1992; Dufiet and Boissonade, 1991). We suggest that a transition exhibiting hysteresis can be further characterized by measuring the number of clusters in the case of reaction-diffusion systems forming spatial patterns. In addition to the hysteresis effect we have also observed a slowing down of the dynamics while the parameter C approaches the parameter region corresponding to morphological changes. For bistable C values the system requires more simulation steps to achieve the final steady-state. The scaling law is not easy to find since the transition point is not well-defined and the characteristic time is hard to measure exactly. Critical slowing down has been studied earlier both numerically (Reyes de Rueda et al., 1999) and experimentally (Ganapathisubramanian and Showalter, 1983; Ouyang et al., 1992) in bistable chemical systems.

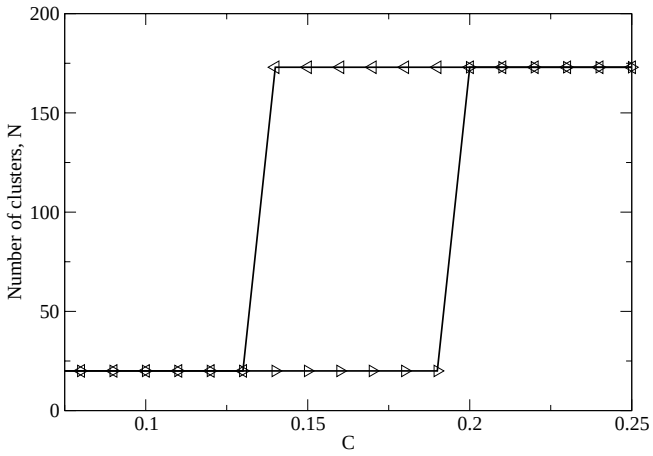

Figure 5.14: The number of U clusters as a function of the nonlinear parameter C, which was varied continuously throughout the sweep in a single simulation. The two-dimensional 100×100 pattern was given 250 000 iterations for stabilization at each value of C ($k_c = 0.86$). The arrow heads describe the direction of the sweep implying hysteresis.

The competition between hexagonal spotty patterns and stripe patterns has previously been addressed in the field of pattern formation both experimentally (Ouyang and Swinney, 1991; Ouyang et al., 1992) and numerically (Verdasca et al., 1992; Borckmans et al., 1992; Dufiet and Boissonade, 1992; Jensen et al., 1993). These studies do not, however, provide a method to investigate the morphological changes, but only corroborate the analytically predicted existence of both symmetries. In the following, we will try to find some insight into the morphological transition resulting in from the bistability of stripes and hexagonal spots. In order to study the transition we employ extensive numerical simulations and measure the number of clusters. The results were averaged over up to 20 simulations for each value of C. We carried out studies for several system sizes in order to guarantee the general nature of our results.

In Fig. 5.15 we plot the averaged scaling function $F_2(N(C), N_c)$ for U-clusters against C for several different system sizes. The simulations were started from random initial configurations of the chemicals for each value of C. Neglecting the number of V-clusters does not affect our conclusions, since the curves would be symmetrical (number of V clusters goes to 1 for high C). From Fig. 5.15 one can clearly see that the transition takes place at those values of the parameter C for

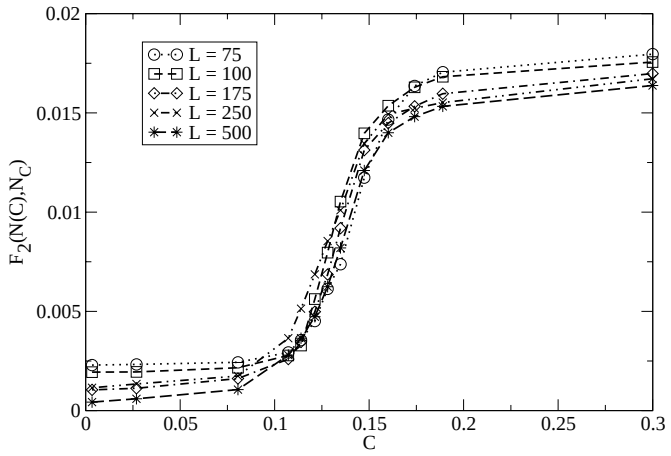

Figure 5.15: The normalized number of U clusters as a function of C in two-dimensional systems. System sizes are $L = 75$, $L = 100$, $L = 175$, $L = 250$ and $L = 500$. The results were averaged up to 20 simulations and they match with the analytical prediction for the bistable regime given by $0.084 < C < 0.161$.

which bifurcation analysis predicted the system to be bistable. In addition, it can be seen that the normalization function of Eq. (5.5) scales the number of clusters in such a way that the results for different system sizes agree within reasonable deviations.

The smoothness of the curve in Fig. 5.15, as compared to the data plotted in Fig. 5.14, is due to averaging. The boundaries of the hysteresis loop in Fig. 5.14 are not well-defined and the transition in a single simulation may take place for any value of C within the region of bistability. Thus Fig. 5.15 can be thought of as a normalized sum of step-like functions. In a system exhibiting bistability one cannot predict the exact transition value for a particular control parameter C. However, based on Fig. 5.15 it can be proposed that the predictions of the bifurcation analysis have the power to approximate the dynamics of bistable pattern formation in a probabilistic manner. For example, for $C = 0.15$ the bifurcation analysis predicts a bistability, but based on our simulation results, we suggest that when the system is initialized to a random state it will tend to evolve towards a hexagonal spotty pattern.

If one carries out the simulations for very small system sizes, finite-size effects can be observed. For small system sizes the $F_2(N(C), N_c)$ curves become more steep in the transition region and the value C for which the transition takes place

seems to be affected by the finite size of the system. This would suggest that in the limit of small systems, the transition would become almost discontinuous. However, the system cannot be made infinitely small since the (periodic) boundary conditions start to affect the behavior of the system. As discussed earlier, the spots tend to nucleate from topological defects, or dislocations, of the striped pattern (Fig. 5.13). In the case of a small system even one dislocation can affect the morphology of the whole system and thus quickly transform stripes into a lattice of spots. In a larger system many dislocations have to appear at various sites to give rise to spots which in turn make the appearance of more spots favorable.

So far we have discussed our simulation results only in two-dimensional systems. We have also studied the connectivity transition extensively in three dimensions. In this case stripes and spots become lamellae and spherical droplets, respectively. Figure 5.16 shows the concentration isosurfaces obtained in computer simulations with random initial configuration for four different values of C. From Fig. 5.16 one observes that in three dimensions one cannot obtain pure planar lamellae or organized spherical structures (FCC, BCC or HPC) spontaneously from random initial conditions. The linear structure we obtain in three dimensions is a continuous lamellae resembling a minimal surface solution (see Fig. 5.16A). The characterization of the various surfaces is difficult, but luckily the specific organization of qualitatively similar structures does not significantly affect the measured clustering in the structures. The fact that the cylindrical phase is predicted to be stable in SC-lattice for all parameter values C makes the structure selection even more complicated, especially in the transition region.

One would expect that in 3D the transition does not occur at the same point with respect to C as in 2D since the third dimension gives one more degree of freedom to the clustering process. This is indeed what one finds. Figure 5.17 depicts the normalized number of clusters for four different system sizes. One can see that the behavior of the system is different from that in two dimensions. Now, the transition occurs at a higher value of C, since a relatively smaller cubic nonlinear coupling favoring lamellar structures is sufficient for increasing connectivity in three-dimensional space.

The bifurcation analysis is not able to predict the transition domain in the three-dimensional case. The stable lamellae was predicted to change to stable spherical droplets at $C = 0.355$ corresponding to the border of the transition region in Fig. 5.17. The cylindrical structures were predicted to be stable for all C, which results in a bistability. The insufficient nature of the bifurcation analysis may further be due to the SC-lattice approximation. On the other hand, the stability of twisted lamellar surfaces could not be analyzed under any symmetry condition.

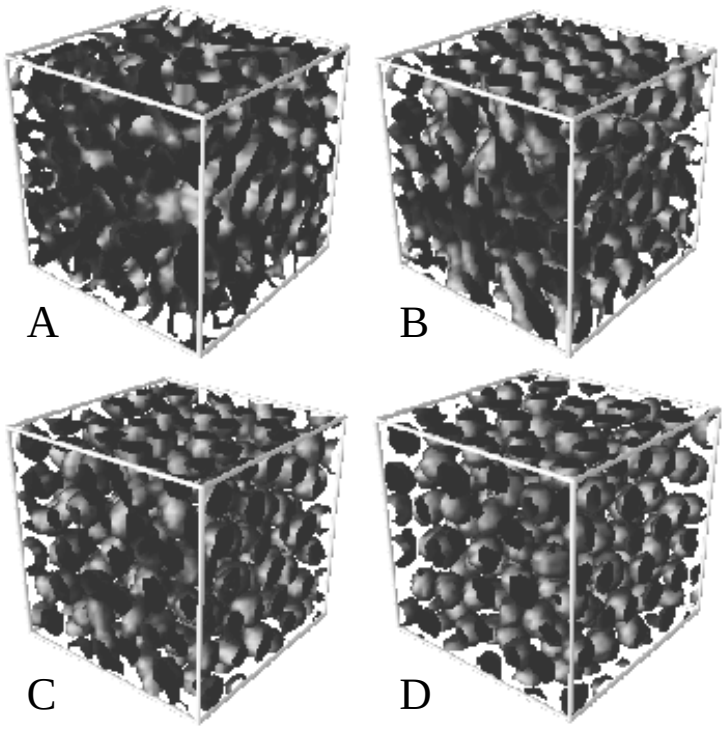

Figure 5.16: Transition from a twisted minimal surface to spherical shapes in a three-dimensional system of size $50 \times 50 \times 50$. The structures were obtained after 500 000 iterations with $k_c = 0.86$. The visualization was carried out by plotting the middle concentration isosurface. Parameter values: A) $C = 0$, B) $C = 0.44$, C) $C = 0.53$ and D) $C = 1.0$

Conclusions

In this section, we have investigated the connectivity of spatial patterns generated by the reaction-diffusion mechanism both in two- and three-dimensions. This was done by applying clustering analysis for the dominating chemical. The numerical simulations were consistent with the predictions drawn from the bifurcation analysis, and the system showed a transition in the proximity of the predicted C-value irrespective of the individual system size. The agreement with theory turned out to be better in the two-dimensional case than in three dimensions, since in two dimensions there is a simple transition between monostable patterns through a bistable regime. In three dimensions the analytical approximation of the changes in connectivity was more difficult, since the system was predicted to be bistable for all parameter values and no bistability was implied between lamellar

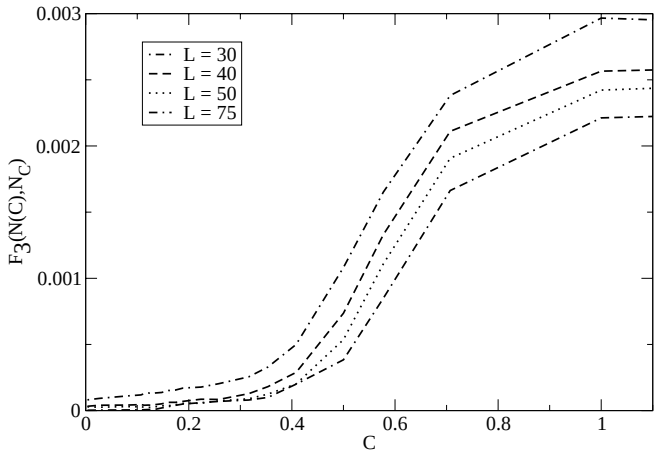

Figure 5.17: The averaged normalized number of U clusters as a function of C in a three-dimensional systems. System sizes are $L = 30$, $L = 40$, $L = 50$, and $L = 75$. The bifurcation analysis predicts unstable lamellar structures and stable SC-droplets for $C > 0.361$, whereas stable cylindrical structures are predicted for all $C < 0.65$.

and spherical structures in the SC-lattice. On the other hand, for the BCC-lattice the bifurcation analysis did predict a bistability, but the bistable values of the control parameter did not agree with the results of the numerical simulations as well as the predictions for an SC-lattice. Although the BCC-structures are stable in Turing systems, it seems that the system cannot find them when the simulation is started from a random initial configuration. In large systems of dissipative quasi-particles this kind of behavior has been hypothesized to be due to an instability of transient structures (Liehr et al., 2001).

The bistability of two different patterns is observed in a variety of chemical (Kapral and Showalter, 1995) and biological systems (Nagorcka and Mooney, 1985; Murray, 1989). The approach of this study brought more insight into the pattern selection in Turing systems. We have shown that at least in the context of Turing systems the pattern selection of a bistable system can be predicted probabilistically. We have also shown that the non-equilibrium morphological transition has characteristics similar to first order phase transitions, i. e., hysteresis is observed. Hysteresis can be seen not only with respect to the amplitude of the chemical concentration as earlier, but also with respect to the morphological changes, i. e., the averaged number of clusters. The fact that the system size does not affect clustering and pattern selection at all (given that system is not too small)

implies that the Turing mechanism is very general and it is applicable to systems of various sizes.

5.5 Dimensionality effects[4]

The study of the transition from two-dimensional patterns to three-dimensional structures is a more challenging than the direct comparison of the final results (Figs. 5.1 and 5.3). It has been shown that an experimental gel reactor with CIMA reaction may exhibit bistability, i.e., both spot and stripe patterns may appear into the gel on different heights (Ouyang et al., 1992). This has been explained by a concentration gradient that is imposed by the reactor (Ouyang et al., 1992). Turing patterns have also been studied in ramped systems, where the thickness of the gel is increased gradually and one observes qualitatively different patterns corresponding to different thicknesses (Dulos et al., 1996).

The problem has also been addressed more quantitatively by Dufiet and Boissonade (1996), who modeled pattern formation in a three-dimensional experimental reactor by imposing a permanent gradient on one of the bifurcation parameters in their model. This corresponds to the situation in an experimental reactor, where the concentrations are kept constant only on the feed surfaces, whereas the concentration inside the gel is governed solely by reaction and diffusion. Dufiet and Boissonade (1996) conclude that the patterns in quasi-2D reactors can, to a certain extent, be interpreted as two-dimensional patterns when the thickness of the gel L_z is less than the characteristic wavelength $\lambda_c = 2\pi/k_c$ of the pattern.

As for the effect of dimensionality in the BVAM model we have observed that the transition from a two-dimensional to a three-dimensional system is not at all simple. The structure selection is not deterministically governed by the thickness of the system. As one increases the thickness of the discrete system from a plane (with thickness dx), it will lose the correlation between the bottom and top plates gradually, but the transition thickness is not well-defined, i.e., thickness larger than the characteristic wave length ($L_z > \lambda_c$) does not seem to guarantee that the structure becomes truly three-dimensional. Figure 5.18 shows the resulting structures for two systems of nearly the same thickness $L_z > \lambda_c$ as one starts from different random initial conditions. One can easily observe that the leftmost structures is three-dimensional, whereas the rightmost is quasi-two-dimensional, although the latter structure grows in a thicker domain. The preliminary results presented in Fig. 5.18 were obtained by straightforward simulation of the Lengyel-Epstein model (see Sec. 3.2.3) with $\sigma = 50$, $d = 1.07$, $a = 8.8$ and $b = 0.09$, which is known to correspond to hexagonal patterns (Rudovics et al., 1999).

Based on our numerical studies using both the BVAM model (Eq. (4.10)) and the Lengyel-Epstein model (Eq. (3.24)) it seems that the probability that the

[4]The work presented in this section has been published in Leppänen et al. (2003b).

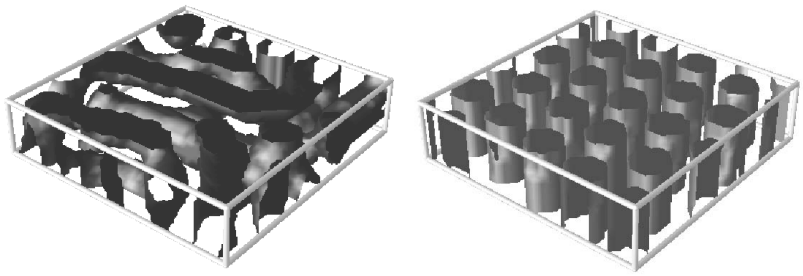

Figure 5.18: Structures obtained in a numerical simulation of the Lengyel-Epstein model in a domain of size $100x100xL_z$. The dimensionality of the pattern is not determined by the thickness L_z of the system alone. Left: $L_z = 12$. Right: $L_z = 13$. The system parameters are the same for both ($\lambda_c = 6.86$), but the random initial conditions are different.

pattern is quasi-two-dimensional is proportional to the number of linearly unstable wave vectors $\vec{k}$ with $n_z \neq 0$. Our simulations show that the number of three-dimensional final structures does not change monotonically as a function of the system thickness, but due to increasing degeneracy the dependence becomes very complicated. There is not any unique transition thickness, but the system chooses between a quasi-2D and 3D structure based on the unstable wave window, initial conditions and system thickness. The unstable wave modes, which are excited by the initial random perturbations and fit the simulation box the best form the structure.

From the numerical simulations one can measure characteristics of the morphologies (e.g. correlations, structure factors), which are difficult to measure from chemical patterns in a gel. In addition visualization of numerical results makes it possible to see into the structure. We have used the Lengyel-Epstein model reaction to analyze further the structures that have been reported from experiments in ramped systems (Dulos et al., 1996). Fig. 5.19 shows results of solving the Lengyel-Epstein model in a ramped system and there is some agreement with experimental results. One should note that both stripes and spots gradually change into complex three-dimensional tubular structures. It seems that three-dimensional experimental chemical patterns can be easily misinterpreted, because the depth information is lost in the 2D projection made for visualization. What seems to be a non-harmonic modulation may be just an aligned lamellae, and what seems to be a combination of stripes and spots may as well be tubes appearing to the observer as stripes if seen from the side and as spots if seen from the end.

As discussed above an important feature of experiments, which is absent in the numerical simulations is the gradients in the reactor. In a computer a given model can be solved to the computational precision, from which it follows that

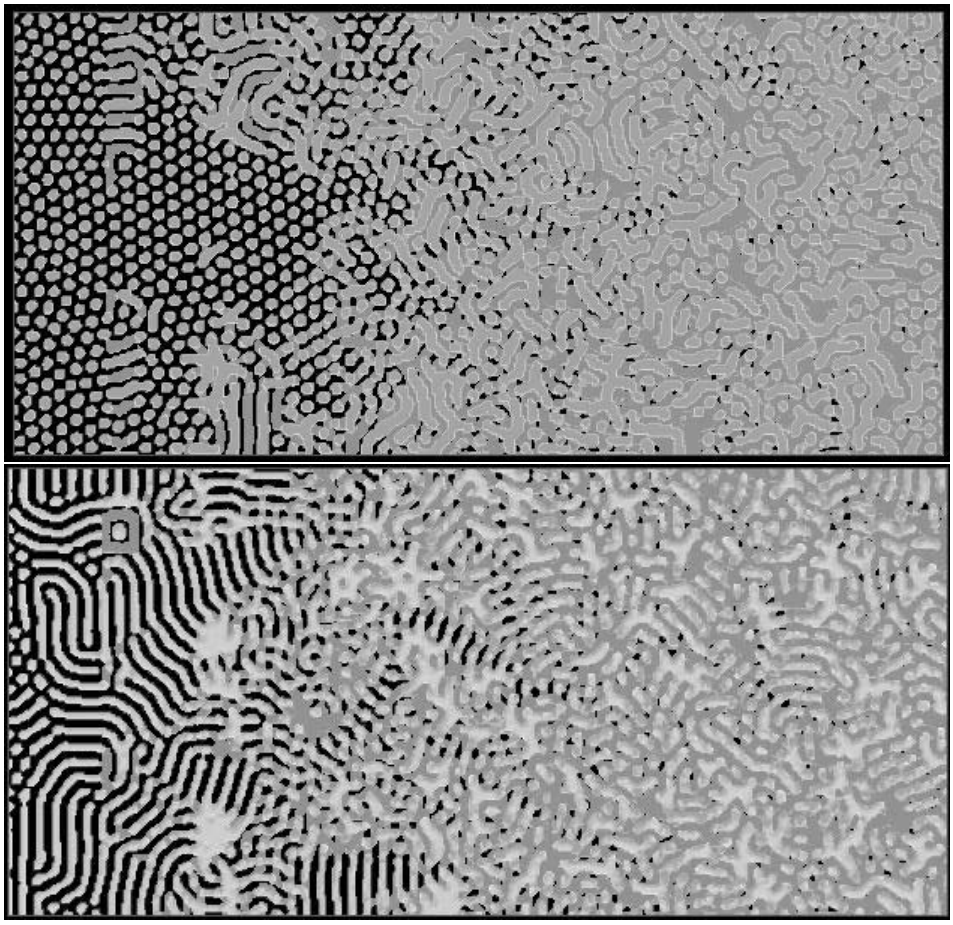

Figure 5.19: Simulations in a ramped system with dimensions 200×420. The thickness of the slab increases from $L_z = 1$ on the left to $L_z = 30$ on the right causing transition from clear quasi-two-dimensional to complex three-dimensional structures. Parameter for the Lengyel-Epstein model were $\sigma = 50$, $d = 1.07$ and $b = 0.39$ with $a = 12$ (top) and $a = 12.5$ (bottom).

if a model captures the phenomenon accurately, the results are accurate and there are no such artifacts as concentration gradients. If one thinks of applying Turing system in biological modeling, it is of great importance that the models imitate the real processes and there is nothing that skews the results. In biological tissue the sources controlling the parameters of the reaction would in part be in the cells and not always in the boundaries. Thus the gradients are not always present in biological morphogenesis. Hence the patterns obtained from numerical simula-

tions may in fact be better imitations of natural patterns than the patterns arising in experimental reactors.

5.6 Time-dependent behavior[5]

In this section we present results of studies of the BVAM model in the presence of a Hopf instability or more than one stationary state. Simultaneous instability of many stationary states results in competition between the bifurcations and the system can exhibit spatial, temporal and spatio-temporal pattern formation depending on the system parameters. We are interested in the coupling of Turing and Hopf bifurcations producing spatial patterns and temporal oscillations.

Although Turing instability leads to spatially periodic patterns that are stationary in time, in general a reaction-diffusion system can also exhibit a variety of spatio-temporal phenomena (Kapral and Showalter, 1995; De Wit, 1999). Hopf instability produces spatially homogeneous temporal oscillations and its relation to Turing instability is of great interest. This is because both instabilities can be observed experimentally in the CIMA reaction by varying the concentration of the color indicator in the reactor (De Wit, 1999; Perraud et al., 1992). The interaction between these instabilities (Rovinsky and Menzinger, 1992; Dewel et al., 1995) may take place either through a co-dimension-two Turing-Hopf bifurcation, when the corresponding bifurcation parameter threshold values are equal (De Wit et al., 1996; Rudovics et al., 1996) or due to different competing bifurcations of multiple stationary states (De Wit, 1999; Dewel et al., 1996). Both the situations lead to interesting spatio-temporal dynamics. In addition, Yang et al. (2002) and Yang and Epstein (2003) have recently obtained a variety of stationary and oscillating structures in the numerical simulations of a system with interacting modes

We have performed numerical simulations of the BVAM model (Eq. (4.10)) in two-dimensional domains of size 100×100 by using parameter values corresponding to different bifurcation and stability scenarios. On one hand, we have studied the interaction of Turing and Hopf bifurcations in a monostable system, and on the other hand, a tristable system with a coupled Turing-Hopf-Turing or Turing-Turing bifurcation. These conditions are able to produce a variety of spatio-temporal dynamics, whose characterization is very challenging. To enhance the temporal resolution of our simulations we used decreased the time step to $dt = 0.01$.

By using the parameters $D = 0.122$, $a = 2.513$, $h = -1$, $b = -.95$, $\nu = 0.199$ and $C = 1.57$ one can adjust the system in such a way that there is only one stationary state $(0, 0)$, which is both Turing unstable with $k_c = 0.85$ and characteristic length $L = 2\pi/k_c \approx 7.4$, and Hopf unstable with oscillation period of $T_c = 2\pi/\mathrm{Im}\{\lambda(k_0)\} \approx 25.40 = 2540 \times dt$ ($k_c = 0$). Eventually, the

[5]The work presented in this section has been published in Leppänen et al. (2004c).

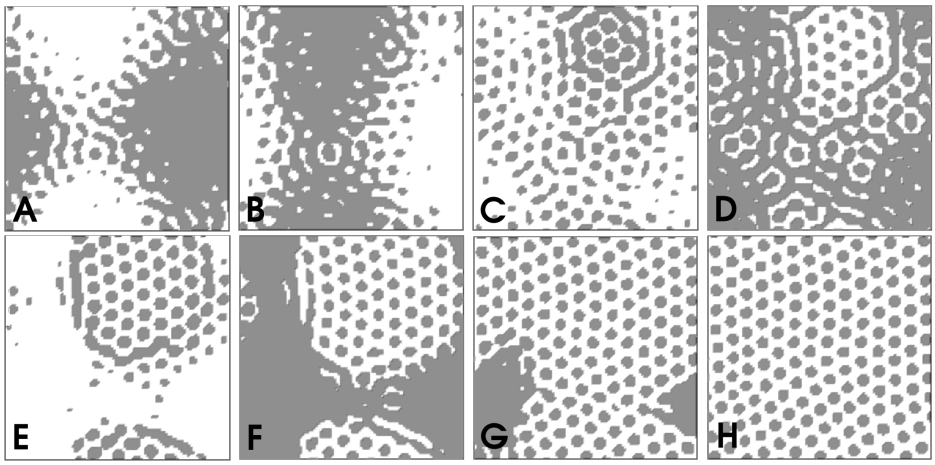

Figure 5.20: A two-dimensional concentration patterns obtained in a system with a coupled Turing-Hopf bifurcation as the simulation is started from a random initial configuration. White and gray domains correspond to areas dominated by chemical u and v, respectively. The time evolution goes from left to right and from top to bottom.

oscillations fade away and a stationary hexagonal spotty pattern is established. Fig. 5.20 shows snapshots of the behavior of the system at appropriate moments of time. The homogeneous domains changing color correspond to oscillations.

For $h \neq -1$ the BVAM model has three stationary states instead of only the trivial state $(0, 0)$. For $h < -1$ the stationary state $(0, 0)$ goes through a subcritical pitchfork bifurcation, i.e., it becomes stable, whereas two new unstable stationary states are established. For $h > -1$ a tri-instability is established, i.e., there are three (Turing) unstable stationary states. We fixed $h = -0.97$, which yields two additional stationary states and studied the pattern formation with other parameters $D = 0.516$, $a = 1.112$, $b = -0.96$ and $\nu = 0.450$, which correspond to a Turing-Hopf bifurcation of the state $(0, 0)$ with $k_c = 0.46$ and Turing bifurcation of the stationary states $(-2.01, 0.40)$ and $(9.97, -1.97)$, both with $k_c = 0$. The Turing-Hopf modes growing from $(0, 0)$ excite the former of these two states, which results in a coupling between Turing-Hopf and Turing instabilities. From random initial configuration the parameter selection $C = 1.57$, which corresponds to spotty patterns resulted in a hexagonal lattice with a few twinkling spots at dislocation sites. Twinkling hexagonal lattices of spots have previously been obtained in numerical simulations of a four-component Turing model (Yang et al., 2002) and of a nonlinear optical system (Logvin et al., 1997). Our results show that "twinkling-eye" behavior can also be observed in a two-component model without any special preparations.

Using the same parameters as above, except choosing $b = -1.01$ one still

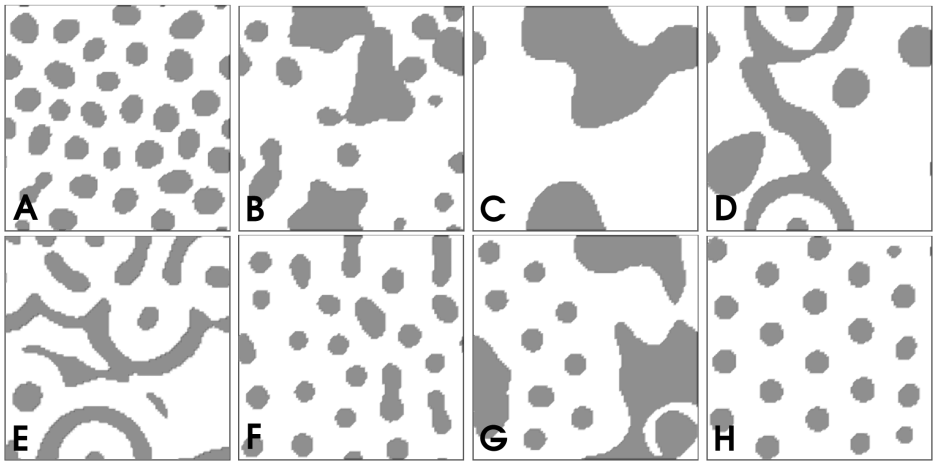

Figure 5.21: The two-dimensional concentration patterns obtained in a tristable system with a coupled Turing-Hopf-Turing bifurcation as the simulation is started from a random initial configuration. The time evolution goes from left to right and from top to bottom.

obtains a tristable system, although the stationary state $(0, 0)$ is no longer Turing-Hopf unstable, but Turing unstable with $k_c = 0.46$. The two other stationary states $(-1.191, 0.350)$ and $(6.529, -1.920)$ are unstable with $k_c = 0$ as in the previous case. Again the Turing modes growing from $(0, 0)$ excite another nearest stationary state, which results in an interesting competition between growing modes. Although there is no straightforward Turing-Hopf bifurcation, the modes growing from the state $(-1.191, 0.350)$ with $Re\{\lambda(k_0)\} > 0$ are coupled with the damped Hopf modes $\propto e^{i\omega_0 t}$ of the state $(0, 0)$, which results in oscillatory behavior with period $T_c \approx 3765 \times dt$. This dynamics is described by a series of snapshots in Fig. 5.21, where the homogeneous oscillations sweep out spots with period T_c, and then the spots are again nucleated at the centers of concentric target pattern waves. The competition continues for long times of up to $10^6 \times dt$, although the oscillations gradually fade out.

One should mention that for $C = 0$, which corresponds to striped patterns, the system showed a straightforward Turing bifurcation of the state $(0, 0)$ without any oscillatory competition. This happened because the Turing modes growing from the state $(0, 0)$ and resulting in stripes did not excite the other stationary states, i.e., the amplitude of the striped concentration pattern was not large enough for the modes to interact with other stationary states. Based on this observation, one can state that in multistable systems the parameter selection might have drastic effects on the dynamical behavior of the system.

Most of the earlier studies of spatio-temporal dynamics have been carried out in one-dimensional systems, since they make it feasible to study the Turing-Hopf

interaction by using amplitude equation formalism (De Wit, 1999; De Wit et al., 1996). In the two-dimensional case (not to talk about three dimensions) the studies of spatio-temporal behavior have typically, although not always (Dewel et al., 1995), been more or less qualitative. By considering stability and bifurcation aspects one can understand the behavior of the systems to some extent, but otherwise two-dimensional spatio-temporal dynamics is often too complex to be studied analytically.

Turing instability is not only relevant in reaction-diffusion systems, but also in describing other dissipative structures, which can be understood in terms of diffusion-driven instability (see Chaper 1). The studies of temporal and spatial pattern formation in Turing system are important, since they may be of great interest also in biological context, e.g. skin hair follicle formation, which is closely related to skin pigmentation, occurs in cycles (Nagorcka, 1989). Recently, spatio-temporal traveling wave pattern has been observed on the skin of a mutant mouse (Suzuki et al., 2003), which might perhaps be the result of a misconfigured Turing mechanism with competing instabilities, i.e., the pattern becomes temporal instead of stationary due to a shift in the values of the reaction and diffusion rates of morphogens.

Chapter 6

Conclusions

The first experimental observation of chemical Turing patterns some 15 years ago confirmed that the theoretical ideas hypothesized by Alan Turing almost 40 years earlier were not only mathematical formulations, but a pioneering contribution to the theory of nonlinear dynamics, non-equilibrium physics and mathematical biology. After 1990, Turing's seminal article has received more citations per year than it received in total during the first twenty years after its publication. In general, Turing systems can be defined as simple mathematical models, such as the BVAM model studied in this thesis, that can generate stationary concentration patterns and structures with a characteristic length from random initial configurations. A special feature of the Turing mechanism is that the characteristics of the resulting patterns are determined intrinsically by the reaction and diffusion rates of the chemicals involved in the process and not by any external control mechanism. In mathematical Turing models the length scale and morphology of the resulting patterns can each be adjusted with only one parameter. This means that for a fixed model the information of the morphology we wish to generate (stripes or spots) can be expressed by one number.

Turing's original motivation for studying pattern-forming properties of chemical systems was biological and it seems plausible that the spontaneous processes that occur in nature might be governed by some Turing-like mechanism. It would mean that the genome holds only the information required for describing specific structures, whereas the construction itself occurs due to fundamental physical laws. Of course, the model of a real biological mechanism would require possibly hundreds or even thousands of coupled partial differential equations and it would be impossible to solve. This was not, however, Turing's main point. The contribution of Alan Turing to mathematical biology is unequivocal in the sense that he was the first to show, how an amazingly simple mechanism can generate complex behavior and describe a wide variety of natural systems in a very generic way.

Although the work presented in this thesis might seem as having no self-evident applications in biology, especially the results of the structures generated by the Turing mechanism in three dimensions might be important in the biological context. Two-dimensional systems can be treated analytically and they are computationally fast to solve. The bifurcation analysis applied to three-dimensional pattern formation does not, however, capture the characteristics of the process as easily and due to increased wave number degeneracy one cannot predict the results of numerical simulations very well. As we saw in Chapter 5, already our two-component model could generate very complex three-dimensional twisted lamellar surfaces beyond the reach of quantitative measures. Thus, understanding the richness of spatial information that could be expressed by Turing systems consisting of possibly hundreds of morphogens calls for imagination.

In addition to the biological relevance of Turing systems, their ability to generate structure is of great interest from the point of view of physics. There are various physical systems that show similar phenomena, although the underlying mechanisms can be very different. Thus making fundamental theoretical contributions to the theory of pattern formation has proved out to be extremely challenging. Thus, most of the research in the field relies on experiments and numerical simulations justified by an analytical examination. The numerical simulations approach employed in this thesis seems promising since carrying out computations is much less cumbersome than carrying out experiments. In addition, in simulations one may study pattern formation under constraints that are beyond the reach of experiments and the numerical data is also easier to analyze.

In this thesis, I have presented the results of our studies of pattern formation in Turing systems. The main findings may be listed as follows:

1. The addition of morphogen sources into the Gray-Scott model gives rise to labyrinthine networks, which connect the sources in both two and three dimensions. It was proposed that Turing models could provide a plausible mechanism for the generation of chemical signaling pathways in biological systems, for example, in the context of neuronal growth (Sec. 3.2.2).

2. The stability regions of the BVAM model corresponding to different two- and three-dimensional symmetries were derived by applying nonlinear bifurcation analysis and the center manifold reduction technique (Chapter 4).

3. The initial configuration (random or almost random) and the parameters affect the formation of three-dimensional structures significantly due to increased degeneracy as compared to two-dimensional systems. In three dimensions one can observe, for example, minimal surfaces (Sec. 5.2.2).

4. Additive Gaussian noise does not inhibit Turing instability. The resulting morphologies are very robust against noise, although the effect of noise

is evident in the structure factor. The three-dimensional structures proved to be significantly more robust than the two-dimensional patterns, and the radial symmetries more robust than the linear symmetries (Sec. 5.3).

5. A quantitative cluster-based method devised for characterizing morphological transitions statistically as a function of the control parameter offers a probabilistic way for studying pattern selection in bistable systems, which are beyond the reach of analytical methods. Interestingly, it was observed that the system exhibits hysteresis with respect to the devised measure and a slowing down of the chemical dynamics is evident as the control parameter approaches the bistable (transition) regime (Sec. 5.4).

6. Studies with the Lengyel-Epstein model in domains growing to one direction revealed that the pattern selection in quasi-two-dimensional systems is strongly dependent on the aspect ratio of the domain and initial conditions. The condition that the shortest dimension of the system must be larger than the unstable wave length ($L_z > \lambda_c$) was found to be *necessary but not sufficient* for the formation of three-dimensional structures (Sec. 5.5).

7. The coupling of Turing and Hopf bifurcations combined with multistability results in complex spatio-temporal dynamics proving that a reaction-diffusion scheme can generically account for the basic processes present in many biological systems (spatial information and oscillations) (Sec. 5.6).

Perhaps the two most important results of this thesis deal with the conditions for the morphology selection of three-dimensional Turing structures (item 3) and the pattern selection in bistable two-dimensional Turing systems (item 5). We specified the conditions for the spontaneous formation of three-dimensional Turing structures from random or almost random initial configurations, whereas the earlier studies had mostly relied on numerical confirmation theoretically justified assumptions of the stable morphologies. Our study on the two-dimensional pattern selection in the BVAM model was the first effort made towards characterizing morphological transitions and pattern formation in bistable systems.

As a whole, our findings on the effect of the initial configuration, random noise, changes in the system parameters, bistability, thickening domain and competing bifurcations complement the knowledge concerning Turing pattern formation from their part. The theory of pattern formation has a close connection to the fundamental problems of non-equilibrium thermodynamics, which remain to be solved both in the context of Turing systems and also in the more general framework of non-equilibrium physics.

Appendix A

A.1 Derivation of coefficients for amplitude equations

In the following we will present the derivation of the parameters for the amplitude equations by employing the center manifold reduction explained in Sec. 4.3.2. The idea is to find out combinations of the wave modes and their contribution to the amplitude equations of a particular symmetry.

Two-dimensional hexagonal lattice

In the hexagonal lattice two wave vectors sum up to another wave vector. The vectors for the hexagonal lattice are given by $\vec{k}_1 = k_c(1,0)$, $\vec{k}_2 = k_c(-1/2, \sqrt{3}/2)$ and $\vec{k}_3 = k_c(-1/2, -\sqrt{3}/2)$. The strength of the quadratic coupling term is determined by the first term in Eq. (4.31). Since there are two possible selections (permutations) of m_1 and m_2, i.e., $-\vec{k}_3 - \vec{k}_2 = -\vec{k}_2 - \vec{k}_3 = \vec{k}_1$ one has to take into account both of them. Thus the quadratic coupling parameter of the corresponding amplitude equation (Eq. (4.20)) is given by $\Gamma = 2\beta^{1h} A^{h,ij} \alpha^{i1} \alpha^{j1}$. The strength of the cubic coupling terms can be found by similar arguments. However, there are two cases that have to be treated separately, case 1: $m_1 = m_2 \neq m_3$ and case 2: $m_1 = m_2 = m_3$.

In the first case the coupling is of the type $k_1 + k_2 - k_2 = k_1$. There are three different combinations of m_2 and m_3 with two corresponding permutations. The combinations are

1. $m_2 = k_2$ and $m_3 = -k_2$ with $|m_2 + m_3|^2 = 0$,
2. $m_2 = k_1$ and $m_3 = k_2$ with $|m_2 + m_3|^2 = 1$,
3. $m_2 = k_1$ and $m_3 = -k_2$ with $|m_2 + m_3|^2 = 3$,

which defines the coefficient $g\kappa$ in Eq. (4.20) to have the value $g\kappa = -2F(0) - 2F(1) - 2F(3)$.

In the second case the coupling is of the type $k_1 + k_1 - k_1 = k_1$. There are three possible permutations with

1. $m_2 = k_1$ and $m_3 = -k_1$ with $|m_2 + m_3|^2 = 0$,

2. $m_2 = -k_1$ and $m_3 = k_1$ with $|m_2 + m_3|^2 = 0$,

3. $m_2 = k_1$ and $m_3 = k_1$ with $|m_2 + m_3|^2 = 4$,

which results in $g = -2F(0) - F(4)$ for Eq. (4.20).

Based on the above reasoning and Eq. (4.32) one may calculate the exact form of the coefficient in Eq. (4.20) with respect to the parameters of the BVAM model of Eq. (4.10). The parameters of the amplitude equations are given by

$$\Gamma = \frac{-2bC\eta R\sqrt{\eta(\eta - 2R)}}{(\eta + b\,\eta - 2R)\sqrt{(\eta + b\eta - 2R)(\eta - R)}}, \tag{A.1}$$

$$g = \frac{3b\eta^2(\eta - 2R)R}{(\eta + b\eta - 2R)^2(\eta - R)}, \tag{A.2}$$

$$\kappa = 2, \tag{A.3}$$

where we have denoted $R = Dk_c^2 = \eta(Db + 1)/2$. The linear coefficient of Eq. (4.20) is given by Eq. (4.19).

Three-dimensional SC-lattice

In the SC-lattice the vectors are independent and given as $\vec{k}_1 = k_c(1, 0, 0)$, $\vec{k}_2 = k_c(0, 1, 0)$ and $\vec{k}_3 = k_c(0, 0, 1)$. There are no resonant modes. Following the ideas above in the first case we find

1. $m_2 = k_2$ and $m_3 = -k_2$ with $|m_2 + m_3|^2 = 0$,

2. $m_2 = k_1$ and $m_3 = k_2$ with $|m_2 + m_3|^2 = 2$,

3. $m_2 = k_1$ and $m_3 = -k_2$ with $|m_2 + m_3|^2 = 2$,

which defines the coefficient $g\kappa = -2F(0) - 4F(2)$ in Eq. (4.20). The second case yields the permutations

1. $m_2 = k_1$ and $m_3 = -k_1$ with $|m_2 + m_3|^2 = 0$,

2. $m_2 = -k_1$ and $m_3 = k_1$ with $|m_2 + m_3|^2 = 0$,

3. $m_2 = k_1$ and $m_3 = k_1$ with $|m_2 + m_3|^2 = 4$,

which gives $g = -2F(0) - F(4)$ for Eq. (4.20).

For the amplitude equations of the three-dimensional SC-lattice (Eq. (4.21)) the coefficients are given by

$$g = \frac{-b\,\eta^2(C^2(8\eta - 23R) - 27R)(\eta - 2R)}{9(\eta + b\eta - 2R)^2(\eta - R)}, \tag{A.4}$$

$$\kappa = \frac{18(C^2(8\eta - 7R) - 3R)}{C^2(8\eta - 23R) - 27R}, \tag{A.5}$$

where we have again denoted $R = Dk_c^2 = \eta(Db+1)/2$ and the linear coefficient of Eq. (4.21) is given by Eq. (4.19).

Three-dimensional FCC-lattice

For the FCC-lattice the vectors of BCC-lattice are given by $\vec{k}_1 = k_c(1,1,1)/\sqrt{3}$, $\vec{k}_2 = k_c(1,1,-1)/\sqrt{3}$, $\vec{k}_3 = k_c(1,-1,1)/\sqrt{3}$ and $\vec{k}_4 = k_c(1,-1,-1)/\sqrt{3}$ are not linearly independent. To find the coefficient of the resonant contribution to Eq. (4.22) one must considers the possible combinations of the two last terms within the sum $k_2 + k_3 - k_4 = k_1$. These are given by

1. $m_2 = k_3$ and $m_3 = -k_4$ with $|m_2 + m_3|^2 = \frac{4}{3}$,
2. $m_2 = -k_4$ and $m_3 = k_2$ with $|m_2 + m_3|^2 = \frac{4}{3}$,
3. $m_2 = k_2$ and $m_3 = k_3$ with $|m_2 + m_3|^2 = \frac{4}{3}$,

which yields the resonant coupling coefficient $\Gamma = 6F(\frac{4}{3})$ for the Eq. (4.22).

The two other coefficients are determined using the same reasoning as above. In the first case one gets

1. $m_2 = k_2$ and $m_3 = -k_2$ with $|m_2 + m_3|^2 = 0$,
2. $m_2 = k_1$ and $m_3 = -k_2$ with $|m_2 + m_3|^2 = \frac{4}{3}$,
3. $m_2 = k_1$ and $m_3 = k_2$ with $|m_2 + m_3|^2 = \frac{8}{3}$,

which results in the coefficient $g\kappa = -2F(0) - 2F(\frac{4}{3}) - 2F(\frac{8}{3})$ for the Eq. (4.22). In the second case we get the permutations

1. $m_2 = k_1$ and $m_3 = -k_1$ with $|m_2 + m_3|^2 = 0$,
2. $m_2 = -k_1$ and $m_3 = k_1$ with $|m_2 + m_3|^2 = 0$,
3. $m_2 = k_1$ and $m_3 = k_1$ with $|m_2 + m_3|^2 = 4$,

which yields $g = -2F(0) - F(4)$ for the Eq. (4.22).

The coefficients of the amplitude equations of the three-dimensional FCC-lattice (Eq. (4.22)) can be written as

$$\Gamma = \frac{6b\eta^2(\eta - 2R)(3C^2(8\eta - 7R) - R)}{(\eta + b\eta - 2R)^2(\eta - R)}, \tag{A.6}$$

$$g = \frac{-b\,\eta^2(C^2(8\eta - 23R) - 27R)(\eta - 2R)}{9(\eta + b\eta - 2R)^2(\eta - R)}, \tag{A.7}$$

$$\kappa = \frac{18(C^2(648\eta - 583R) - 75R)}{25(C^2(8\eta - 23R) - 27R)}, \tag{A.8}$$

where $R = \eta(Db + 1)/2$ and the linear coefficient λ_c of Eq. (4.22) is defined by Eq. (4.19).

Three-dimensional BCC-lattice

For the BCC-lattice the vectors of FCC-lattice are given by $\vec{k}_1 = k_c(1, 1, 0)/\sqrt{2}$, $\vec{k}_2 = k_c(0, 1, 1)/\sqrt{2}$, $\vec{k}_3 = k_c(1, 0, 1)/\sqrt{2}$, $\vec{k}_4 = k_c(1, -1, 0)/\sqrt{2}$, $\vec{k}_5 = k_c(0, 1, -1)/\sqrt{2}$ and $\vec{k}_6 = k_c(1, 0, -1)/\sqrt{2}$. In the BCC-lattice there is both quadratic and cubic resonant coupling of the modes. The quadratic coupling is due to $k_2 + k_6 = k_3 + k_5 = k_1$ with the coupling coefficient $\Upsilon = 2\beta^{1h} A^{h,ij} \alpha^{i1} \alpha^{j1}$. The cubic coupling is due to $k_2 + k_4 + k_5 = k_3 - k_4 + k_6 = k_1$ and defined by

1. $m_2 = k_5$ and $m_3 = k_4$ with $|m_2 + m_3|^2 = 1$,

2. $m_2 = k_2$ and $m_3 = k_4$ with $|m_2 + m_3|^2 = 1$,

3. $m_2 = k_5$ and $m_3 = k_2$ with $|m_2 + m_3|^2 = 2$,

which gives $\Gamma = 2F(2) + 4F(1)$ for the Eq. (4.23). The other coefficients are given by wave vector pairs

1. $m_2 = k_2$ and $m_3 = -k_2$ with $|m_2 + m_3|^2 = 0$,

2. $m_2 = k_1$ and $m_3 = k_3$ with $|m_2 + m_3|^2 = 1$,

3. $m_2 = k_3$ and $m_3 = k_1$ with $|m_2 + m_3|^2 = 3$,

which gives $g\kappa = -2F(0) - 2F(1) - 2F(3)$,

1. $m_2 = k_4$ and $m_3 = -k_4$ with $|m_2 + m_3|^2 = 0$,

2. $m_2 = k_1$ and $m_3 = -k_4$ with $|m_2 + m_3|^2 = 2$,

3. $m_2 = k_1$ and $m_3 = k_4$ with $|m_2 + m_3|^2 = 2$,

which gives $g\chi = -2F(0) - 2F(1) - 2F(3)$, and

1. $m_2 = k_1$ and $m_3 = -k_1$ with $|m_2 + m_3|^2 = 0$,

2. $m_2 = -k_1$ and $m_3 = k_1$ with $|m_2 + m_3|^2 = 0$,

3. $m_2 = k_1$ and $m_3 = k_1$ with $|m_2 + m_3|^2 = 4$,

which gives $g = 2F(0) + F(4)$ for Eq. (4.23). The coefficients of the amplitude equations of the three-dimensional BCC-lattice (Eq. (4.23)) can be written as

$$\Upsilon = \frac{-bC\eta R\sqrt{\eta(\eta-2R)}}{(\eta+b\,\eta-2R)\sqrt{(\eta+b\eta-2R)(\eta-R)}}, \tag{A.9}$$

$$\Gamma = \frac{b\,\eta^2(R(12R-6\eta)+C^2(40\eta^2-118\eta*R+76R^2))}{(\eta+b\eta-2R)^2(\eta-R)}, \tag{A.10}$$

$$g = \frac{-b\eta^2(C^2(8\eta-23R)-27R)(\eta-2R)}{9(\eta+b\eta-2R)^2(\eta-R)}, \tag{A.11}$$

$$g\kappa = \frac{-b\eta^2((6\eta-12R)R-C^2(19\eta^2-58\eta R+40R^2))}{(\eta+b\eta-2R)^2(\eta-R)}, \tag{A.12}$$

$$g\chi = \frac{2b\eta^2(C^2(8\eta-7R)-3R)(\eta-2R)}{(\eta+b\eta-2R)^2(\eta-R)}, \tag{A.13}$$

where $R = \eta(Db+1)/2$ and the linear coefficient λ_c of Eq. (4.23) is defined by Eq. (4.19).

A.2 Details on stability analysis of amplitude equation systems

After one has derived the amplitude equation systems, one can study the stability of patterns with different symmetries by employing linear analysis to the system of amplitude equations around the interesting stationary states. In the following, we will present how this is carried out for the amplitude equation systems for the two-dimensional hexagonal lattice and the three-dimensional SC-, FCC-, and BCC-lattices.

Two-dimensional hexagonal lattice

The system of amplitude equations for a two-dimensional hexagonal lattice can be written based on Eq. (4.20) as

$$\begin{aligned}
\frac{dW_1}{dt} &= \lambda_c W_1 + \Gamma W_2^* W_3^* - g[|W_1|^2 + \kappa(|W_2|^2 + |W_3|^2)]W_1, \\
\frac{dW_2}{dt} &= \lambda_c W_2 + \Gamma W_1^* W_3^* - g[|W_2|^2 + \kappa(|W_1|^2 + |W_3|^2)]W_2, \\
\frac{dW_3}{dt} &= \lambda_c W_3 + \Gamma W_1^* W_2^* - g[|W_3|^2 + \kappa(|W_1|^2 + |W_2|^2)]W_3,
\end{aligned} \tag{A.14}$$

where λ_c is given by Eq. (4.19) and the coefficients Γ, g and κ derived in the appendix A.1 are defined by Eqs. (A.1), (A.2) and (A.3), respectively.

The system of Eq. (A.14) has numerous stationary states. In the case of stripes $W_2 = W_3 = 0$ and the system reduces to only one equation. Now the stationary state defined by the zero of the right-hand side of Eqs. (A.14) can easily be shown to be $W_1^c = \sqrt{\lambda_c/g}e^{i\phi_1}$. For the rhombic patterns ($W_3 = 0$), the stationary state is given by $W_j^c = \sqrt{\lambda_c/(g(1+\kappa))}e^{i\phi_j}$ ($j = 1, 2$). In the case of hexagonally arranged spots we have three equations and by choosing an isotropic solution such that $W_c = W_1^c = W_2^c = W_3^c$ we obtain two stationary states defined by

$$|W_\pm^c| = \frac{|\Gamma| \pm \sqrt{\Gamma^2 + 4\lambda_c g[1+2\kappa]}}{2g(1+2\kappa)}. \tag{A.15}$$

An other non-isotropic stationary solution of hexagonal spots is defined by $W_3^c = |\Gamma|/(g(\kappa+1))$ and $W_1^c = W_2^c = \sqrt{\lambda_c - g|W_3|^2/(g(\kappa+1))}$.

The elements of the linearized amplitude matrix can be calculated based on

Eq. (4.33)) and are given by

$$\begin{aligned}
\left|\frac{\partial f_i}{\partial |W_i|}\right|_{W_c} &= \lambda_c - g\kappa(|W_{i-1}^c|^2 + |W_{i+1}^c|^2) - 3g|W_i^c|^2, \\
\left|\frac{\partial f_i}{\partial |W_{i-1}|}\right|_{W_c} &= \Gamma|W_{i+1}^c| - 2g\kappa\ |W_{i-1}^c|\ |W_i^c|, \\
\left|\frac{\partial f_i}{\partial |W_{i+1}|}\right|_{W_c} &= \Gamma|W_{i-1}^c| - 2g\kappa\ |W_{i+1}^c|\ |W_i^c|, \qquad \text{(A.16)}
\end{aligned}$$

where $i = 1, 2, 3\ (mod\ 3)$ and the partial derivatives are evaluated at the stationary state. Based on these equations one can construct the 3×3 Jacobian matrices for the different symmetries. By substituting the values of the stationary states and coefficients (Eqs. (A.1), (A.2) and (A.3)) to the Jacobians and calculating the eigenvalues, one obtains conditions for the stability of symmetries as a function of the original reaction-diffusion parameters. The parameter values for, which the even one of the eigenvalues is positive, the pattern is unstable. For negative eigenvalues the pattern is stable. The eigenvalues and the bifurcation diagrams are presented in Sec. 4.3.3.

Three-dimensional SC-lattice

The amplitude equations of a three-dimensional SC-lattice are based on Eq. (4.21) and the system is given as

$$\begin{aligned}
\frac{dW_1}{dt} &= \lambda_c W_1 - g[|W_1|^2 + \kappa(|W_2|^2 + |W_3|^2)]W_1, \\
\frac{dW_2}{dt} &= \lambda_c W_2 - g[|W_2|^2 + \kappa(|W_1|^2 + |W_3|^2)]W_2, \\
\frac{dW_3}{dt} &= \lambda_c W_3 - g[|W_3|^2 + \kappa(|W_1|^2 + |W_2|^2)]W_3, \qquad \text{(A.19)}
\end{aligned}$$

where the λ_c, g is defined by Eq. (4.19), and coefficients g and κ are given by Eqs. (A.4) and (A.5) in the appendix A.1.

Next, we will consider only the isotropic stationary states of the amplitude system in Eq. (A.19). The stationary state corresponding to the planar lamellae is given by $|W_1^c| = \sqrt{\lambda_c/g}$. For the cylindrical structure we get $|W_1^c| = |W_2^c| = \sqrt{\lambda_c/(g(\kappa+1))}$ and for the isotropic stationary state of SC-droplets $|W_1^c| = |W_2^c| = |W_3^c| = \sqrt{\lambda_c/(g(2\kappa+1))}$.

For the SC-lattice, the elements of the linearized matrix (Eq. (4.33)) are given by

$$\begin{aligned}
\left|\frac{\partial f_i}{\partial |W_i|}\right|_{W_c} &= \lambda_c - g\kappa(|W_{i-1}^c|^2 + |W_{i+1}^c|^2) - 3g|W_i^c|^2, \\
\left|\frac{\partial f_i}{\partial |W_{i-1}|}\right|_{W_c} &= -2g\kappa\ |W_{i-1}^c|\ |W_i^c|, \\
\left|\frac{\partial f_i}{\partial |W_{i+1}|}\right|_{W_c} &= -2g\kappa\ |W_{i+1}^c|\ |W_i^c|,
\end{aligned} \tag{A.20}$$

where $i = 1, 2, 3\ (mod\ 3)$. By substituting the values of the stationary states and coefficients defined by Eqs. (A.4) and (A.5) to the 3×3 matrix defined above one can study stability of different symmetries. The eigenvalues and the bifurcation diagrams are presented in Sec. 4.3.3.

Three-dimensional FCC-lattice

The amplitude equations of the three-dimensional FCC-lattice are defined by Eq. (4.22) and the system is given by

$$\begin{aligned}
\frac{dW_1}{dt} &= \lambda_c W_1 + \Gamma W_2^* W_3^* W_4^* - g[|W_1|^2 + \kappa(|W_2|^2 + |W_3|^2) + |W_4|^2)]W_1, \\
\frac{dW_2}{dt} &= \lambda_c W_2 + \Gamma W_1^* W_3^* W_4^* - g[|W_2|^2 + \kappa(|W_1|^2 + |W_3|^2) + |W_4|^2)]W_2, \\
\frac{dW_3}{dt} &= \lambda_c W_3 + \Gamma W_1^* W_2^* W_4^* - g[|W_3|^2 + \kappa(|W_1|^2 + |W_2|^2) + |W_4|^2)]W_3, \\
\frac{dW_4}{dt} &= \lambda_c W_4 + \Gamma W_1^* W_2^* W_3^* - g[|W_4|^2 + \kappa(|W_1|^2 + |W_2|^2) + |W_3|^2)]W_4,
\end{aligned} \tag{A.21}$$

where λ_c is given by Eq. (4.19), and the coefficients Γ, g and κ are defined by Eqs. (A.6), (A.7) and (A.8) in the appendix A.1.

We will consider only the isotropic stationary states corresponding to lamellar planes and FCC-droplet structure. The stationary state corresponding to the planar lamellae is defined by $|W_1^c| = \sqrt{\lambda_c/g}$, with $|W_2^c| = |W_3^c| = |W_4^c| = 0$. For the stationary state of FCC-droplets with constraint $|W_1^c| = |W_2^c| = |W_3^c| = |W_4^c|$ we get $|W_i^c| = \sqrt{\lambda_c/(g(3\kappa + 1) - \Gamma)}$.

For the FCC-lattice, the elements of the linearized matrix (Eq. (4.33)) are

defined by

$$\begin{aligned}
\left|\frac{\partial f_i}{\partial |W_i|}\right|_{W_c} &= \lambda_c - g\kappa(|W^c_{i-1}|^2 + |W^c_{i+1}|^2 + |W^c_{i+2}|^2) - 3g|W^c_i|^2, \\
\left|\frac{\partial f_i}{\partial |W_{i-1}|}\right|_{W_c} &= -2g\kappa\ |W^c_{i-1}|\ |W^c_i| + \Gamma|W^c_{i+1}|\ |W^c_{i+2}|, \\
\left|\frac{\partial f_i}{\partial |W_{i+1}|}\right|_{W_c} &= -2g\kappa\ |W^c_{i+1}|\ |W^c_i| + \Gamma|W^c_{i-1}|\ |W^c_{i+2}|, \\
\left|\frac{\partial f_i}{\partial |W_{i+2}|}\right|_{W_c} &= -2g\kappa\ |W^c_{j+1}|\ |W^c_j| + \Gamma|W^c_{i-1}|\ |W^c_{i+1}|,
\end{aligned} \tag{A.22}$$

where $i = 1, 2, 3, 4\ (mod\ 4)$. By substituting the values of the above calculated stationary states and coefficients defined by Eqs. (A.7), (A.6) and (A.8) to the 4×4 matrix defined above one can study stability of different symmetries. The eigenvalues and the bifurcation diagrams are presented in Sec. 4.3.3.

Three-dimensional BCC-lattice

The amplitude equations of a three-dimensional BCC-lattice are defined by Eq. (4.23) and the system is given by

$$\begin{aligned}
\frac{dW_1}{dt} &= \lambda_c W_1 + \Upsilon(W_2W_6 + W_3W_5) + \Gamma(W_2W_4W_5 + W_3W^*_4W_6) - \\
&\quad g[|W_1|^2 + \chi|W_4|^2 + \kappa(|W_2|^2 + |W_3|^2 + |W_5|^2 + |W_6|^2]W_1, \\
\frac{dW_2}{dt} &= \lambda_c W_2 + \Upsilon(W_1W_3 + W_3W_6) + \Gamma(W_3W_5W_6 + W_1W_4W^*_5) - \\
&\quad g[|W_2|^2 + \chi|W_5|^2 + \kappa(|W_1|^2 + |W_3|^2 + |W_4|^2 + |W_6|^2]W_2, \\
\frac{dW_3}{dt} &= \lambda_c W_3 + \Upsilon(W_2W_4 + W_1W_5) + \Gamma(W_1W_4W_6 + W_2W_5W^*_6) - \\
&\quad g[|W_3|^2 + \chi|W_6|^2 + \kappa(|W_1|^2 + |W_2|^2 + |W_4|^2 + |W_5|^2]W_3, \\
\frac{dW_4}{dt} &= \lambda_c W_4 + \Upsilon(W_3W_5 + W_2W_6) + \Gamma(W_1W_2W_5 + W^*_1W_3W_6) - \\
&\quad g[|W_4|^2 + \chi|W_1|^2 + \kappa(|W_2|^2 + |W_3|^2 + |W_5|^2 + |W_6|^2]W_4, \\
\frac{dW_5}{dt} &= \lambda_c W_5 + \Upsilon(W_4W_6 + W_1W_3) + \Gamma(W_2W_3W_6 + W_1W^*_2W_4) - \\
&\quad g[|W_5|^2 + \chi|W_2|^2 + \kappa(|W_6|^2 + |W_1|^2 + |W_3|^2 + |W_4|^2]W_5, \\
\frac{dW_6}{dt} &= \lambda_c W_6 + \Upsilon(W_1W_5 + W_2W_4) + \Gamma(W_1W_3W_4 + W_2W^*_3W_5) - \\
&\quad g[|W_6|^2 + \chi|W_3|^2 + \kappa(|W_1|^2 + |W_2|^2 + |W_4|^2 + |W_5|^2]W_6,
\end{aligned} \tag{A.23}$$

where the λ_c is defined by Eq. (4.19) and the coefficients Υ, Γ, g, χ and κ are given by Eqs. (A.9), (A.10), (A.11), (A.13), and (A.12) in the Appendix A.1.

Again we will consider only the two most important cases, namely planar lamellae and isotropic BCC-droplets. The stationary state corresponding to planar lamellae is defined by $|W_1^c| = \sqrt{\lambda_c/g}$, with $|W_2^c| = |W_3^c| = |W_4^c| = |W_5^c| = |W_6^c| = 0$. For the stationary state of BCC-droplets with constraint $|W_1^c| = |W_2^c| = |W_3^c| = |W_4^c| = |W_5^c| = |W_6^c|$ we get

$$|W_i^c| = \frac{-2\Upsilon \pm \sqrt{4\Upsilon^2 + 4\lambda_c(g(1+\chi+4\kappa) - 2\Gamma)}}{2(g(1+\chi+4\kappa))}. \tag{A.24}$$

For the BCC-lattice, the elements of the linearized matrix (Eq. (4.33)) are defined as

$$\begin{aligned}
\left|\frac{\partial f_i}{\partial |W_i|}\right|_{W_c} &= \lambda_c - g\kappa(|W_{i+1}^c|^2 + |W_{i+2}^c|^2 + |W_{i+4}^c|^2 + |W_{i+5}^c|^2) - \\
&\quad g\chi|W_{i+3}^c| - 3g|W_i^c|^2, \\
\left|\frac{\partial f_i}{\partial |W_{i+1}|}\right|_{W_c} &= -2g\kappa\ |W_{i+1}^c|\,|W_i^c| + \Gamma|W_{i+3}^c|\,|W_{i+4}^c| + \Upsilon|W_{i+5}^c|, \\
\left|\frac{\partial f_i}{\partial |W_{i+2}|}\right|_{W_c} &= -2g\kappa\ |W_{i+2}^c|\,|W_i^c| + \Gamma|W_{i+3}^c|\,|W_{i+5}^c| + \Upsilon|W_{i+4}^c|, \\
\left|\frac{\partial f_i}{\partial |W_{i+3}|}\right|_{W_c} &= -2g\chi\ |W_{i+3}^c|\,|W_i^c| + \Gamma(|W_{i+1}^c|\,|W_{i+4}^c| + |W_{i+2}^c|\,|W_{i+5}^c|), \\
\left|\frac{\partial f_i}{\partial |W_{i+4}|}\right|_{W_c} &= -2g\kappa\ |W_{i+3}^c|\,|W_i^c| + \Gamma|W_{i+1}^c|\,|W_{i+3}^c| + \Upsilon|W_{i+2}^c|, \\
\left|\frac{\partial f_i}{\partial |W_{i+5}|}\right|_{W_c} &= -2g\kappa\ |W_{i+5}^c|\,|W_i^c| + \Gamma|W_{i+2}^c|\,|W_{i+3}^c| + \Upsilon|W_{i+1}^c|,
\end{aligned} \tag{A.25}$$

where $i = 1, 2, 3, 4, 5, 6$ $(mod\ 6)$. By substituting the values of the stationary states and coefficients defined by Eqs. (A.9), (A.10), (A.11), (A.13), and (A.12) to the 6×6 matrix defined above one can study stability of different symmetries. The eigenvalues and the bifurcation diagrams are presented in Sec. 4.3.3.

A.3 Details on discretization and numerical simulations

In the case of a Turing system in two dimensions we have to discretize equations of the following form

$$\begin{cases} y_t = D\Delta y + f(x_1, x_2, t) & \text{in } \Omega = [0, L_x] \times [0, L_y] \\ y(x_1, 0, t) = y(x_1, L_y, t) \\ y(0, x_2, t) = y(L_x, x_2, t) \\ y(x_1, x_2, 0) = g(x_1, x_2), \end{cases} \tag{A.26}$$

where the topmost equation defines the problem and the domain where has to be solved. The next two equations express the periodic boundary conditions, and the last equation fixes the initial conditions with help of function $g(x_1, x_2)$ defined on the domain. In the case of Turing systems the function g is usually replaced by an homogeneous distribution of random numbers rather than a function in the usual sense.

For simplicity the lattice constant (h or dx) is chosen to be isotropic, i.e., $h = h_1 = h_2$. Now the notation y_{ij} is used for the approximation of $y(ih_1, jh_2, t)$, the value of y at the lattice site (i, j) at time t. Using this, we get the matrix

$$y_h(t) = \begin{pmatrix} y_{11} & \dots & y_{1L_y} \\ \vdots & \ddots & \vdots \\ y_{L_x 1} & \dots & y_{L_x L_y} \end{pmatrix}.$$

Next we discretize the function f over the domain matrix by setting

$$f_h(t) = \begin{pmatrix} f(h, h, t) & \dots & f(h, L_y h, t) \\ \vdots & \ddots & \vdots \\ f(L_x h, h, t) & \dots & f(L_x h, L_y h, t) \end{pmatrix}.$$

and the initial conditions analogously

$$g_h(t) = \begin{pmatrix} g(h, h, t) & \dots & g(h, L_y h, t) \\ \vdots & \ddots & \vdots \\ g(L_x h, h, t) & \dots & g(L_x h, L_y h, t) \end{pmatrix}.$$

Using these matrix notations we may formulate the Euler method, which is well-known and simple method for solving differential equations citepharris98a. The method is based on numerical integration of differential equations. In our case, we use it for the integration over the time step.

In the general case, Euler method is used for solving simple first order differential equation of the form $y'(t) = f(t, y(t))$. As the derivative y' is approximated by a difference quotient, we obtain the equation

$$y(t_i + \delta) - y(t_i) = f(t_i, y(t_i)) \cdot \delta + o(\delta^2), \tag{A.27}$$

where $o(\delta^2)$ is an error term of the second order, such that

$$\lim_{\delta \to 0} \frac{o(\delta^2)}{\delta} = 0.$$

By dropping the error term, Eq. (A.27) can be further reduced to

$$y(t_i + \delta) \approx y(t_i) + f(t_i, y(t_i)) \cdot \delta. \tag{A.28}$$

In our discrete Turing system the time step is given by δ (or dt). By setting $y_h^k = y_h(k\delta)$, we obtain for Euler method

$$\begin{cases} y_h^{k+1} = y_h^k + \delta(D\Delta_h y_h^k + f_h^k) \\ y_h^0 = g_h, \end{cases} \tag{A.29}$$

where Δ_h denotes the discretized Laplacian. In our two-dimensional study, the discretized Laplacian of the function $y(x_1, x_2)$ can be written out as follows

$$\Delta y = \frac{\partial^2 y}{\partial x_1^2} + \frac{\partial^2 y}{\partial x_2^2}. \tag{A.30}$$

In the three-dimensional case, the operator would contain second derivative also in the third direction. By approximating the derivatives twice in the same way as in the previous section and using the notation $y_{i,j}$ for $y(hi, hj)$ we obtain

$$\frac{\partial^2 y}{\partial x_1^2} \approx \frac{y_{i+1,j} - 2y_{i,j} + y_{i-1,j}}{h^2}. \tag{A.31}$$

By repeating the above procedure for derivatives with respect to y, we can write the discretized Laplacian operator for Eq. (A.29) as $\Delta_h = I \otimes \Delta_{h_1} + \Delta_{h_2} \otimes I$, where

$$\Delta_{h_p} = \frac{1}{h_p^2} \begin{pmatrix} -2 & 1 & \dots & 0 & 1 \\ 1 & -2 & \dots & 0 & 0 \\ \vdots & \ddots & \ddots & \ddots & \vdots \\ 0 & \dots & 1 & -2 & 1 \\ 1 & \dots & 0 & 1 & -2 \end{pmatrix}.$$

for $p = 1, 2$. Notice that periodic boundary conditions are properly taken into account in this formulation.

Appropriate values for the discretization parameters $dx = h$ and $dt = \delta$ can be found by using the von Neumann stability analysis (Press et al., 1995). In three dimensions the discretized difference equation would be given by

$$\begin{aligned} \frac{y_{mnp}^{t+1} - y_{mnp}^t}{\delta} &= \frac{D}{h^2}(y_{m+1,n,p} + y_{m-1,n,p} + y_{m,n+1,p} + y_{m,n-1,p} + y_{m,n,p+1} + \\ &\quad + y_{m,n,p-1} - 6y_{mnp}) + f_{mnp}^t(y), \end{aligned} \tag{A.32}$$

where h denotes the lattice constant and δ the time step.

Let us now consider that the difference equation varies so slowly that we can try independent solutions of the form

$$y^t_{m,n,p} = \xi^t e^{ik_x mh} e^{ik_y nh} e^{ik_z ph}, \tag{A.33}$$

where i is the imaginary unit, and k_x, k_y and k_z the wave numbers in x-, y- and z-directions, respectively. When we substitute Eq. (A.33) to Eq. (A.32) and simplify we get

$$\xi = \frac{D\delta}{h^2}(e^{ik_x h}+e^{-ik_x h}+e^{ik_y h}+e^{-ik_y h}+e^{ik_z h}+e^{-ik_z h}-6)+1+\frac{\delta f^t_h(y)}{\xi^n(e^{mk_x}e^{nk_y}e^{pk_z})^{ih}}, \tag{A.34}$$

We can further approximate $\xi(k)$ by transforming complex numbers to trigonometric functions using Euler formula and by approximating the cosines with minus one. This yields

$$|\xi(k)| \leq \left|1 - \frac{12D\delta}{h^2} + \frac{\delta f^t_h(y)}{\xi^n(e^{mk_x}e^{nk_y}e^{pk_z})^{ih}}\right|, \tag{A.35}$$

We are interested in the modulus of ξ, which is called the *amplification factor*. Condition $|\xi(k)| < 1$ for all k, implies that the difference equation is stable, i.e., no mode is exponentially growing. The last term on the right side of Eq. (A.35) is dependent on the reaction kinetics of the BVAM model given by

$$\begin{aligned} f(u,v) &= \eta(u + av - Cuv - uv^2), \\ g(u,v) &= \eta(bv + hu + Cuv + uv^2), \end{aligned} \tag{A.36}$$

As we linearize the above equations, we are left with $f(u,v) = \eta(u + av)$ and $g(u,v) = \eta(bv + hu)$. To make the approximation reasonable we use the same trial solution for both u and v in the form of Eq. (A.33), except that we make a phase shift of π radians between u and v. This is due to the fact that the activator and inhibitor are in anti-phase. Substitution of the linearized kinetics to Eq. (A.35) and simplifying yields

$$\begin{aligned} \max|\xi_u(k)| &= |1 - \delta_u(\frac{12D}{h^2} - \eta(1+a))| \\ \max|\xi_v(k)| &= |1 - \delta_v(\frac{12}{h^2} - \eta(b+h))|. \end{aligned} \tag{A.37}$$

The suitable values of δ are the ones where $\max|\xi(\delta)|$ is below the unity. For two-dimensional systems the conditions are also given by an equation similar to Eq. A.37 with the difference that the constant is 8 instead of 12. Fixing the lattice constant to $h = 1$ and using the parameter values corresponding to the modes

$k_c = 0.45$ and $k_c = 0.86$ (see Sec. 4.2) yields the condition $\delta < 0.225$ for two-dimensional and $\delta < 0.155$ for three-dimensional systems. In practise also the nonlinear effects and the coupling of the equations stabilizes the iteration. Based on this analysis and some trial simulations we found the parameter values $h = 1$ and $\delta = 0.05$ suitable for the BVAM model.

The simulation programs were built using the C programming language. The FFTW library (see http://www.fftw.org) was used in the calculation of the Fourier transform. The random numbers needed for the initial configurations and random noise were generated using RANMAR. The visualization of two-dimensional data was the easiest to carry out by using the surface plots of Matlab. The visualization of three-dimensional data was first carried out using FUNCS (the figures with a black background, e.g. Fig. 5.3) developed by a Finnish company Centre for Scientific Computing (CSC). Most of the three-dimensional data, however, was visualized using a more advanced program named OpenDX, which is an open source visualization environment originally developed by IBM (see www.opendx.org).

References

Agladze, K., Dulos, E., and Kepper, P. D. (1992). Turing patterns in confined gel and gel-free media. *J. Phys. Chem.*, 96:2400.

Ammelt, E., Astrov, Y. A., and Purwins, H.-G. (1998). Hexagon structures in a two-dimensional dc-driven gas discharge system. *Phys. Rev. E*, 58:7109.

Aragon, J. L., Torres, M., Gil, D., Barrio, R. A., and Maini, P. K. (2002). Turing patterns with pentagonal symmetry. *Phys. Rev. E*, 65:051913.

Aranson, I. S., Bishop, A., and Kramer, L. (1998). The dynamics of vortex lines in the three-dimensional complex Ginzburg-Landau equation: instability, stretching, entanglement, and helices. *Phys. Rev. E*, 57:5276.

Aranson, I. S. and Kramer, L. (2002). The world of the complex Ginzburg-Landau equation. *Rev. Mod. Phys.*, 74:2002.

Ashcroft, N. W. and Mermin, N. D. (1976). *Solid State Physics*. Harcourt Brace College Publishers, USA.

Astrov, Y., Ammelt, E., Teperick, S., and Purwins, H.-G. (1996). Hexagon and stripe Turing structures in a gas discharge system. *Phys. Lett. A*, 211:184.

Bak, P., Tang, C., and Wiesenfeld, K. (1987). Self-organized criticality: An explanation of 1/f noise. *Phys. Rev. Lett.*, 59:381.

Ball, P. (2001). *The self-made tapestry: pattern formation in nature*. Oxford Univ. Press, Oxford.

Barenblatt, G. I. (1987). *Dimensional Analysis*. Gordon and Breach Science Publishers, New York.

Barrio, R. A., Aragón, J. L., Torres, M., and Maini, P. K. (2002). Size-dependent symmetry-breaking in models for morphogenesis. *Physica D*, 168-169:61.

Barrio, R. A., Aragon, J. L., Varea, C., Torres, M., Jimenez, I., and de Espinosa, F. M. (1997). Robust symmetric patterns in the Faraday experiment. *Phys. Rev. E*, 56:4222.

Barrio, R. A., Varea, C., Aragón, J. L., and Maini, P. K. (1999). Two-dimensional numerical study of spatial pattern formation in interacting Turing systems. *Bull. Math. Biol.*, 61:483.

Berenstein, I., Yang, L., Dolnik, M., Zhabotinsky, A. M., and Epstein, I. R. (2003). Superlattice Turing structures in a photosensitive reaction-diffusion system. *Phys. Rev. Lett.*, 91:058302.

Boissonade, J., Dulos, E., and Kepper, P. D. (1995). Turing patterns: From myth to reality. *in Chemical Waves and Patterns (Eds. R. Kapral and K. Showalter)*, Chapter 7:221–268.

Borckmans, P., Dewel, G., Wit, A. D., Dulos, E., Boissonade, J., Gauffre, F., and Kepper, P. D. (2002). Diffusive instabilities and chemical reactions. *Int. J. Bif. Chaos*, 12:2307.

Borckmans, P., Wit, A. D., and Dewel, G. (1992). Competition in ramped Turing structures. *Physica A*, 188:137.

Bose, I. and Chaudhuri, I. (1997). Effect of randomness and anisotropy on Turing patterns in reaction-diffusion systems. *Phys. Rev. E*, 55:5291.

Callahan, T. K. (2003). Hopf bifurcations on cubic lattices. *Nonlinearity*, 16:2099.

Callahan, T. K. (2004). Turing patterns with o(3) symmetry. *Physica D*, 188:65.

Callahan, T. K. and Knobloch, E. (1996). Bifurcations on the fcc lattice. *Phys. Rev. E*, 53:3559.

Callahan, T. K. and Knobloch, E. (1997). Symmetry-breaking bifurcations on cubic lattices. *Nonlinearity*, 10:1179.

Callahan, T. K. and Knobloch, E. (1999). Pattern formation in three-dimensional reaction-diffusion systems. *Physica D*, 132:339.

Callahan, T. K. and Knobloch, E. (2001). Long-wavelength instabilities of three-dimensional patterns. *Phys. Rev. E*, 64:36214.

Cartwright, J. H. E. (2002). Labyrinthine Turing pattern formation in the cerebral cortex. *J. Theor. Biol.*, 217:97.

Castets, V., Dulos, E., Boissonade, J., and Kepper, P. D. (1990). Experimental evidence of a sustained standing Turing-type nonequilibrium chemical pattern. *Phys. Rev. Lett.*, 64:2953.

Chaikin, P. M. and Lubensky, T. C. (1995). *Principles of condensed matter physics*. Cambridge University Press, Cambridge.

Chen, Y. and Schier, A. F. (2001). The zebrafish nodal signal squint functions as a morphogen. *Nature*, 411:607, see also ibid. p.533.

Crawford, J. D. (1991). Introduction to bifurcation theory. *Rev. Mod. Phys.*, 63:991.

Cross, M. C. and Hohenberg, P. C. (1993). Pattern formation outside of equilibrium. *Rev. Mod. Phys.*, 65:851.

De Groot, S. R. and Mazur, P. (1962). *Non-equilibrium Thermodynamics*. North Holland, Amsterdam.

De Kepper, P., Dulos, E., Boissonade, J., Wit, A. D., Dewel, G., and Borckmans, P. (2000). Reaction-diffusion patterns in confined chemical systems. *J. Stat. Phys.*, 101:495.

De Wit, A. (1993). *Brisure de symétrie spatiale et dynamique spatio-temporelle dans les systèmes réaction-diffusion (in French)*. Ph.D. thesis, Université Libre de Bruxelles.

De Wit, A. (1999). Spatial patterns and spatio-temporal dynamics in chemical systems. *Adv. Chem. Phys.*, 109:435.

De Wit, A., Borckmans, P., and Dewel, G. (1997). Twist grain boundaries in three-dimensional lamellar Turing structures. *Proc. Nat. Acad. Sci.*, 94:12765.

De Wit, A., Dewel, G., Borckmans, P., and Walgraef, D. (1992). Three-dimensional dissipative structures in reaction-diffusion systems. *Physica D*, 61:289.

De Wit, A., Lima, D., Dewel, G., and Borckmans, P. (1996). Spatiotemporal dynamics near a codimension-two point. *Phys. Rev. E*, 54:261.

Dewel, G., Borckmans, P., Wit, A. D., Rudovics, B., Perraud, J.-J., Dulos, E., Boissonade, J., and Kepper, P. D. (1995). Pattern selection and localized structures in reaction-diffusion systems. *Physica A*, 213:181.

Dewel, G., Wit, A. D., Métens, S., Verdasca, J., and Borckmans, P. (1996). Pattern selection in reaction-diffusion systems with competing bifurcations. *Physica Scripta*, T67:51.

Dionne, B., Silber, M., and Skeldon, A. C. (1997). Stability results for steady, spatially periodic planforms. *Nonlinearity*, 10:321.

Dolnik, M., Berenstein, I., Zhabotinsky, A. M., and Epstein, I. R. (2001a). Spatial periodic forcing of Turing structures. *Phys. Rev. Lett.*, 87:238301.

Dolnik, M., Zhabotinsky, A. M., and Epstein, I. R. (2001b). Resonant suppression of Turing patterns by periodic illumination. *Phys. Rev. E*, 63:026101.

Dufiet, V. and Boissonade, J. (1991). Conventional and unconventional Turing patterns. *J. Chem. Phys.*, 96:664.

Dufiet, V. and Boissonade, J. (1992). Numerical studies of Turing patterns selection in a two-dimensional system. *Physica A*, 188:158.

Dufiet, V. and Boissonade, J. (1996). Dynamics of Turing pattern monolayers close to onset. *Phys. Rev. E*, 53:4883.

Dulos, E., Davies, P., Rudovics, B., and Kepper, P. D. (1996). From quasi-2d to 3d Turing patterns in ramped systems. *Physica D*, 98:53.

Elder, K. R., Viñals, J., and Grant, M. (1992). Dynamic scaling and quasiordered states in the two-dimensional swift-hohenberg equation. *Phys. Rev. A*, 46:7618.

Epstein, I. R., Lengyel, I., S. Kadar, M. K., and Yokoyama, M. (1992). New systems for pattern formation studies. *Physica A*, 188:26.

Epstein, I. R. and Showalter, K. (1996). Nonlinear chemical dynamics: Oscillations, patterns and chaos. *J. Phys. Chem.*, 100:13132.

Falta, J., Imbihl, R., and Henzler, M. (1990). Spatial pattern formation in a catalytic surface reaction: The facetting of Pt(110) in CO+O2. *Phys. Rev. Lett.*, 64:1409.

Field, R. J., Körös, E., and Noyes, R. M. (1972). Oscillations in chemical systems. II. thorough analysis of temporal oscillation in the bromate-cerium-malonic acid system. *J. Am. Chem. Soc.*, 94:8649.

Field, R. J. and Noyes, R. M. (1974). Oscillations in chemical systems. IV. limit cycle behavior in a model of a real chemical reaction. *J. Chem. Phys.*, 60:1877.

Ganapathisubramanian, N. and Showalter, K. (1983). Critical slowing down in the bistable iodate-arsenic(III) reaction. *J. Phys. Chem.*, 87:1098.

Gatenby, R. A. and Maini, P. K. (2003). Cancer summed up. *Nature*, 421:321.

Gierer, A. and Meinhardt, H. (1972). A theory of biological pattern formation. *Kybernetik*, 12:30.

Gollub, J. P. and Langer, J. S. (1999). Pattern formation in nonequilibrium physics. *Rev. Mod. Phys.*, 71:S396.

Gray, P. and Scott, S. K. (1983). Autocatalytic reactions in the isothermal continuous stirred tank reactor - isolas and other forms of multistability. *Chem. Eng. Sci.*, 38:29.

Gray, P. and Scott, S. K. (1984). Autocatalytic reactions in the isothermal continuous stirred tank reactor - oscillations and instabilities in the system $a + 2b \rightarrow 3b$; $b \rightarrow c$. *Chem. Eng. Sci.*, 39:1087.

Gray, P. and Scott, S. K. (1985). Sustained oscillations and other exotic patterns of behavior in isothermal reactions. *J. Phys. Chem.*, 89:22.

Groot, R. D. and Madden, T. J. (1998). Dynamic simulation of diblock copolymer microphase separation. *J. Chem. Phys.*, 108:8713.

Groot, R. D., Madden, T. J., and Tildesley, D. J. (1999). On the role of hydrodynamic interactions in block copolymer microphase separation. *J. Chem. Phys.*, 110:9739.

Gunaratne, G. (1994). Pattern formation in the presence of symmetries. *Phys. Rev. E*, 50:2802.

Gyllenberg, M. (2004). Private communication.

Hagberg, A. and Meron, E. (1997). The dynamics of curved fronts: Beyond geometry. *Phys. Rev. Lett.*, 78:1166.

Haken, H. (1977). *Synergetics, An Introduction*. Springer-Verlag, Berlin.

Harris, J. W. and Stocker, K. (1998). *Handbook of Mathematics and Computational Science*. Springer, Berlin.

Hasslacher, B., Kapral, R., and Lawniczak, A. (1993). Molecular Turing structures in the biochemistry of the cell. *Chaos*, 3:7.

Horváth, A. K., Dolnik, M., nuzuri, A. P. M., and Epstein, I. R. (1999). Control of Turing structures by periodic illumination. *Phys. Rev. Lett.*, 83:2950.

Hoshen, J. and Kopelman, R. (1976). Percolation and cluster distribution. Cluster multiple labeling technique and critical concentration algorithm. *Phys. Rev. B*, 14:3438.

Howard, M. and Rutenberg, A. D. (2003). Pattern formation inside bacteria: fluctuations due to the low copy number of proteins. *Phys. Rev. Lett.*, 90:128102.

Howard, M., Rutenberg, A. D., and de Vet, S. (2001). Dynamic compartmentalization of bacteria: accurate division in e. coli. *Phys. Rev. Lett.*, 87:278102.

Hunding, A. (1980). Dissipative structures in reaction-diffusion systems: Numerical determination of bifurcations in the sphere. *J. Chem. Phys.*, 72:5241.

Hunding, A. and Engelhardt, R. (1995). Early biological morphogenesis and nonlinear dynamics. *J. Theor. Biol.*, 173:401.

Hutson, M. S., Tokutake, Y., Chang, M.-S., Bloor, J. W., Venakides, S., Kiehart, D. P., and Edwards, G. S. (2003). Forces for morphogenesis investigated with laser microsurgery and quantitative modeling. *Science*, 300:145.

Ipsen, M., Kramer, L., and Sorensen, P. (2000). Amplitude equations for description of chemical reaction-diffusion systems. *Phys. Rep.*, 337:193.

Jensen, O., Pannbacker, V. O., Dewel, G., and Borckmans, P. (1993). Subcritical transitions to Turing structures. *Phys. Lett. A*, 179:91.

Judd, S. L. and Silber, M. (2000). Simple and superlattice Turing patterns in reaction-diffusion systems: Bifurcation, bistability and parameter collapse. *Physica D*, 136:45.

Kapral, R. (1995). Pattern formation in chemical systems. *Physica D*, 86:149.

Kapral, R. and Showalter, K. (1995). *Chemical Waves and Patterns*. Kluwer Academic Publishers, Dordrecht.

Karttunen, M., Haataja, M., Elder, K. R., and Grant, M. (1999). Defects, order and hysteresis in driven charge-density waves. *Phys. Rev. Lett.*, 83:3518.

Karttunen, M., Provatas, N., Ala-Nissila, T., and Grant, M. (1998). Nucleation, growth and scaling in slow combustion. *J. Stat. Phys.*, 90:1401.

Koch, A. J. and Meinhardt, H. (1994). Biological pattern formation: From basic mechanisms to complex structures. *Rev. Mod. Phys.*, 66:1481.

Kondo, S. and Asai, R. (1995). A reaction-diffusion wave on the skin of the marine angelfish pomacanthus. *Nature*, 376:678.

Kreyszig, E. (1993). *Advanced Engineering Mathematics*. Wiley, USA.

Krstic, R. (1997). *Human Microscopic Anatomy*. Springer-Verlag, Berlin.

Landauer, R. (1975). Inadequancy of entropy and entropy derivatives in characterizing the steady state. *Phys. Rev. A*, 12:636.

Lengyel, I. and Epstein, I. R. (1991). Modeling of Turing structures in the chlorite-iodine-malonic acid-starch reaction system. *Science*, 251:650.

Lengyel, I. and Epstein, I. R. (1992). A chemical approach to designing Turing patterns in reaction-diffusion systems. *Proc. Nat. Acad. Sci.*, 89:3977.

Lengyel, I. and Epstein, I. R. (1995). The chemistry behind the first experimental chemical examples of Turing patterns. *in Chemical Waves and Patterns (Eds. R. Kapral and K. Showalter)*, Chapter 9:297–322.

Lengyel, I., Li, J., and Epstein, I. R. (1992). Dynamical study of the chlorine dioxide-iodide open system oscillator. *J. Phys. Chem.*, 96:7032.

Lengyel, I., Li, J., Kustin, K., and Epstein, I. R. (1996). Rate constants for reactions between iodine- and chlorine-containing species: A detailed mechanism of the chlorine dioxide/chlorite-iodide reaction. *J. Am. Chem. Soc.*, 118:3708.

Lengyel, I., Rabai, G., and Epstein, I. R. (1990a). Batch oscillation in the reaction of chlorine dioxide with iodine and malonic acid. *J. Am. Chem. Soc.*, 112:4606.

Lengyel, I., Rabai, G., and Epstein, I. R. (1990b). Experimental and modeling study of oscillations in the chlorine dioxide-iodine-malonic acid reaction. *J. Am. Chem. Soc.*, 112:9104.

Leppänen, T. (2001). *Spatial pattern formation in Turing systems*. M.Sc. thesis, Helsinki University of Technology.

Leppänen, T., Karttunen, M., Kaski, K., Barrio, R. A., and Zhang, L. (2002). A new dimension to Turing patterns. *Physica D*, 168-169:35.

Leppänen, T. (2004). The theory of Turing pattern formation. *Current Topics in Physics (Eds. K. Kaski and R.A. Barrio), (Imperial College Press)*, in press.

Leppänen, T., Karttunen, M., Barrio, R. A., and Kaski, K. (2003a). The effect of noise to Turing patterns. *Prog. Theor. Phys. (Suppl.)*, 150:367.

Leppänen, T., Karttunen, M., Barrio, R. A., and Kaski, K. (2004a). Turing systems as models of complex pattern formation. *Braz. J. Phys.*, 34:368.

Leppänen, T., Karttunen, M., Kaski, K., and Barrio, R. A. (2003b). Dimensionality effects in Turing pattern formation. *Int. J. Mod. Phys. B*, 17:5541.

Leppänen, T., Karttunen, M., Kaski, K., and Barrio, R. A. (2004b). Morphological transitions and bistability in Turing systems. *To appear in Phys. Rev. E*, 70.

Leppänen, T., Karttunen, M., Kaski, K., and Barrio, R. A. (2004c). Spatio-temporal pattern formation in a Turing model. *Submitted to InterJournal*.

Liaw, S. S., Yang, C. C., Liu, R. T., and Hong, J. T. (2002). Turing model for the patterns of lady beetles. *Phys. Rev. E*, 64:041909.

Liehr, A. W., Bode, M., , and Purwins, H.-G. (2001). The generation of dissipative quasi-particles near Turing's bifurcation in three-dimensional reaction-diffusion systems. *in High Performance Computing in Science and Engineering (Ed. S. Wagner)*, p. 425.

Logvin, Y. A., Ackemann, T., and Lange, W. (1997). Winking hexagons. *Eur. Phys. Lett.*, 38:583.

Madzvamuse, A. (2000). *A numerical approach to the study of spatial pattern formation*. Ph.D. thesis, University of Oxford.

Madzvamuse, A., Wathen, A. J., and Maini, P. K. (2003). A moving grid finite element method applied to a model biological pattern generator. *J. Comp. Phys.*, 190:478.

Maini, P. K. (2003). How the mouse got its stripes. *Proc. Nat. Acad. Sci.*, 100:9656.

Manneville, P. (1990). *Dissipative Structures and Weak Turbulence*. Academic Press, USA.

Matsen, M. W. and Bates, F. S. (1996). Unifying weak- and strong-segregation block copolymer theories. *Macromolecules*, 29:1091.

Meinhardt, H. (1982). *Models of Biological Pattern Formation*. Academic, New York.

Melo, F., Umbanhowar, P. B., and Swinney, H. L. (1995). Hexagons, kinks and disorder in oscillated granular layers. *Phys. Rev. Lett.*, 75:3838.

Metens, S., Dewel, G., Borckmans, P., and Engelhardt, R. (1997). Pattern selection in bistable systems. *Eur. Phys. Lett.*, 37:109.

Mimura, M., Sakaguchi, H., and Matsushita, M. (2000). Reaction-diffusion modelling of bacterial colony patterns. *Physica A*, 282:283.

Mosekilde, E. and Mouritsen, O. G. (1995). *Modelling the Dynamics of Biological Systems*. Springer-Verlag, Berlin.

Murray, J. D. (1988). How the leopard gets its spots. *Scientific American*, March:62.

Murray, J. D. (1989). *Mathematical Biology*. Springer-Verlag, Berlin.

Murray, J. D. (2003). *Mathematical Biology II: Spatial Models and Biomedical Applications*. Springer-Verlag, Berlin.

Nagorcka, B. N. (1989). Wavelike isomorphic prepatterns in development. *J. Theor. Biol.*, 137:127.

Nagorcka, B. N. and Mooney, J. R. (1985). From stripes to spots: Prepatterns which can be produced in the skin by a reaction-diffusion system. *IMA J. Math. Appl. Med. Biol.*, 114:243.

Newell, A. C., Passot, T., and Lega, J. (1993). Order parameter equations for patterns. *Annu. Rev. Fluid Mech.*, 25:399.

Nicolis, G. (1995). *Introduction to nonlinear science*. Cambridge University Press, Cambridge.

Nicolis, G. and Prigogine, I. (1977). *Self-Organisation in Non-Equilibrium Chemical Systems*. Wiley, New York.

Noszticzius, Z., Ouyang, Q., McCormick, W. D., and Swinney, H. L. (1992). Effect of Turing pattern indicators on CIMA oscillators. *J. Phys. Chem.*, 96:6302.

Ouyang, Q., Noszticzius, Z., and Swinney, H. L. (1992). Spatial bistability of two-dimensional Turing patterns in a reaction-diffusion system. *J. Phys. Chem.*, 96:6773.

Ouyang, Q. and Swinney, H. L. (1991). Transition from a uniform state to hexagonal and striped Turing patterns. *Nature*, 352:610.

Painter, K. J., Maini, P. K., and Othmer, H. G. (1999). Stripe formation in juvenile pomacanthus explained by a generalized Turing mechanism with chemotaxis. *Proc. Nat. Acad. Sci.*, 96:5549.

Patriarca, M. and Leppänen, T. (2004). Modeling language competition. *Physica A*, 338:296.

Pearson, J. E. (1993). Complex patterns in a simple system. *Science*, 261:189. See also http://www.cacr.caltech.edu/ismap/image.html.

Pena, B., Pérez-Garcia, C., Sanz-Anchelergues, A., Miguez, D. G., and Munuzuri, A. P. (2003). Transverse instabilities in chemical Turing patterns of stripes. *Phys. Rev. E*, 68:56206.

Perraud, J. J., Agladze, K., Dulos, E., and Kepper, P. D. (1992). Stationary Turing patterns versus time-dependent structures in the chlorite-iodide-malonic acid reaction. *Physica A*, 188:1.

Petrov, V., Ouyang, Q., and Swinney, H. L. (1997). Resonant pattern formation in a chemical system. *Nature*, 388:655.

Pismen, L. M. (1980). Pattern selection at the bifurcation point. *J. Chem. Phys.*, 72:1900.

Pismen, L. M. (1994). Long-scale deformations of resonant three-dimensional patterns and the structure of confined dislocations. *Phys. Rev. E*, 50:4896.

Press, W. H., Teukolsky, S. A., Vetterling, W. T., and Flannery, B. P. (1995). *Numerical Recipes in C*. Cambridge University Press, Cambridge.

Prigogine, I. and Lefever, R. (1968). Symmetry breaking instabilities in dissipative systems. ii. *J. Chem. Phys.*, 48:1695.

Rabinovich, M. I., Ezersky, A. B., and Weidman, P. D. (2000). *The dynamics of patterns*. World Scientific, London.

Rakos, A., Paessens, M., and Schutz, G. M. (2003). Hysteresis in one-dimensional reaction-diffusion systems. *Phys. Rev. Lett.*, 91:238302.

Reyes de Rueda, J. M., Izús, G. G., and Borzi, C. H. (1999). Critical slowing down on the dynamics of a bistable reaction-diffusion system in the neighborhood of its critical point. *J. Stat. Phys.*, 97:803.

Reynolds, W. N., Pearson, J. E., and Ponce-Dawson, S. (1994). Dynamics of self-replicating patterns in reaction diffusion systems. *Phys. Rev. Lett.*, 72:2797.

Reynolds, W. N., Ponce-Dawson, S., and Pearson, J. E. (1997). Self-replicating spots in reaction-diffusion systems. *Phys. Rev. E*, 56:185.

Rovinsky, A. and Menzinger, M. (1992). Interaction of Turing and Hopf bifurcations in chemical systems. *Phys. Rev. A*, 46:6315.

Rudovics, B., Barillot, R., Davies, P. W., Dulos, E., Boissonade, J., and Kepper, P. D. (1999). Experimental studies and quantitative modeling of Turing patterns in the (chlorine dioxide, iodine, malonic acid) reaction. *J. Phys. Chem. A*, 103:1790.

Rudovics, B., Dulos, E., and Kepper, P. D. (1996). Standard and nonstandard Turing patterns and waves in the CIMA reaction. *Physica Scripta*, T67:43.

Sanz-Anchelergues, A., Zhabotinsky, A. M., Epstein, I. R., and nuzuri, A. M. (2001). Turing pattern formation induced by spatially correlated noise. *Phys. Rev. E*, 63:056124.

Schepers, H. E. and Markus, M. (1992). Two types of performance of an isotropic cellular automaton stationary (Turing) patterns and spiral waves. *Physica A*, 188:337.

Schöpf, W. and Kramer, L. (1991). Small-amplitude periodic and chaotic solutions of the complex Ginzburg-Landau equation for a subcritical bifurcation. *Phys. Rev. Lett.*, 66:2316.

Schweitzer, F., Lao, K., and Family, F. (1997). Active random walkers simulate trunk trail formation by ants. *BioSystems*, 41:153.

Segev, R. and Ben-Jacob, E. (2000). Generic modeling of chemotactic based self-wiring of neural networks. *Neural Networks*, 13:185.

Sekimura, T., Madzvamuse, A., Wathen, A. J., and Maini, P. K. (2000). A model for colour pattern formation in the butterfly wing of papilio dardanus. *Proc. Roy. Soc. London B*, 267:851.

Stich, M. (2003). *Target patterns and pacemakers in reaction-diffusion systems*. Ph.D. thesis, Techischen Universität Berlin.

Strogatz, S. (1994). *Nonlinear Dynamics and Chaos*. Perseus, USA.

Suzuki, N., Hirate, M., and Kondo, S. (2003). Traveling stripes on the skin of a mutant mouse. *Proc. Nat. Acad. Sci.*, 100:9680.

Swift, J. and Hohenberg, P. C. (1977). Hydrodynamic fluctuations at the convective instability. *Phys. Rev. A*, 15:319.

Szili, L. and Tóth, J. (1993). Necessary condition of the Turing instability. *Phys. Rev. E*, 48:183.

Tabony, J., Glade, N., Demongeot, J., and Papaseit, C. (2002). Biological self-organization by way of microtubule reaction-diffusion processes. *Langmuir*, 18:7196.

Tarlie, M. B. and Elder, K. R. (1998). Metastable state selection in one-dimensional systems with a time-ramped control parameter. *Phys. Rev. Lett.*, 81:18.

Temmyo, J., Notzel, R., and Tamamura, T. (1997). Semiconductor nanostructures formed by the Turing instability. *Appl. Phys. Lett.*, 71:1086.

Thomas, E. L., Anderson, D. M., Henkee, C. S., and Hoffman, D. (1988). Periodic area-minimizing surfaces in block copolymers. *Nature*, 334:598.

Tlidi, M., Mandel, P., and Haelterman, M. (1997). Spatiotemporal patterns and localized structures in nonlinear optics. *Phys. Rev. E*, 56:6524.

Turing, A. M. (1952). The chemical basis of morphogenesis. *Phil. Trans. R. Soc. Lond.*, B237:37.

van Ooyen, A. (2001). Competition in the development of nerve connections: A review of models. *Network: Comput. Neural Syst.*, 12:R1.

van Saarloos, W. (1998). Three basic issues concerning interface dynamics in nonequilibrium pattern formation. *Phys. Rep.*, 301:9.

Vance, W. and Ross, J. (1999). Spatial correlations near Turing instabilities: Criteria for wavenumber selection. *J. Phys. Chem. A*, 103:1347.

Varea, C., Aragón, J. L., and Barrio, R. A. (1997). Confined Turing patterns in growing systems. *Phys. Rev. E*, 56:1250.

Vastano, J. A., Pearson, J. E., Horsthemke, W., and Swinney, H. L. (1987). Chemical pattern formation with equal diffusion coefficients. *Phys. Lett. A*, 124:320.

Vastano, J. A., Pearson, J. E., Horsthemke, W., and Swinney, H. L. (1988). Turing patterns in an open reactor. *J. Chem. Phys.*, 88:6175.

Verdasca, J., Wit, A. D., Dewel, G., and Borckmans, P. (1992). Reentrant hexagonal Turing structures. *Phys. Lett. A*, 168:194.

von Hardenberg, J., Meron, E., and Zarmi, Y. (2001). Diversity of vegetation patterns and desertification. *Phys. Rev. Lett.*, 87:198101.

Walgraef, D. (1997). *Spatio-temporal Pattern Formation*. Springer-Verlag, USA.

Walgraef, D., Dewel, G., and Borckmans, P. (1980). Fluctuations near nonequilibrium phase transitions to nonuniform states. *Phys. Rev. A*, 21:397.

Walgraef, D., Dewel, G., and Borckmans, P. (1981). Dissipative structures and broken symmetry. *J. Chem. Phys.*, 74:755.

Walgraef, D. and Ghoniem, N. M. (2003). Effects of glissile interstial clusters on microstructure self-organization in irradiated materials. *Phys. Rev. B*, 67:064103.

Weber, A., Kramer, L., Aranson, I. S., and Aranson, L. B. (1992). Stability limits of traveling waves and the transition to spatiotemporal chaos in the complex Ginzburg-Landau equation. *Physica D*, 61:279.

Yang, L., Dolnik, M., Zhabotinsky, A. M., and Epstein, I. R. (2002). Spatial resonances and superposition patterns in a reaction-diffusion model with interacting Turing modes. *Phys. Rev. Lett.*, 88:208303.

Yang, L. and Epstein, I. R. (2003). Oscillatory Turing patterns in reaction-diffusion systems with two coupled layers. *Phys. Rev. Lett.*, 90:178303.

ISBN 951-22-7395-0 (printed)
ISBN 951-22-7396-9 (PDF)
ISSN 1455-0474
Picaset Oy, Helsinki 2004